UNIVERSIDAD
NACIONAL
DE COLOMBIA

CONSTITUTIVE MODEL EVALUATION FOR PREDICTING THE MECHANICAL BEHAVIOR OF A RESIDUAL IGNEOUS SOIL IN THE SOUTH OF THE ABURRÁ VALLEY

Daniel Fernando Valencia Cifuentes

Universidad Nacional de Colombia

Facultad de Minas, Departamento de Ingeniería Civil

Medellín, Colombia

2023

Constitutive Model Evaluation for Predicting the Mechanical Behavior of a Residual Igneous Soil in the South of the Aburrá Valley

Daniel Fernando Valencia Cifuentes

Research thesis presented as partial requirement to obtain the title

of:

Magister of Science – Geotechnics

Director:

David G. Zapata Medina, Ph.D.

Codirector:

Alan J. Aparicio Ortube, Ph.D

Research line:

Soil Numerical Simulation

Universidad Nacional de Colombia

Facultad de Minas, Departamento de Ingeniería Civil

Medellín, Colombia

2023

Declaración de obra original

Yo declaro lo siguiente:

He leído el Acuerdo 035 de 2003 del Consejo Académico de la Universidad Nacional. «Reglamento sobre propiedad intelectual» y la Normatividad Nacional relacionada al respeto de los derechos de autor. Esta disertación representa mi trabajo original, excepto donde he reconocido las ideas, las palabras, o materiales de otros autores.

Cuando se han presentado ideas o palabras de otros autores en esta disertación, he realizado su respectivo reconocimiento aplicando correctamente los esquemas de citas y referencias bibliográficas en el estilo requerido.

He obtenido el permiso del autor o editor para incluir cualquier material con derechos de autor (por ejemplo, tablas, figuras, instrumentos de encuesta o grandes porciones de texto).

Por último, he sometido esta disertación a la herramienta de integridad académica, definida por la universidad.

Daniel Fernando Valencia Cifuentes

26/06/2023

Acknowledgments

First and foremost, I would like to thank God and my mother who is always supporting me from the heaven, for giving me the willing, strength and health to achieve this important goal.

This research would not have been possible without the help and guidance of Professor David Guillermo Zapata, my advisor and thesis director, and Alan Jaret Aparicio, my co-director. For every single advice, discussion, moment, and for all your time invested in this work, THANK YOU.

To my father Jorge Valencia, thank you for giving me the support I needed every day, for the patience and the love you gave me through this difficult and challenging process, for always believing in me no matter what, and for being the main pillar in my life.

And last but not least, I would like to thank my colleague and great friend Alejandro Aguirre, who always supported me with his vast experience, advises and even for giving me the physical and digital resources to proceed with this investigative work.

Abstract

The dynamic growth shown by cities has generated an accelerated reduction in useful areas and therefore the need to optimize space. This implies the need to execute works with special conditions such as important excavations, often surrounded by infrastructure that is prone to suffer affectations in its functionality and stability. In these cases, a stress-strain behavior evaluation of the soil is necessary. Geotechnical modeling has become the main engineers resource, providing a tool to numerically reproduce or predict the soil behavior. Advanced constitutive models which account for soil anisotropy, stress history, hardening-softening, among other soil characteristics, have been developed in the last decades. Nevertheless, the state of local practice shows that the vast majority of analyses are approached through limit equilibrium theories, or the application of very simple constitutive models. The application of these methods leads to not very accurate predictive results. Another important identified limitation is the lack of studies focused on the mechanical behavior of residual soils and the development and validation of constitutive models, which are often carried out on sedimentary soils. In this work an evaluation of the capabilities of three (3) constitutive models to reproduce the mechanical behavior of an Igneous residual soil in south of The Aburrá Valley is presented. Starting from advanced available residual soil characterization experimental data, the predictive capacity of the evaluated constitutive models was evaluated against very small and large strain responses, drain and undrained conditions, and different shearing paths, considering one single set of constitutive parameters per model. Inverse analysis techniques were applied in order to identify correctly the constitutive parameters that could not be obtained from the experimental data, demonstrating the high applicability of these tools on geotechnical modeling.

Keywords: Residual soil, constitutive model, inverse analysis, hypoplasticity, mechanical behavior, numerical modelling.

Evaluación de modelos constitutivos para predecir el comportamiento mecánico de un suelo residual de roca ígnea en el sur del Valle de Aburrá

Resumen

El crecimiento dinámico de las ciudades ha generado una reducción de áreas útiles, haciendo necesaria la optimización de espacio, lo que implica la ejecución de obras con condiciones especiales como excavaciones de gran magnitud, frecuentemente cerca de infraestructura existente propensa a sufrir daños. En estos casos se hace necesaria la evaluación del desempeño esfuerzo-deformación del suelo. La modelación numérica se ha convertido en el principal recurso de los ingenieros para predecir el comportamiento del suelo. A pesar de que los modelos constitutivos avanzados son capaces de reproducir aspectos del comportamiento del suelo tales como su historia de carga, anisotropía, entre otros, el estado de la práctica local se desarrolla todavía bajo teorías de equilibrio límite o modelos constitutivos muy simples, cuya aplicación resulta en predicciones poco acertadas. Otra importante falencia identificada es la falta de estudios enfocados en el comportamiento mecánico de suelos residuales, y el desarrollo y validación de modelos constitutivos aplicados a estos, que en la mayoría de casos se enfocan en suelos de origen sedimentario. En este trabajo se evalúa la capacidad de tres modelos constitutivos para reproducir el comportamiento mecánico de un suelo de origen residual de roca Ígnea del sur del Valle de Aburrá. A partir de datos experimentales avanzados de caracterización mecánica se evaluó la capacidad predictiva de los modelos ante respuesta en el rango de muy bajas y largas deformaciones, condiciones drenadas y no drenadas, y diferentes trayectorias de falla, considerando un solo set de parámetros por cada modelo. Se implementaron técnicas de análisis inverso para definir los parámetros que no pudieron ser identificados a partir de los datos experimentales disponibles, demostrando la alta aplicabilidad de este tipo de herramientas en la modelación geotécnica.

Palabras clave: Suelo residual, modelo constitutivo, análisis inverso, hipoplasticidad, comportamiento mecánico, modelación numérica.

Table of Contents

Pág.

1. Introduction 19
1.1 Statement of the Problem 21
1.2 Relevance of Research 22
1.3 Objectives of the Research 24
1.4 Content of the Thesis 24

2. Technical Background 27
2.1 Advanced Constitutive Models 28
2.1.1 Modified Cam Clay model 28
2.1.2 Hardening Soil model with small-strain stiffness (HS-Small) 31
2.1.3 Hypoplastic clay model 41
2.2 Parameter Optimization 54
2.3 Advanced Testing in Residual Soils 63
2.3.1 General description 65
2.3.2 Field testing program 66
2.3.3 Soil Sampling 67
2.3.4 Laboratory testing program 67
2.3.5 Geology and stratigraphy of the investigation site 69
2.4 Stress path rotation angle 74

3. Modeling of Boundary Element Problems 79
3.1 Numerical Simulation Conditions 80
3.1.1 Geometry, Mesh, Boundary, and Saturation Conditions 82
3.1.2 Numerical Simulation of Triaxial Stress Probes 84
3.2 Parameters Identification 90
3.2.1 Modified Cam Clay model 91
3.2.2 HSsmall model 92
3.2.3 Hypoplastic clay model 96
3.2.4 Inverse analysis results 101
3.2.5 Definitive set of parameters 118

4. Numerical Simulation Results 123

5. Summary, Conclusions and Recommendations 127
5.1 Summary 127
5.2 Conclusions 128
5.3 Recommendations 132

References 135

Appendix A: Parameter optimization code..... 145

List of figures

Pág.

Figure 2-1: Typical compressibility response of clays in oedometer testing. Modified Cam Clay model's compressibility parameters representation. 29
Figure 2-2: Yield surface of the of the Modified Cam-Clay model in the *p'-q* plane (Brinkgreve et al. 2017) 29
Figure 2-3: Hyperbolic stress-strain relation in primary loading for a standard drained triaxial test (Schanz et al. 1999). 33
Figure 2-4: Definition of $Eoedref$ in oedometer test results (Brinkgreve et al. 2017). 34
Figure 2-5: Successive yield loci for various constant values of the hardening parameter vur (Brinkgreve et al. 2017). 36
Figure 2-6: Resulting strain curve for a standard drained triaxial test when including dilatancy cut-off (Brinkgreve et al. 2017)..... 37
Figure 2-7: Yield surfaces in the *p – q* plane. The elastic region can be further reduced by means of a tension cut-off (Brinkgreve et al. 2017). 38
Figure 2-8: Representation of the total yield contour of the Hardening Soil model in the principal stress space for cohesionless soils (Brinkgreve et al. 2017). 39
Figure 2-9: Secant and tangent shear modulus reduction curve (Brinkgreve et al. 2017). 40
Figure 2-10: Plot of the mobilized dilatancy angle ψm and mobilized friction angle φm for Hardening Soil model with small-strain stiffness (Brinkgreve et al. 2017). 41
Figure 2-11: Definition of parameters N, $\lambda *$ and $k *$, taken form (Mašín 2005). 47
Figure 2-12: The effect of αf on (a) stress-strain curves and (b) stress paths of undrained triaxial tests (Mašín, 2018). 49
Figure 2-13: Calibration of the parameter μpp using undrained triaxial tests on Dortmund clay. (a) Stress-strain curves, and (b) stress paths (Mašín, 2018). 49
Figure 2-14: Influence of parameters R, βr, and χ on stiffness degradation, taken from (Mašín 2015). 51
Figure 2-15: **T**wo methods of initialization of the void ratio for the Hypoplastic clay model in finite element simulations: the first method labelled as "initialize e" and the second method labelled as "initialize *OCR*" (Mašín 2018). 53
Figure 2-16: Scheme of a basic inverse analysis procedure, taken from (Calvello, 2002). 56
Figure 2-17: Investigation site location, northwestern branch of the Colombian Andes in South America. (Source: Google Earth 2022). 66
Figure 2-18: Test pit excavation. [From: Galeano (2020)]. 67

Figure 2-19: Graphical representation of the stress paths followed during reconsolidation and shearing stages in the experimental program conducted by Galeano, (2020). 68
Figure 2-20: Subsoil conditions of the investigation site determined from field and laboratory tests. Taken from (Galeano, 2020). 70
Figure 2-21: Evolution of the coefficient of earth pressure at rest during K_0 reconsolidation. Taken from (Galeano, 2020). 73
Figure 2-22: (a) Δq-$\Delta \varepsilon_{sh}$ responses; (b) Secant shear modulus degradation curves. Modified from (Galeano, 2020). 73
Figure 2-23: (a) $\Delta p'$-$\Delta_{\varepsilon vol}$ responses; (b) Secant Bulk modulus degradation curves. Taken from (Galeano, 2020). 74
Figure 2-24: Small strain elastic shear modulus response during pseudo K_0-TX 74
Figure 2-25: Pre-shear paths: (a) recompression to in situ stresses; (b) evaluation of recent stress history, taken from (Finno and Kim, 2012). 75
Figure 2-26: Illustration of the rotation angle, taken from (Finno and Kim, 2012). 75
Figure 2-27: Secant shear modulus degradation curves. a) K_0 TXC and K_0 76
Figure 2-28: a) Hypothesized effects of recent stress history. b) Normalized stiffness degradation curves. Taken from (Finno and Kim (2012)) 77
Figure 3-1: Axisymmetric conditions scheme, modified from (Brinkgreve et al. 2017). 81
Figure 3-2: Numerical oedometer model. a) Loading and constraining conditions, b) Saturation and drainage conditions. 83
Figure 3-3: Position of the nodes and stress points in soil elements. Taken from Plaxis reference manual 84
Figure 3-4: Preshearing stress paths followed in the Hypoplastic clay model, taken from (Arboleda-Monsalve et al. 2017) 85
Figure 3-5: Hypothetical Stress Path During Tube Sampling and Specimen Preparation of Centerline Element of Low OCR Clay (after Ladd and Lambe 1963, Baligh et al. 1987), taken from [Ladd and DeGroot (2003)]. 85
Figure 3-6: Pre-shearing stress paths followed for the numerical simulation of triaxial stress probes. 86
Figure 3-7: Shearing stress paths followed in the numerical triaxial tests simulations 86
Figure 3-8: Initial conditions of the numerical model in Plaxis 2D. 87
Figure 3-9: Saturation stage. a) Loading and constrained conditions, b) Saturation and drainage conditions, all boundaries closed to seepage. 88
Figure 3-10: K_0 reconsolidation stage. a) Loading and constrained conditions, b) Saturation and drainage conditions, all boundaries opened to seepage. 89
Figure 3-11: Shearing stage under stress-controlled conditions. a) Loading and constrained conditions, b) Saturation and drainage conditions for the TXC and RTXE paths, c) Saturation and drainage conditions for the tests sheared under other paths. 90
Figure 3-12: Compression range obtained from compressibility tests – Caldas residual soil. 91

Figure 3-13: Unloading-reloading cycles obtained from compressibility tests – Caldas residual soil. 91
Figure 3-14: Critical state line – Caldas residual soil. 92
Figure 3-15: Oedometric modulus-vertical effective stress in logarithmic space. 93
Figure 3-16: Dilatancy behavior evaluated from drained triaxial tests. a) CMNE, b) CMNS, c) CQL, and d) CQU stress paths. Taken from (Galeano, 2020) 95
Figure 3-17: Incremental Loading (IL) and Constant Rate of Strain (CRS) oedometer tests in the $ln1 + e\text{-}lnp'$ space for Caldas soil. 96
Figure 3-18: Compression range of incremental IL and CRS oedometer tests in the $ln1 + e\text{-}lnp'$ space for Caldas residual soil. 97
Figure 3-19: Normalized compressibility response for Caldas soil. 98
Figure 3-20: Recompression range for the IL and CRS oedometer tests in the $ln(1 + e)\ vs\ ln(p)$ space for Caldas Soil – Unload portion 98
Figure 3-21: Bender Element test results during K_0-reconsolidation – Caldas residual soil. a) Arithmetic space, b) Logarithmic space. 100
Figure 3-22: Parameters composite scaled sensitivities ($cssj$) results. Axial strain-deviatoric stress ($\varepsilon a\text{-}q$): a) TXC results and b) RTXE results. Modified Cam Clay model. 104
Figure 3-23: Parameters composite scaled sensitivities ($cssj$) results. Secant shear modulus degradation ($Gsec$): a) TXC results and b) RTXE results. Modified Cam Clay model. 104
Figure 3-24: Parameter correlation coefficients results. Axial strain-deviatoric stress ($\varepsilon a\text{-}q$) : a) TXC results and b) RTXE results. Modified Cam Clay model. 104
Figure 3-25: Parameters correlations coefficients results. Secant shear modulus degradation ($Gsec$) : a) TXC path and b) RTXE path. Modified Cam Clay model 105
Figure 3-26: Parameters composite scaled sensitivities ($cssj$) results for overall response. Axial strain-deviatoric stress ($\varepsilon a\text{-}q$) and Secant shear modulus degradation ($Gsec$): a) TXC path and b) RTXE path. Modified Cam Clay model.....105
Figure 3-27: Parameters correlations coefficients results for overall response. Axial strain-deviatoric stress ($\varepsilon a\text{-}q$) and Secant shear modulus degradation ($Gsec$): a) TXC results and b) RTXE results. Modified Cam Clay model. 105
Figure 3-28: Parameters composite scaled sensitivities ($cssj$) results. Axial strain-deviatoric stress ($\varepsilon a\text{-}q$): a) TXC results and b) RTXE results. HSsmall model. 106
Figure 3-29: Parameters composite scaled sensitivities ($cssj$) results. Secant shear modulus degradation ($Gsec$) : a) TXC results and b) RTXE results. HSsmall model. 106
Figure 3-30: Parameters correlations coefficients results. Axial strain-deviatoric stress ($\varepsilon a\text{-}q$) : a) TXC results and b) RTXE results. HSsmall model. 107
Figure 3-31: Parameters correlations coefficients results. Secant shear modulus degradation ($Gsec$): a) TXC results and b) RTXE results. HSsmall model. 107
Figure 3-32: Parameters composite scaled sensitivities ($cssj$) results for overall response. Axial strain-deviatoric stress ($\varepsilon a\text{-}q$) and Secant shear modulus degradation ($Gsec$): a) TXC results and b) RTXE results. HSsmall model. 108

Figure 3-33: Parameters correlations coefficients results for overall response. Axial strain-deviatoric stress (εa-q) and Secant shear modulus degradation ($Gsec$): a) TXC results and b) RTXE results. HSsmall model. 108
Figure 3-34: Parameters composite scaled sensitivities ($cssj$) results. Axial strain-deviatoric stress (εa-q): a) TXC results and b) RTXE results. Hypoplastic clay model... 109
Figure 3-35: Parameters composite scaled sensitivities ($cssj$) results. Secant shear modulus degradation ($Gsec$): a) TXC results and b) RTXE results. Hypoplastic clay model. 109
Figure 3-36: Parameters correlations coefficients results. Axial strain-deviatoric stress (εa-q): a) TXC results and b) RTXE results. Hypoplastic clay model. 110
Figure 3-37: Parameters correlations coefficients results. Secant shear modulus degradation ($Gsec$): a) TXC results and b) RTXE results. Hypoplastic clay model. 111
Figure 3-38: Parameters composite scaled sensitivities ($cssj$) results for overall response. Axial strain-deviatoric stress (εa-q) and Secant shear modulus degradation ($Gsec$): a) TXC results and b) RTXE results. Hypoplastic clay model..... 111
Figure 3-39: Parameters correlations coefficients results for overall response. Axial strain-deviatoric stress (εa-q) and Secant shear modulus degradation ($Gsec$): a) TXC results and b) RTXE results. Hypoplastic clay model. 112
Figure 3-40: Secant shear modulus degradation curves. Modified Cam Clay model a) Initial parameters b) Optimized parameters..... 120
Figure 3-41: Secant shear modulus degradation curves. HSsmall model a) Initial parameters b) Optimized parameters..... 120
Figure 3-42: Secant shear modulus degradation curves. Hypoplastic clay model a) Initial parameters b) Optimized parameters..... 120
Figure 3-43: Axial strain-deviatoric stress (εa-q) curves. Modified Cam Clay model a) UTXC b) RTXE. 121
Figure 3-44: Axial strain- deviatoric stress (εa-q) curves. HSsmall model a) UTXC b) RTXE 121
Figure 3-45: Axial strain-deviatoric stress (εa-q) curves. Hypoplastic clay model a) UTXC b) RTXE 122
Figure 4-1: Secant shear modulus degradation. Experimental versus simulated data a) UTXC, b) URTXE, c) CMNS, and d) CMNU. 123
Figure 4-2: *Δq*- shear strain. Constitutive models comparison a) UTXC b) URTXE 124
Figure 4-3: *Δq*- shear strain. Constitutive models comparison a) CMNS b) CMNU 124
Figure 4-4: Axial strain-deviatoric stress (εa-q). Constitutive models comparison a) UTXC b) URTXE..... 124
Figure 4-5: Axial strain-deviatoric stress (εa-q). Constitutive models comparison a) CMNS b) CMNU..... 125
Figure 4-6: Volumetric strain-mean stress (εvol-$\Delta p'$). Constitutive models comparison a) CQL b) CQU 125

Figure 4-7: Axial strain-mean stress (εa-p'). Constitutive models comparison a) CQL b) CQU.....125
Figure 4-8: 1D compression curves**.** Axial strain-mean stress (εa- p') Constitutive models comparison 126

List of tables

Pág.

Table 2-1: Modified Cam Clay Model constitutive parameters. 30
Table 2-2: Standard Hardening Soil Model constitutive parameters. 32
Table 2-3: Basic Hypoplastic model constitutive parameters for different soils (After Mašín, 2017; Arboleda-Monsalve et al. 2017) 48
Table 2-4: Intergranular strain concept constitutive parameters for different soils, (After Mašín, 2017; Arboleda-Monsalve et al. 2017) 51
Table 2-5: Summary of index and compressibility properties, taken from (Galeano, 2020) 69
Table 2-6: Summary of compressibility parameters and sample quality assessment, taken from (Galeano, 2020)..... 71
Table 3-1: Selected weights for the observations. 101
Table 3-2: Initial parameter set considered for statistical analysis and optimization techniques – Modified Cam Clay model. 102
Table 3-3: Initial parameter set considered for statistical analysis and optimization techniques – HSsmall model. 102
Table 3-4: Initial parameter set considered for statistical analysis and optimization techniques – Hypoplastic clay model. 103
Table 3-5: Fit measurement variables. Axial strain-deviatoric stress (εa-q) on UTXC stress path. 114
Table 3-6: Fit measurement variables. Secant shear modulus degradation ($Gsec$) on UTXC stress path. 114
Table 3-7: Fit measurement variables. Axial strain-deviatoric stress (εa-q) on URTXE stress path. 115
Table 3-8: Fit measurement variables. Secant shear modulus degradation ($Gsec$) on URTXE stress path. 115
Table 3-9: Fit measurement variables for overall response: Axial strain-deviatoric stress (εa-q) and Secant shear modulus degradation ($Gsec$) on UTXC stress path. 116
Table 3-10: Fit measurement variables for overall response: Axial strain-deviatoric stress (εa-q) and Secant shear modulus degradation ($Gsec$) on URTXE stress path. 117
Table 3-11: Fit measurement variables for overall response: UTXC and URTXE stress paths. 117
Table 3-12: Constitutive parameters set – Modified Cam Clay model. 118
Table 3-13: Constitutive parameters set – HSsmall model. 119

Table 3-14: Constitutive parameters set – Hypoplastic clay model. 119
Table 5-1: Ranges of physical and mechanical properties for soil applicability..... 132

1. Introduction

The formation of residual soils is favored by the geographic location of Colombia, considering its climate, precipitation regime, orography, among other factors (Torres and Colmenares, 2017). Due to these conditions encountered at inter-tropical latitudes, the soils tend to develop different mineralogical, physicochemical, and mechanical properties when compared with sedimentary soils. Despite approximately 40% of the world's population is settled in the Tropics, which constitute approximately 40% of the Earth's surface area, research on residual soils is not as advanced as on sedimentary soils. Limited investigations conducted to study the mechanical behavior of residual soils are found in the technical literature, as pointed out by Xinyu Liu et al (2021) and Shu et al (2021).

In most geotechnical projects, the soil mass is subjected to a variety of stress paths which may lead to ground settlements, lateral displacements, failures, among others. When soil deformations are of interest, numerical simulation in combination with robust constitutive models are required to adequately recreate in-situ conditions, such as stratigraphy, groundwater, load applications, among others, and predict soil response (Knabe et al. 2012; Desai and Zaman, 2014). A constitutive soil model can be defined as a mathematical representation of the soil mechanical behavior under different load and displacement conditions (stresses and strains increments). The selection of a constitutive model not only depends on the problem conditions (Lade, 2005) but also the determination of constitutive parameters that compose the soil model. The more advanced the constitutive soil model, generally the more of the amount of constitutive parameters to be determined. In practical geotechnical applications, at times insufficient data are available to define all the constitutive parameters of the advanced models (Brinkgreve, 2005). The selection of a constitutive model depends on several factors such as the soil type, conditions of the problem, available soil characterization information (commonly obtained from laboratory and field procedures), the understanding of the model capabilities and limitations, the

meaning and influence of each constitutive parameter on the computed response, engineering judgment, among others (Brinkgreve, 2005).

Despite the recent advance of the geotechnical numerical simulation, available advanced constitutive soil models, among others, the complexity of recent geotechnical works still demands the state of the practice to be enhanced in order to implement new procedures which can lead to a more accurate soil behavior prediction (J. Krahn, 2003). These improvements must be at least capable of reproducing soil stress-strain behavior relationships taking into account aspects such as non-linearity, anisotropy, strength, and stiffness, among others. In the last decade, several investigations have shown that geotechnical finite element procedures have been enhanced with powerful mathematic algorithms which make easier to calibrate advanced constitutive models (Knabe et al. 2012).

In this research three (3) constitutive models were evaluated, specifically in terms of their capabilities to reproduce the mechanical behavior of a residual Igneous soil located in Colombia, specifically in the south of the Aburrá valley. Advanced experimental data was investigated and evaluated in order to calibrate the assessed constitutive models and measure their applicability to predict the target soil's mechanical behavior. The main requirement of the employed experimental laboratory data in this research was the availability of at least high-quality specimens with an accurate field and physical soil description tested under one-dimensional conditions, drained and undrained triaxial conditions following different stress paths (compression and extension), and advanced laboratory instrumentation which allows to evaluate the stiffness of the material in the very small and small strain range. The work of Galeano (2020) fulfills all these requirements.

A single set of parameters was defined for each evaluated constitutive model, in order to assess the predicted mechanical response at small and large strain levels, drained and undrained conditions, and over a wide range of stress paths. The determination of one single set of parameters capable to reasonably capture the mechanical behavior of a soil under different conditions solves the geotechnical modeling need to divide a certain problem into two or more different modeling stages with different constitutive parameters. The accuracy of the constitutive model and soil parameters were assessed by comparing

the numerical simulations results with the available laboratory data. Numerical simulations were developed via finite element models (FEM) performed in PLAXIS 2D software, under axisymmetric conditions (boundary element problems). The parameters of soil constitutive models are typically estimated from laboratory data, but it is not common to see practical cases where only one set of parameters can reproduce different conditions such as stress paths and drainage conditions (Wichtmann, 2016).

Inverse analysis techniques (mathematical algorithms) are useful in cases where not all the constitutive parameters of a determined model can be obtained via field and/or laboratory data. These kind of techniques allow the geotechnist to minimize the discrepancy between the experimental data and the numerical modeling results, reducing the consumed time (Knabe et al. 2012). The implementation of inverse analyses in geotechnical modeling must be preceded by a deep recognition of the assumptions and approximations related to the employed constitutive model, and to have an accurate engineering judgment to assess the reliability of the numerical predictions (Sarabia, 2012). In this work, a methodology based on inverse analysis (optimization techniques) was implemented in order to complement the determination of the constitutive parameters that compose the assessed models.

1.1 Statement of the Problem

The dynamic growth of the cities in Colombia has generated an accelerated reduction in useful areas and, therefore, the need to optimize space. Highly relevant engineering projects for the Aburrá Valley have been executed during the last three (3) decades, such as the tunnel *Fernando Gómez Martínez* (1998-2006), sewage treatment plant *PTAR Bello* (2012-2019), *Túnel de Oriente* (2014-2019), which is the longest tunnel in South America and its construction process included tunneling across soil and rock, slope stability, bridges, among others. Also, other important works are being developed or projected for the near future, such as the *Metro* and *Metro-Plu*s system extension, highway *Regional Norte*, the railway *Ferrocarril de Antioquia*, *Central Park*, city hall of Envigado city, etc. The Aburrá Valley presents in general terms, a relief that magnifies the need of space optimization since it is a narrow valley with a hillside environment where it is common to find thick weathering soil profiles, either from slope deposits or residual soils from the different geological formations (AMVA, 2007).

The mentioned conditions make more frequent the need to execute works with special conditions such as large buildings, involving special foundations and important excavations. In general, these works are surrounded by infrastructure that is prone to suffer affectations in its functionality and stability in the most critical cases. In these cases, a performance analysis based on the study of stress-strain behavior is necessary. To date, despite the availability of several recent advanced constitutive models, the state of local practice is at a point where the vast majority of analyses are approached employing limit equilibrium (resistance) theories, or the application of very simple constitutive models which are not accurate enough for the design and performance evaluation needs of current geotechnical works (Hsiung and Dao, 2014; Krahn, 2003; Baba et al. 2014). As pointed by Gudehus et al. (2008), the users of constitutive models generally do not have the time or the expertise to implement the constitutive models in their geotechnical modeling by themselves and therefore their choice of models remains confined to the few (often primitive) models utilized in their local environment.

This scenario implies the need to enhance the local state of art related to residual soils and its numerical modeling, reducing the uncertainty in the soil response by improving the "predictive" capacity of the geotechnical modeling via an accurate application of advanced constitutive models. The calibration of advanced models depends on a large and complex set of variables that are related to the characteristics of the material such as its genesis, stress history, degree of weathering, strain levels, etc. (Schweiger, 2008). In most cases, the development and validation of most constitutive models has been limited to transported soils from geological environments that differ from residual soils, and which can therefore evidence different mechanical responses, mainly due to the fact that in the behavior of residual soils, its weathering process and the development of their structure and genesis (parental rock) takes great relevance (Wesley, 2009).

1.2 Relevance of Research

The proposed research is focused on a need of the engineering local environment, where the magnitude and complexity of geotechnical works is increasing and require a more rigorous approach for the prediction of soil behavior, considering especially the stress-strain

relationships that control the performance of engineering works and their influence on surrounding infrastructure.

To adequately predict the stress-strain behavior, advanced models with the capacity to capture the incremental non-linearity of the soil, the small strain behavior, the load history, and anisotropic stress state, among others, must be included. In general, the required advanced responses depend on complex parameters. A great part of the development and validation of these models has been carried out on sedimentary soils (Xinyu Liu et al. 2021), which present different characteristics and behavior with respect to the residual soils that occur in the Aburrá Valley. Research on advanced constitutive models applied to the residual soils of Colombia is very limited and, therefore, it becomes a weakness of engineering as the necessary tools to address the most complex problems are not available (deeply studied).

According to Desai and Zaman (2014), understanding and defining the behavior of engineering materials are essential for realistic and economic geotechnical analyses. The application of numerical methods with advanced constitutive models allows a better understanding of the mechanical behavior of complex geotechnical problems and also may significantly facilitate the design procedure and risk assessment (Schweiger, 2008). This research seeks to advance in the state of the art and practice of Colombian residual soils, relying on existing and recent advances on the development and application of constitutive models, with the aim of providing tools and support for the modelling of geotechnical problems in the local geological and geotechnical environment.

An accurate identification of constitutive models capable of reproducing the mechanical behavior of local residual soils represent a powerful tool to model geotechnical problems. Designs can be improved by having a more realistic numerical representation of the soil, shortening the gap between predicted performance and the actual one. Relevant and complex geotechnical works located in the Aburrá Valley, specifically on sites with a residual soil profile similar to the one assessed in this research, would be influenced by easier, more realistic, and safer designs, with fewer uncertainties that can could lead to more robust solutions and thus lower construction costs.

1.3 Objectives of the Research

The main objective of this research is to assess the performance of existing constitutive soil models that can capture the mechanical behavior of an Igneous residual soil in the south of the Aburrá Valley.

The specific objectives of this work includes:

- Identify constitutive models that have the attributes and potential to reproduce the mechanical response of residual soils.
- Identity and evaluate the available local experimental laboratory data related to Igneous residual soils mechanical behavior. The laboratory data must contain high quality experimental tests results, including at least triaxial tests with small strain measurements, one-dimension compression tests, and the evaluation of maximum secant shear modulus and its degradation.
- Calibrate and validate the constitutive parameters of the assessed models based on the responses obtained from the laboratory tests.
- Implement an inverse analysis (parameter optimization) routine that can reduce the time spent, identifying the constitutive parameters that cannot be obtained from the available experimental data.
- Compare the numerical results to evaluate the performance of the assessed models by means of statistical techniques and select the one(s) that best fit the soil laboratory responses. Propose a characterization methodology that allows the calibration of these models, (*i.e.,* the correct identification of the parameters that control the constitutive model).

1.4 Content of the Thesis

This thesis is composed of five chapters. Chapter 2 presents the Technical Background relate to advanced constitutive models, parameter optimization techniques (inverse analyses), statistical fit measurements, advanced testing in residual soils, and stress path rotation angle concept. In this chapter a detailed description of the three evaluated constitutive models and the experimental field and laboratory work that were selected, is presented.

Chapter 3 presents the description of the numerical simulation of the conducted Boundary Element Problems, along with the justification of why these constitutive models were selected for this work. Different conditions of the numerical models such as geometry, meshing, boundary, saturation and model stages are described. The identification of the constitutive parameters is also presented in this chapter, along with the results of the inverse analyses procedures and the definitive set of parameters for each evaluated constitutive model.

Chapter 4 presents the Numerical Simulation Results. These results are presented in terms of graphs that describe the mechanical behavior of the Caldas residual soil in comparison to the laboratory experimental data (Galeano, 2020). Both triaxial probes and 1-D compression tests are presented in this chapter.

Chapter 5 of this thesis presents the summary of the research, the conclusions and the recommendations.

2. Technical Background

The understanding of soil behavior has been a latent need for several years. The first approaches were closely linked to the classical theory of elasticity formulated by Robert Hooke (Timoshenko, 1951), from which the basis for the construction of knowledge in soil mechanics was forged. This theory was the first approximation to describe the deformations undergone by the soil against different changes in its stress state. However, these approximations have limitations because the studied material does not completely fulfill the initial hypothesis governing elasticity, which describe continuous, homogeneous, isotropic, and elastic materials. Soils as porous, particulate materials, highly dependent on their genesis and stress conditions, present responses that in several cases are considerably different from the predictions of elasticity. From the identification of this limitation, the advances in the concept of elasticity and plasticity began, and among them the contributions of Tresca (19th century) and Von Mises (20th century) stand out. These theories define that a material is not totally elastic, but there is an applied stress from which non-recoverable deformations appear (plasticity). An elasto-plastic model requires the definition of three general elements, which consist of the determination of the yielding range where the soil changes its elastic behavior or response, the flow rule that indicates how the deformations advance after this yield is overcome, and the other element is the type of behavior (*i.e.*, hardening or softening).

From these first advances, different elasto-plastic models applied to soils have been built and refined, which have involved the effect of the stress paths (loading-unloading) and the stress history of the material, relating them to its stress-strain behavior, thus providing more realistic and accurate responses.

2.1 Advanced Constitutive Models

Some of the widely known advanced constitutive soil models include the Generalized Hardening Soil (GHS) model (Schanz et al. 1999), Hypoplastic model for clays (Mašín, 2005), Anisotropic M3-SKH (Ellison, 2012), Barcelona Basic Model (Alonso et al. 1990), PM4Silt (Boulanger and Ziotopoulou, 2018), among others. Most of these theories have been mainly developed on soils formed mainly by sedimentary deposits, with certain homogeneity and common characteristics. These materials differ from those located in the tropics, specifically residual soils and/or deposits derived from them, where their behavior is highly influenced by the factory of origin (parent rock) and the chemical processes experienced during the weathering processes. The constitutive soil models evaluated in this research are presented and described in the following sections.

2.1.1 Modified Cam Clay model

Cam Clay formulations are considered as the first Critical State models and were developed at the University of Cambridge. The original Cam Clay elasto-plastic model was formulated by Roscoe and Schofield (1963) and Schofield and Wroth (1968). The modified Cam Clay model was later presented by Roscoe and Burland (1968). The modified Cam Clay model is an elasto-plastic model based on the Critical State theory and assumes a logarithmic relation between the mean effective stress, ***p',*** and void ratio, ***e,*** during isotropic compression, which is mainly given by the isotropic compression index, $\boldsymbol{\lambda}$. The compressibility of the material during unloading or reloading is given by swelling index parameter, k**.** Isotropic compression and isotropic unloading-reloading formulation are given in Equations (1) and (2), respectively.

$$e - e^0 = -\lambda \, ln\left(\frac{p'}{p^0}\right) \tag{1}$$

$$e - e^0 = -k \, ln\left(\frac{p'}{p^0}\right) \tag{2}$$

where e^0 and p^0 correspond to known values of void ratio and mean effective stress.

The typical response of clays under one-dimensional compression tests is presented in **Figure 2-1**. Variable v corresponds to the specific volume, $v = 1 + e$.

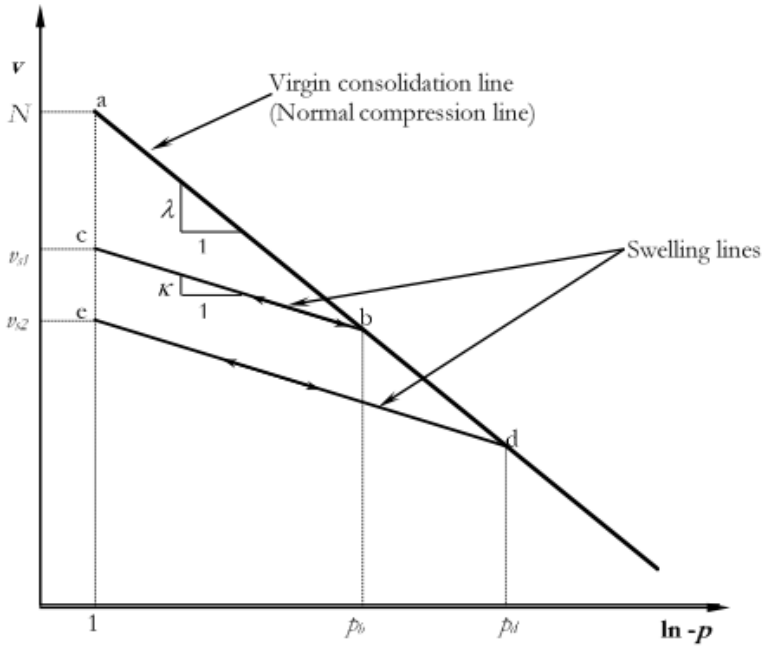

Figure 2-1: Typical compressibility response of clays in oedometer testing. Modified Cam Clay model's compressibility parameters representation.

Figure 2-2 illustrates the yield surface of the Modified Cam Clay (MCC) model in the effective mean normal stress and deviator stress space (*i.e.*, *p'-q* space). Strains inside the elliptical yield surface are elastic while outside are plastic.

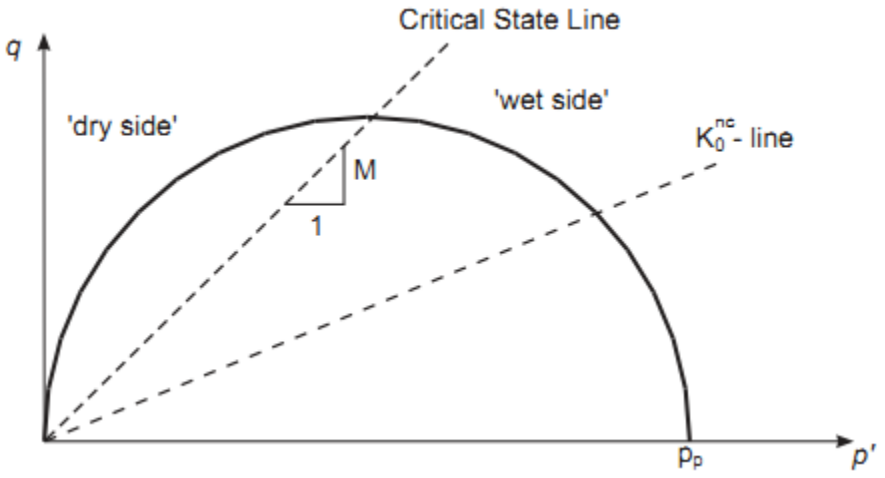

Figure 2-2: Yield surface of the of the Modified Cam-Clay model in the *p'-q* plane (Brinkgreve et al. 2017)

The yield function of the model can be described by Equation (3), where p_p is the preconsolidation stress. Any yield surface will be always associated to a specific

preconsolidation stress. The critical state line (CLS) intersects the elliptical yield surface in the point $q = Mp'$, in the *p'-q* space. Parameter *M* is the tangent of the critical state line and also determines the height of the yielding surface and has influence in the lateral earth pressure coefficient, ${K_0}^{NC}$, under one-dimensional compression.

$$f = \left(\frac{q2}{2}\right) + p'(p' - p_p) \tag{3}$$

This model is capable to reproduce soil hardening and softening phenomena, which are related to changes in void ratio and specific volume. When yielding occurs to the left side of the intersection of the CSL (dry side), the material exhibits softening and thus an increase in volume. When yielding occurs to the right side (wet side), hardening takes place and reduction of the volume occurs.

The Modified Cam Clay model formulation is given by 6 constitutive parameters, listed in **Table 2-1**. Parameter v_{ur} is an elastic parameter which value ranges between 0.1 and 0.2.

Table 2-1: Modified Cam Clay Model constitutive parameters.

#	Symbol	Parameter	Unit
1	λ	Compression index	-
2	k	Swelling index	-
3	v_{ur}	Poisson's ratio	-
4	e_{init}	Initial void ratio for loading/unloading	-
5	M	Tangent of the critical state line	-
6	${K_0}^{NC}$	Coefficient of lateral stress in normal consolidation	-

In Plaxis software, parameter ${K_0}^{NC}$ can be automatically determined based on parameter M, according to the following expression:

$$M = 3 - 2.8{K_0}^{NC} \tag{4}$$

Since parameter M is related to the shear strength and based on the critical state theory, it can be derived from the critical state friction angle, φ. Equation (5) is derived from triaxial conditions. Negative sign for compression and positive sign for extension.

$$M = \frac{6\ sin\varphi}{3 \pm sin\varphi} \tag{5}$$

One of the Modified Cam Clay model's limitation is the overestimation of shear stresses, mainly under stress paths beyond the critical state line. Moreover, this model may reproduce an unwanted soil softening which can lead to mesh dependency and converge problems. Also, since their constitutive parameters are based on drained soil behavior, undrained shear strength predictions might not be very accurate. Another important shortcoming of this model is the fact that only estimates elastic behavior inside the yield surface (Ti et al. 2009; Brinkgreve, 2005).

2.1.2 Hardening Soil model with small-strain stiffness (HS-Small)

In this section a constitutive model which works with a double-stiffness framework for elasticity combined with isotropic strain hardening is described. The Hardening Soil model (HS-Standard) was first developed by Schanz et al. (1999) accounting for some capabilities such as to reproduce the stress-dependency in the stiffness of the material, preconsolidation effects (stress history), decrease of voids in soil structure under plastic deformations (densification), among some others. Hardening Soil formulation is based on a multi-yield surface model and could be considered as an upgrade of The Hyperbolic model (incremental elasticity) with the addition of three main aspects: inclusion of soil dilatancy effects; introduction of a yield cap; and use of the plasticity theory rather than the elasticity theory.

Standard Hardening Soil model does not work with Hooke's single-stiffness with linear elasticity but it is capable to reproduce elasto-plastic response of stiff and soft soils. The yielding surface of the Hardening Soil Model does not work with a principal stress space but can consider plastic straining, which results in more accuracy than other models working in the field of elasticity and perfect plasticity.

The two main types of behaviors considered in this model are compression hardening and shear hardening. The first one takes place when primary compression (oedometer and/or isotropic loading) induces irreversible plastic strains, and the second one is related to deviatoric loads that induce irreversible strains. As shown in **Table 2-2**, the numerical implementation of the Standard Hardening-Soil model requires the input of 13 parameters. Contrary to other models such as Modified Cam Clay, the magnitude of soil deformations can be modeled more accurately by incorporating three input stiffness parameters

corresponding to the triaxial loading stiffness (E_{50}), the triaxial unloading-reloading stiffness (E_{ur}), and the tangent stiffness for primary oedometer loading (E_{oed}).

Table 2-2: Standard Hardening Soil Model constitutive parameters.

#	Symbol	Parameter	Unit
1	c'	Cohesion intercept	Stress
2	φ'	Angle of internal friction	Degrees
3	ψ	Angle of dilatancy	Degrees
4	${E_{50}}^{ref}$	Secant stiffness at 50% stress level in standard drained triaxial test	Stress
5	${E_{oed}}^{ref}$	Tangent stiffness for primary oedometer loading	Stress
6	m	Power for stress-level dependency of stiffness	-
7	${E_{ur}}^{ref}$	Unloading/reloading stiffness (default ${E_{ur}}^{ref}=3{E_{50}}^{ref}$),	Stress
8	v_{ur}	Poisson's ratio for unloading-reloading (default $v_{ur}=0.2$)	-
9	p^{ref}	Reference stress for stiffness (default p^{ref}=100 stress units)	Stress
10	${K_0}^{NC}$	K_0 value for normal consolidation. Default ${K_0}^{NC}=1-sin(\varphi)$	-
11	R_f	Failure ratio q_f/q_a (default $R_f=0.9$),	-
12	$\sigma_{tension}$	Tensile strength (default $\sigma_{tension}=0$ stress units)	Stress
13	$c_{increment}$	Increase of cohesion per unit of depth (default $c_{increment}=0$)	Stress

The constitutive parameters can be separated in two groups, one related to the primary-deviatoric loading behavior, and the other related to the stiffness soil behavior. The hyperbolic stress-strain curve which represents the soil response when is subjected to a primary load is shown in **Figure 2-3**. For monotonic load mechanisms this model considers the secant modulus (E_{50} determined from a triaxial stress-strain curve at 50% of the ultimate shear strength) as the reference parameter. The parameter E_{50} is the confining stress dependent stiffness modulus for primary loading. Effective confining stress ($-{\sigma'}_3$) is directly related to the secant modulus, considering isotropic consolidated conditions. It can be said that E_{50} is dependent on $-\sigma_3$. Secant modulus of the material can be defined as:

$$E_{50} = {E_{50}}^{ref} \left(\frac{c\ cot\varphi - {\sigma'}_3\ sin\varphi}{c\ cos\varphi + p^{ref}\ sin\varphi} \right)^m \quad (6)$$

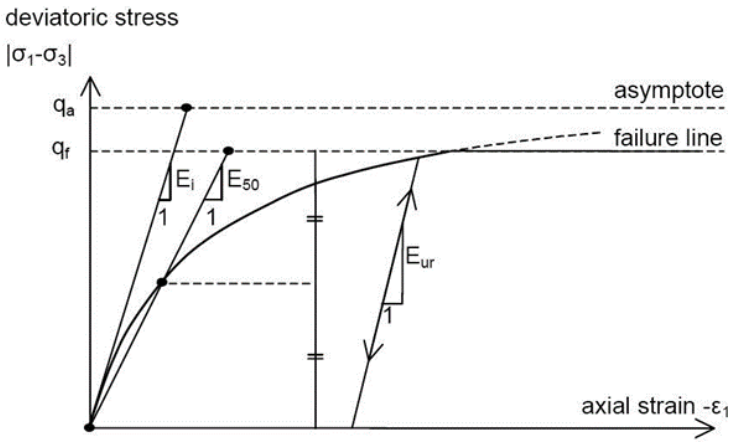

Figure 2-3: Hyperbolic stress-strain relation in primary loading for a standard drained triaxial test (Schanz et al. 1999).

In Equation (6), the variables *c* and *φ* correspond to the Mohr-Coulomb strength parameters, cohesion intercept and friction angle, respectively, $E_{50}{}^{ref}$ corresponds to the secant modulus at the reference stress, and *m* refers to the amount of stress dependency. For simulating a logarithmic stress dependency, parameter *m* should be considered as 1.0, for heavily overconsolidated soils, (*OCR*>2) *m* should take values near to 0, and for other soils, *m* can typically take values between 0.5 to 1.0.

The hyperbolic relationship between the vertical strain ε_1 and deviatoric stress $q = \sigma_1 - \sigma_3$ during primary triaxial loading can be described by Equation (7), applicable for stress states $q < q_a$.

$$-\varepsilon_1 = \frac{q}{E_i \left(1 - \frac{q}{q_a}\right)} \tag{7}$$

$$q_a = \frac{q_f}{R_f} \tag{8}$$

$$E_i = \frac{2E_{50}}{2 - q_f} \tag{9}$$

$$q_f = (c\ cot\varphi - \sigma'_3\ sin\varphi)\frac{2sin\varphi}{1 - sin\varphi} \tag{10}$$

In the previous Equations, the variable q_a refers to the asymptotic shear strength and E_i is the initial stiffness modulus. Equation (10) is derived from the Mohr-Coulomb failure criterion and implies that after deviatoric stress q is equal to q_f perfectly plastic yielding occurs. The stress-dependent stiffness modulus is implemented in this model for the

unloading-reloading stress paths, see Equation (11) and **Figure 2-3**. Again, for this behavior (unload-reload), the modulus depends on the effective confining stress and the reference pressure.

$$E_{ur} = {E_{ur}}^{ref} \left(\frac{c\ cot\varphi - {\sigma'}_3\ sin\varphi}{c\ cos\varphi + p^{ref}\ sin\varphi} \right)^m \tag{11}$$

Corresponding to the stress dependency of soil stiffness under primary compression (oedometer conditions specifically), the numerical formulation of the model considers an oedometric modulus as the reference parameter at a specific reference stress value (p^{ref}) in order to define the soil stiffness, as shown in Equation (12):

$$E_{oed} = {E_{oed}}^{ref} \left(\frac{\sigma}{p^{ref}} \right)^m \tag{12}$$

One of the advantages of the elastoplastic Hardening Soil over other elasticity-based models is that the first one does not work with a fixed relationship between triaxial stiffness, E_{50} , and oedometric stiffness, E_{oed} , but both can be defined and introduced independently. Equation (13) and **Figure 2-4** describe how the tangent stiffness modulus E_{oed} is obtained from oedometer tests.

$$E_{oed} = {E_{oed}}^{ref} \left(\frac{c\ cot\varphi - \frac{{\sigma'}_3\ sin\varphi}{{K_0}^{NC}}}{c\ cos\varphi + p^{ref}\ sin\theta} \right)^m \tag{13}$$

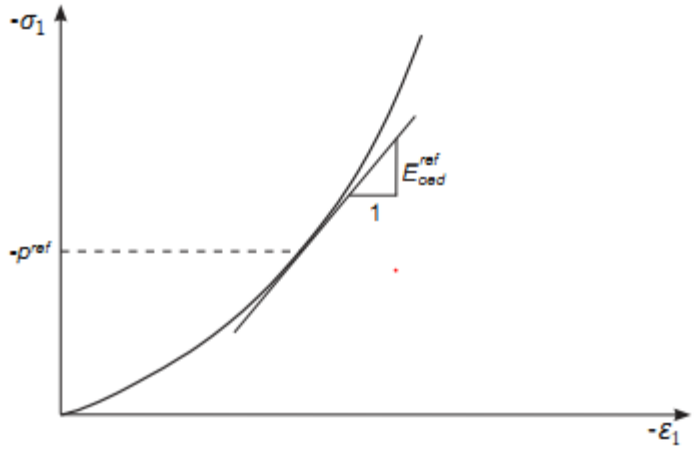

Figure 2-4: Definition of ${E_{oed}}^{ref}$ in oedometer test results (Brinkgreve et al. 2017).

Variable v_{ur} is dependent on the strain level but commonly varies between 0.1 and 0.2 (Brinkgreve et al. 2017). It should be remarked that this is a pure elastic parameter related to an unloading/reloading process and strains developed during deviatoric loading.

Other advantage of the Hardening Soil model can be seen in the lateral earth pressure coefficient parameter, ${K_0}^{NC}$, which is an independent variable and not a simply function of the Poisson's ratio (as for Mohr-Coulomb model). Despite Plaxis software uses a default correlation ${K_0}^{NC} = 1 - \sin(\varphi)$, users can input different values. Considering standard drained triaxial stress paths, the plastic strains are computed under a shear hardening yield function with the following form:

$$f = \bar{f} - \gamma^p \tag{14}$$

$$\bar{f} = \frac{2q}{E_i\left(1 - \frac{q}{q_a}\right)} - \frac{2q}{E_{ur}} \tag{15}$$

$$\gamma^p = -(2{\varepsilon_1}^p - {\varepsilon_v}^p) \approx -2{\varepsilon_1}^p \tag{16}$$

ε_v denotes volumetric strains, ε_1 is refered to axial strains, $\bar{f}$ is a function of stress, γ^p is the function of plastic strains, and the superscript p denotes plastic strains. Plastic strains are developed during primary loading while elastic ones develop both in primary loading and unloading-reloading. For drained stress triaxial paths with constant radial stress, elastic modulus, E_{ur} , remains constant and elastic strains are given by the following Equations:

$$-{\varepsilon^e}_1 = \frac{q}{E_{ur}} \tag{17}$$

$$-{\varepsilon^e}_2 = -{\varepsilon^e}_3 = -v_{ur}\frac{q}{E_{ur}} \tag{18}$$

Plastic strains under primary loading, when $\bar{f} = \gamma^p$, can be expressed as:

$${\varepsilon^p}_1 = 0.5\bar{f} = \frac{q}{E_i\left(1 - \frac{q}{q_a}\right)} - \frac{q}{E_{ur}} \tag{19}$$

For deviatoric loads, the axial strains are the sum of the elastic and plastic components presented in Equation (20), when plastic volumetric strains do not develop.

$$-{\varepsilon^e}_1 - {\varepsilon^p}_1 = -\varepsilon_1 = \frac{q}{E_i\left(1 - \frac{q}{q_a}\right)} \tag{20}$$

The yield condition $\bar{f} = 0$ can be represented in a ***p'-q*** space (for constant value of γ^p) via the yield loci. **Figure 2-7** illustrates the shape of the yield loci, that depends on the exponent

m. For *m=1,* loci will be a straight line, while lower *m*-values will represent slightly curved loci.

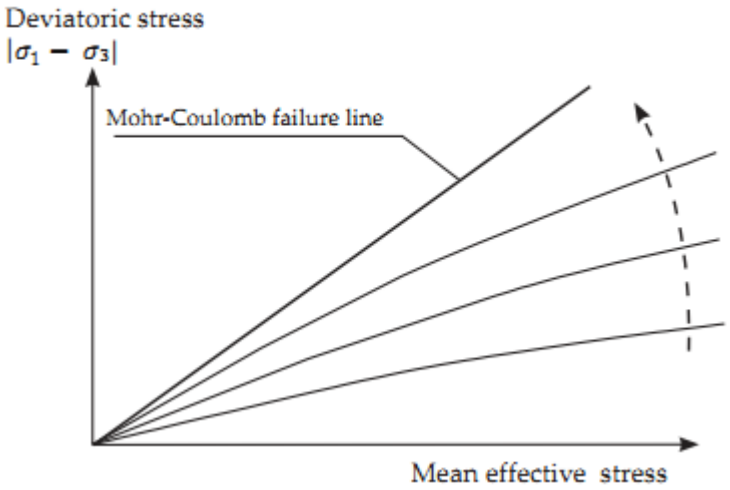

Figure 2-5: Successive yield loci for various constant values of the hardening parameter v_{ur} (Brinkgreve et al. 2017).

Hardening Soil model works with a relationship between plastic and volumetric strains:

$$\varepsilon_v{}^p = sin\psi_m \gamma^p \tag{21}$$

where ψ_m is the mobilized dilatancy angle, defined for this constitutive model as:

$$for\ sin\varphi_m < \frac{3}{4sin\varphi};\qquad \psi_m = 0 \tag{22}$$

$$for\ sin\varphi_m \geq \frac{3}{4sin\varphi}\ \ and\ \psi > 0;\ sin\psi_m = \max\left(\frac{sin\varphi_m - sin\varphi_{cv}}{1 - sin\varphi_m sin\varphi_{cv}}, 0\right) \tag{23}$$

$$for\ sin\varphi_m \geq \frac{3}{4sin\varphi} and\ \psi \leq 0\ \varepsilon_v{}^p = sin\psi_m \gamma^p;\ \ \psi_m = \psi \tag{24}$$

$$for\ \varphi = 0;\quad \psi_m = 0 \tag{25}$$

$$sin\varphi_m = \frac{\sigma'_1 - \sigma'_3}{\sigma'_1 + \sigma'_3 - 2c\ cot\theta} \tag{26}$$

where φ_m is the mobilized friction angle and φ_{cv} is the critical state friction angle, a material constant which is independent of density. For small values of φ_m, negative ψ_m, or when $\varphi = 0$, ψ_m is taken as zero. As given by the stress-dilatancy theory, dilatancy will occur for high stress ratios $\varphi_m > \varphi_{cv}$, and contraction will occur for small stress ratios. When failure occurs ($\varphi = \varphi_{cv}$):

$$sin\varphi_{cv} = \frac{sin\varphi - sin\psi}{1 - sin\varphi sin\psi} \tag{27}$$

For controlling excessive material dilatancy behavior after extensive shearing process, Hardening Soil model counts with a dilatancy cut-off in which the mobilized friction angle is set back to zero when volume change results in a state of the maximum void (e_{max}), as shown in **Figure 2-8**.

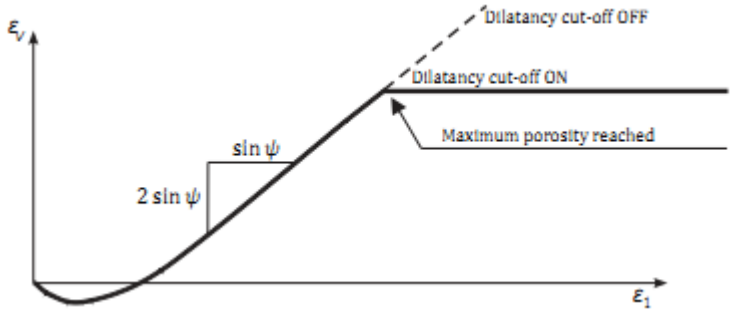

Figure 2-6: Resulting strain curve for a standard drained triaxial test when including dilatancy cut-off (Brinkgreve et al. 2017).

The void ratio is related to the volumetric strain by the following relationship:

$$-\left(\varepsilon_v - {\varepsilon_v}^{init}\right) = \ln\left(\frac{1+e}{1+e_{init}}\right) \tag{28}$$

$$for\ e < e_{max};\quad sin\psi_m = \frac{sin\varphi_m - sin\varphi_{cv}}{1 - sin\varphi_m sin\varphi_{cv}} \tag{29}$$

$$for\ e > e_{max} = \ln\left(\frac{1+e}{1+e_{init}}\right);\ \psi_{mob} = 0 \tag{30}$$

Schanz et al. (1999) introduced in the model's formulation a new yield surface in order to account for the plastic volumetric strain measured during isotropic compression (commonly observed in soft soils). This yield surface which works under compressive stress paths is considered as a cap surface that allows the model to have independency between ${E_{oed}}^{ref}$ and ${E_{50}}^{ref}$. Parameter ${E_{50}}^{ref}$ mainly controls the plastic strains associated with the shear yield surface, while ${E_{oed}}^{ref}$ controls the plastic strains arising from the yield cap. The yield cap surface takes the following shape:

$$f^c = \frac{q^{-2}}{M^2} + p'^2 - {p_p}^2 \tag{31}$$

Figure 2-7 illustrates the yield surface. The ellipse on which the yield cap is located has a length p_p on the *p'-axis* and Mp_p on the *q-axis.* M is an auxiliary parameter of the model related to ${K_0}^{NC}$. In a *p'-q* space, the yield cap f^c is part of an ellipse with its center point in the origin. In the special case of the triaxial state $\sigma 2 = \sigma 3$**,** $p' = (2\sigma_3 - \sigma_1)/3$, and $q = \sigma_1 - \sigma_3$**,** the magnitude of the yield cap is determined by the isotropic consolidation stress p_p.

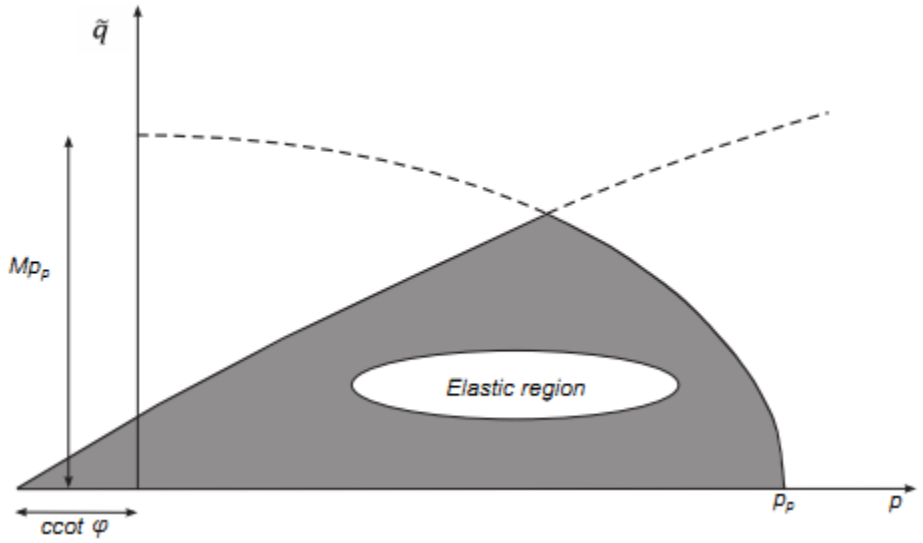

Figure 2-7: Yield surfaces in the *p* – *q* plane. The elastic region can be further reduced by means of a tension cut-off (Brinkgreve et al. 2017).

The fully understating of the Hardening Soil model yield surfaces should be focused on both **Figure 2-7** and **Figure 2-8**. The first one reflects the yield lines and the second one is related to the yield contour in the principal stress space. It should be noted that shear and cap surfaces keep the hexagonal shape of Mohr-Coulomb failure criterion, having the shear yield surface the possibility to expand up to the ultimate failure surface (Mohr-Coulomb), and the cap surface can expand according to the pre-consolidation stress.

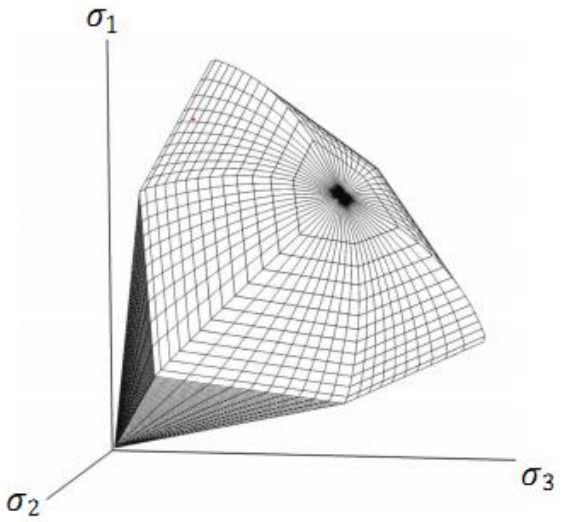

Figure 2-8: Representation of the total yield contour of the Hardening Soil model in the principal stress space for cohesionless soils (Brinkgreve et al. 2017).

To account for the very small-strain soil stiffness and its non-linear dependency on strain amplitude, the Hardening Soil model with small-strain stiffness (HSsmall) model was developed by Benz (2006). This model is an extension of the strain history dependent and multi-axial Hardin-Drnevich model (1972). In comparison to the standard Hardening Soil model, HSsmall has only two additional parameters: the initial or very small-strain shear modulus, G_0; and the shear strain at 70% of the G_0, $\gamma_{0.7}$. For triaxial conditions, the tangent shear modulus, which defines the shear stiffness degradation curve, can be expressed as:

$$G_t = \frac{G_0}{\left(1 + 0.385\frac{\gamma}{\gamma_{0.7}}\right)^2} \tag{32}$$

where G_t corresponds to the tangent shear modulus and γ to the shear strain. In this model, stiffness degradation due to plastic strains is computed with strain hardening effects, and the degradation curve is bounded by certain lower limits (tangent shear modulus cut-off, G_{ur}, and shear strain cut-off, $\gamma_{cut-off}$) which can be determined by laboratory tests.

$$G_t \geq G_{ur}; \quad where \;\; G_{ur} = \frac{E_{ur}}{2(1+\mu_{ur})} \;\; and \quad G_t = \frac{E_t}{2(1+\mu_{ur})} \tag{33}$$

$$\gamma_{cut-off} = \frac{1}{0.385}\left(\sqrt{\frac{G_0}{G_{ur}}} - 1\right)\gamma_{0.7} \tag{34}$$

The tangent shear modulus, G_t, and tangent Young's modulus, E_t, works under stress-dependency considering a constant Poisson's ratio, μ_{ur}, following the power law presented

in Equation (11), replacing E_{ur} by E_t. An example of a stiffness degradation curve corresponding to HSsmall model is shown in **Figure 2-20**.

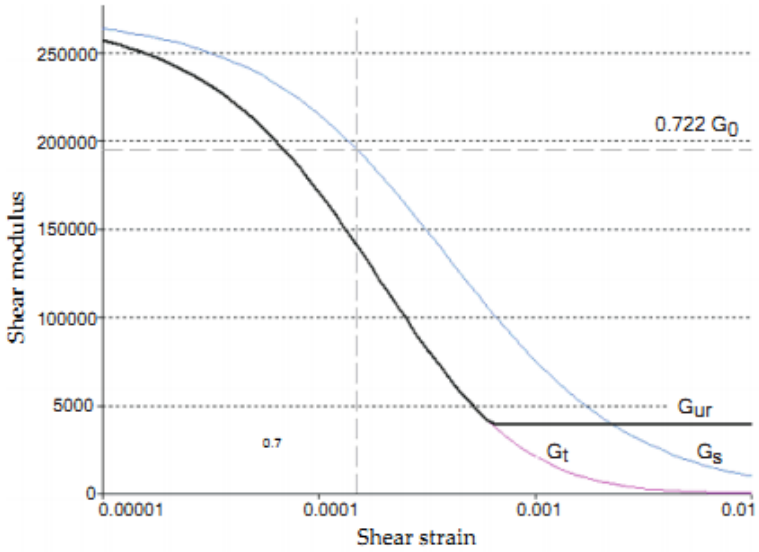

Figure 2-9: Secant and tangent shear modulus reduction curve (Brinkgreve et al. 2017).

HSsmall computes a more rapid decrease of small-strain stiffness during virgin loading than for reloading processes, due to the hardening plasticity. It must be remarked that while parameter G_0 is numerically dependent on the stress-state of the material, the parameter $\gamma_{0.7}$ is numerically independent, but physically both are influenced by actual material void ratio and stress state. On sedimentary soils the stiffness degradation not necessarily implies the microstructure destruction, unless the soil skeleton suffers from breakage. On residual soils, certain level of stiffness degradation might affect the structure so that the fabric suffers irreversible destruction. The user of the constitutive model must have consider the state of the soil structure corresponding to a 70% of the degradation of its G_0.

An important difference between Hardening Soil and HSsmall models is related to the dilatancy.

Figure 2-10 illustrates the relationship between the dilatancy angle and the mobilized friction angle. For the HSsmall, when parameter ψ_m is negative, the mobilized dilatancy is computed as:

$$\sin(\psi_m) = \frac{1}{10}\left(-M_c exp^{\left[\frac{1}{15} ln\left(\frac{M_c\ q}{M_d q_a}\right)\right]} + M_d\right) \quad (35)$$

$$M_c = \frac{6\sin(\varphi_{cv})}{3 - \sin(\varphi_{cv})} \quad (36)$$

$$M_d = \frac{6\sin(\varphi_m)}{3 - \sin(\varphi_m)} \quad (37)$$

$$\frac{q}{q_a} = max\left(\frac{1 - \sin(\varphi_{cv})}{\sin(\varphi_{cv})} . \frac{\sin(\varphi_m)}{1 - \sin(\varphi_m)}\ , 10^{-4}\right) \quad (38)$$

$$\text{and mobilised friction angle is limited to } \sin(\varphi_m) \geq \frac{\sin(\varphi_{cv})}{2 + \sin(\varphi_{cv})} \quad (39)$$

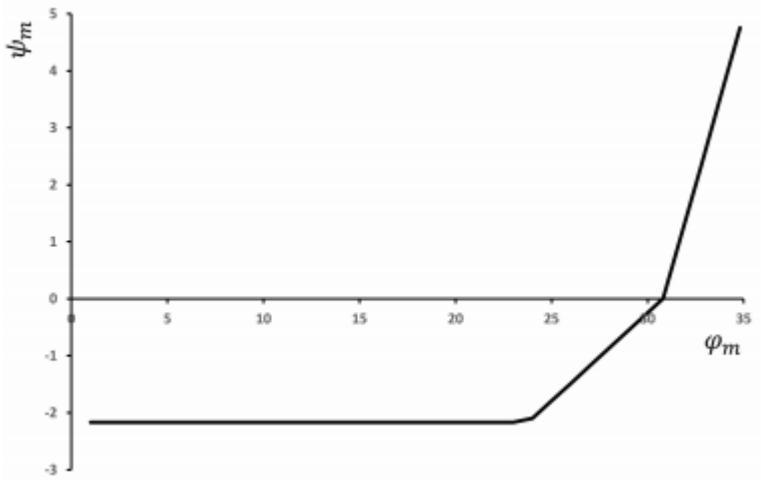

Figure 2-10: Plot of the mobilized dilatancy angle ψ_m and mobilized friction angle φ_m for Hardening Soil model with small-strain stiffness (Brinkgreve et al. 2017).

Both Standard Hardening Soil and HSsmall models do not account for softening due to dilatancy and de-bonding effects, which is an important limitation. Also, the hardening effect captured by models is always isotropic, and are not capable to distinguish between different strain and stiffness levels, so that the user must select a set of parameters in accordance with expected strain levels. HSsmall model is not very suitable for modeling the same material at different void ratios with a single set of material parameters, mainly because of its void ratio independent formulation.

2.1.3 Hypoplastic clay model

The Hypoplastic clay model was proposed by Mašín (2005) and enhanced later by (Mašín and Herle, 2005). It is a constitutive inelastic and non-linear incremental model that does

not require the definition of a yielding surface or decomposing the strains into elastic and plastic parts; thus, it does not work with yield surface and plastic potential definitions. The Hypoplastic clay model can predict the state boundary surface, combining the mathematical formulation of common Hypoplastic models with the basic principles of the critical state soil mechanics. As for to the 3SKH model, the Hypoplastic model predicts non-linear behavior inside the state boundary surface, and therefore it does not suffer from shortcomings of the Cam Clay models.

The hypoplastic constitutive equations can be described by a simple non-linear tensorial equation that represents the stress rates as a function of the strain rates and the initial state variables such as initial void ratio and initial stress state. Stress and strain rates can be understood as an increment obtained in a certain time unit. Lanier et al. (2004) showed that the general hypoplastic equation for early models can be written as:

$$\dot{\mathrm{T}} = \mathcal{L} : D + N\|D\| \tag{40}$$

with $\mathcal{L}$ and N as a fourth-order tensor and D as second-order tensor that are functions of the Cauchy stress, T.

The theory of hypoplasticity was first developed for coarse-grained soils by Kolymbas (1978) and has been the basis of many constitutive soil models nowadays. Kolymbas (1978) model was latter improved by Gudehus (1996), who introduced the critical state concept by including the effects of density with a pyknotropy scalar factor, f_d, and stress level of materials with a barotropy scalar factor, f_s [see Equation (41)]. More after, von Wolffersdorff (1996) added the Matsuoka-Nakai critical state stress condition. To achieve this, a tensorial function was included in Equation (42). This led to the definition of a hypoplastic flow rule [see Equation (43)] with Equation (44) for the critical state, f as the stress function, and B as a constitutive tensor:

$$\dot{\mathrm{T}} = f_s\mathcal{L} : D + f_s f_d N\|D\| \tag{41}$$

$$B = \mathcal{L}^{-1} : N\|D\| \tag{42}$$

$$\vec{D} = -B \tag{43}$$

$$f = \|B\| - 1 \tag{44}$$

Niemunis (2002) defined the flow rule, critical state stress condition, and tensor $\mathcal{L}$ independently by proposing a modification of the basic Equation (40). The resulting formulation describes the relationship between stress and strain, and it was named "generalized hypoplasticity" [see Equation (45)].

$$\dot{\mathrm{T}} = f_s \mathcal{L} : \left(D - f_d Y \frac{m}{\|m\|} \|D\| \right) \tag{45}$$

where m is a second-order tensor and Y is a scalar quantity that represents a limit stress condition.

Since this enhanced model was still based on the von Wolffersdorff (1996) initial model, those formulations were not capable to reproduce shear stiffness independency of the bulk stiffness. Thus, the shear stiffness was underpredicted. Herle and Kolymbas (2004) proposed a Hypoplastic model which could reproduce this stiffness independency, but it still assumed the same pyknotropy and barotropy of von Wolffersdorff (1996) model which was not accurate for clays, and nor did it consider the "generalized hypoplasticity" [Equation (45)]. Herle and Kolymbas (2004) model is taken by Mašín (2005) as the reference model for further modifications.

Herle and Kolymbas (2004) modified the von Wolffersdorff (1996) model in order to separate shear and bulk stiffness by modifying the hypoelastic tensor $\mathcal{L}$ and introducing a new constitutive parameter, r, which controls the ratio of shear and bulk modulus at isotropic stress states. Two scalar factors c_1 and c_2 are introduced by Mašín (2005), where c_1 is employed to guarantee the coupling of the parameter r, and c_2 to guarantee coupling between Herle and Kolymbas (2004) and von Wolffersdorff (1996) models.

Considering that Herle and Kolymbas (2004) model is not based on the "generalized hypoplasticity" [Equation (45)], scalar factors c_1 and c_2 are not valid for the stresses condition approaching the critical state on Matsuoka-Nakai criterion. Thus, another scalar factor, ξ, is introduced. Equation (46) and Equation (47) show the expression for scalar

factors c_1 and c_2, respectively, and Equation (48) shows the formulation for the scalar factor ξ.

$$c_1 = \left(\frac{1 + \frac{1}{3}\alpha^2 - \frac{1}{3}\alpha}{1.5r} \right) \tag{46}$$

$$c_2 = 1 + (1 - c_1)\frac{3}{\alpha^2} \tag{47}$$

where α is a scalar factor derived from critical state friction angle related to the von Wolffersdorff (1996) model.

$$\xi = \langle \frac{sin\varphi'_c - sin\varphi'_{mob}}{sin\varphi'_c} \rangle \tag{48}$$

$$sin\varphi'_{mob} = \frac{T_1 - T_3}{T_1 + T_3} \tag{49}$$

φ'_{mob} refers to the mobilized friction angle, while T_1 and T_3 refers respectively to the maximal and minimal principal stresses.

The basic Hypoplastic model previously described works accurately for soils subjected to monotonic loads at strains levels larger than 0.1%. The soil response with the basic model can be improved by incorporating the ***intergranular strain concept***, which allows capturing soil behavior at strains levels smaller than 0.1% and a more accurate response upon cyclic loading. This improved concept was proposed by Niemunis and Herle (1997):

$$\dot{\mathrm{T}} = \mathrm{M} : D \tag{50}$$

The formulation of this concept consists in introducing the state variable δ, and a fourth-order tangent stiffness tensor of the material, M. Total strain is taken as the sum of the deformation given by the rearrangement of soil skeleton and the deformation of interface

layers (δ). Niemunis and Herle (1997) defined basically three cases in which the soil response in terms of strain could be set:

$$\text{For reverse loading conditions,} \quad \hat{\delta} : D < 0$$
$$\text{For neutral loading conditions,} \quad \hat{\delta} : D = 0$$
$$\text{For continuous loading conditions,} \quad \hat{\delta} : D > 0$$

For reverse and neutral loading cases, strain is given only by deformation on the intergranular interface layer with a hypoelastic response, whereas for continuous loading, the observed response takes into account the rearrangement in the skeleton. Mathematical structure is fully detailed by Mašín (2005).

Reached this point, the Hypoplastic model (Herle and Kolymbas, 2004) still presented some limitations when predicting fine-grained soils behavior. Main shortcomings are listed below:

- Investigations conducted by Viggiani and Atkinson (1995) and Teachavorasinskun and Amornwithayalax (2002) have shown that the small strain shear modulus, G_0, on clays inside the yield surface highly depends on the mean stress, p, while deviatoric stress, q, was not very significant, for both triaxial compression and extension conditions. Herle and Kolymbas (2004) model predictions showed a notorious reduction in G_0 with the ratio q/p.
- According to the critical state soil mechanics for clays (Schofield and Wroth, 1968), it is reasonable to consider the lower limit of void ratio $e = 0$, but Herle and Kolymbas (2004) model assumes a pressure-dependent and a non-zero lower limit for the void ratio (reasonable for coarse-grained materials). This leads to incorrect predictions of stress-dilatancy on clays.
- Isotropic compression and critical state lines for clays are better represented by logarithmic expressions, taking into account typical stress ranges in geotechnical engineering, however the Herle and Kolymbas (2004) basic Hypoplastic model assumes an exponential expression, what despite allowing one to have evaluation limits for the mean stress $p \to 0$ and $p \to \infty$, it results in the disadvantage of having an additional parameter.

- In the Herle and Kolymbas (2004) basic model, the slope of the isotropic unloading line is given by variables α and β, so that the swelling index k^* cannot be specified by the user. This is unhelpful because these two variables are not easily estimated from an isotropic unloading test.
- The Herle and Kolymbas (2004) basic model considers a parameter e_{c0}, which defines the position of the critical state line in the *e-p* space, and this results not very simple for its true applicability. As considered by Mašín (2005), the Modified Cam Clay model is suitable for evaluating the position of the critical state line on clays.

The lack of a suitable hypoplastic formulation for fine grained soils led to the development of the model proposed by Mašín (2005). This model considers principles of the traditional critical state soil mechanics and basic hypoplasticity theory. Constitutive parameters required by the model are similar than Modified Cam Clay model, which are not difficult to calibrate with standard laboratory tests, making the model suitable for practical applications.

Modifications and new formulations for tensor $\mathcal{L}$, limit stress condition, Y, hypoplastic flow rule (tensorial quantity m), barotropy factor, f_s, and pyknotropy factor, f_d, scalar factors, c_1 and c_2, and their respective relationship with stress state, material stiffness, and compressibility dependent variables, are fully explained by Mašín (2005).

Mašín (2005) enhanced the reference Herle and Kolymbas (2004) model by correcting the underprediction of the initial shear stiffness tests starting from anisotropic stress conditions, which resulted on a shortcoming for field applications since those conditions are very common in the field. This new formulation led to more accurate predictions of undrained stress paths.

As mentioned, the basic Hypoplastic model for clays works with five constitutive parameters, which are equivalent (but not identical) to the parameters of the Modified Cam Clay. The main five constitutive parameters of this basic model required for model calibration are N, λ^*, k^*, μ_{pp} and φ'_c. **Figure 2-11** shows three of these parameters, represented in $ln(1+e)$- $ln(p)$ space, and can be obtained from one-dimensional compression (oedometer) tests or isotropic compression tests. In this work, these

parameters were obtained from incremental loading (IL) and constant rate of strain (CRS) oedometer tests and triaxial tests following oedometric stress paths, which were conducted and explained in detail by Galeano (2020). Parameter k^* represents the isotropic unloading line slope, parameters N and λ represents the position and slope of the isotropic compression line, respectively. The ratio λ^* / k^* controls the size of response envelope and the response in undrained conditions in terms of stress paths.

Parameter φ'_c is the critical state friction angle, which according to Mašín (2015) is preferably measured on reconstituted, normally consolidated soil samples via undrained triaxial tests. Parameter μ_{pp} controls the shear stiffness. The larger the value of μ_{pp}, the smaller the shear modulus. This parameter also controls the shape of response envelope, and consequently undrained stress paths. According to Mašín (2015), it should be preferably calibrated from undrained shear tests on undisturbed soil.

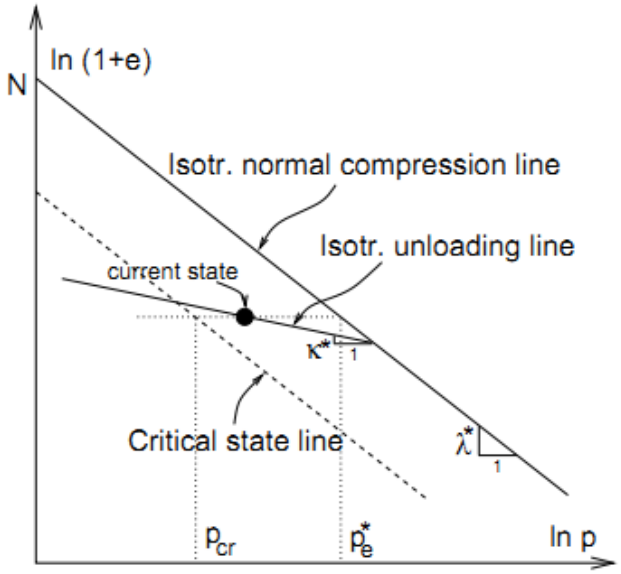

Figure 2-11: Definition of parameters N, λ^* and k^*, taken form (Mašín 2005).

Table 2-3 summarizes the basic Hypoplastic model parameters that have been identified for different soils in the world. With exception of the parameters corresponding to Chicago clay, all of them were compiled by Mašín (2017). All data shown in **Table 2-3** corresponds to sedimentary geological conditions.

Table 2-3: Basic Hypoplastic model constitutive parameters for different soils (After Mašín, 2017; Arboleda-Monsalve et al. 2017)

Sites	Constitutive Parameters - Basic Hypoplastic model					
	φ'_c [°]	λ^*	k^*	N	μ_{pp}	Geological Origin
Brno clay	22	0.128	0.015	1.51	0.33	Neogene clays (Paratethys Sea sediments).
London clay	21.9	0.095	0.015	1.19	0.1	Marine deposits during Eocene period.
Karlsruhe Kaolin	27.5	0.065	0.01	0.918	0.35	Sedimentary deposit, Upper Cretaceous period. Transportation of weathered parental granites and gneisses rocks.
Dortmund clay	27.9	0.057	0.008	0.749	0.38	Overconsolidated illitic clay from tertiary deposits overlying coal seams.
Weald clay	24	0.059	0.018	0.8	0.3	Estuarine deposit of the Cretaceous period (Heavily overconsolidated in its natural state).
Koper clay	33	0.103	0.015	1.31	0.28	Quaternary marine deposits.
Fujinomori clay	34	0.045	0.011	0.887	0.36	Volcanic ash deposit.
Pisa clay	21.9	0.14	0.01	1.56	0.31	Alluvial (Holocene-Pleistocene) deposits of the Arno River.
Beaucaire clay	33	0.06	0.01	0.85	0.21	Shallow marine deposit, Pliocene age. Heavily overconsolidated.
Trmice clay	18.7	0.09	0.01	1.09	0.09	Deposition during the Quaternary period, specifically during the Pleistocene.
Chicago Clay	29	0.062	0.011	0.76	0.15	Ice marine deposits of the Wisconsinan stage of the Pleistocene glacial epoch.
Min. value	*18.7*	0.045	0.008	0.749	0.09	
Max. value	*34*	0.14	0.018	1.56	0.38	
Avg. value	*26.6*	0.082	0.012	1.056	0.26	

Mašín (2018) indicates that the advanced parameter α_f controls the translation of the response envelope without modifying its shape. This constitutive parameter has a similar influence than μ_{pp} on the mechanical behavior at large strains, but with some differences. Parameter α_f decreases the rate of stiffness degradation without noticeable influence on the initial soil stiffness, while changes in μ_{pp} influences the initial stiffness. Mašín (2018) stated that the calibration of parameter α_f could be considered as an advanced calibration. The influence of the parameters α_f and μ_{pp} are shown respectively in **Figure 2-12** and **Figure 2-13**.

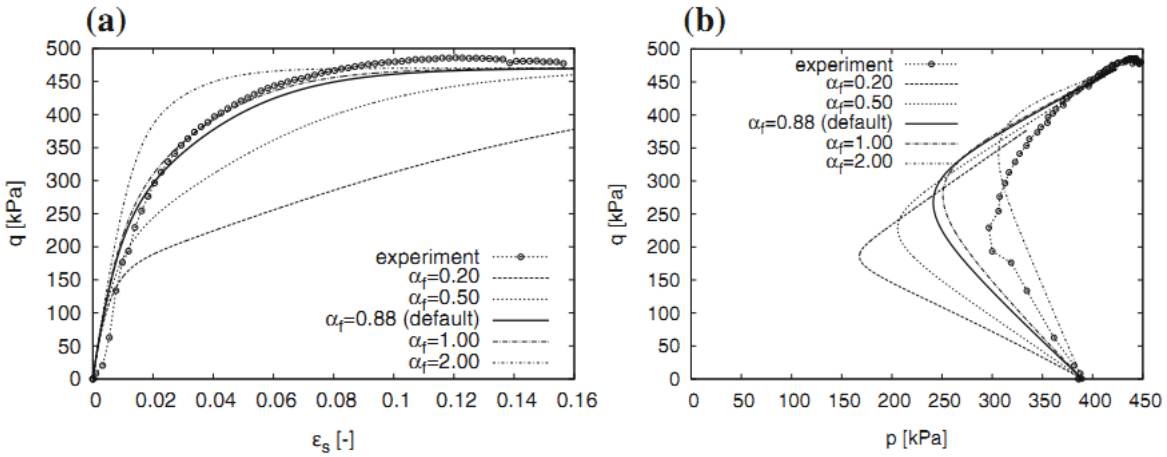

Figure 2-12: The effect of α_f on (a) stress-strain curves and (b) stress paths of undrained triaxial tests (Mašín, 2018).

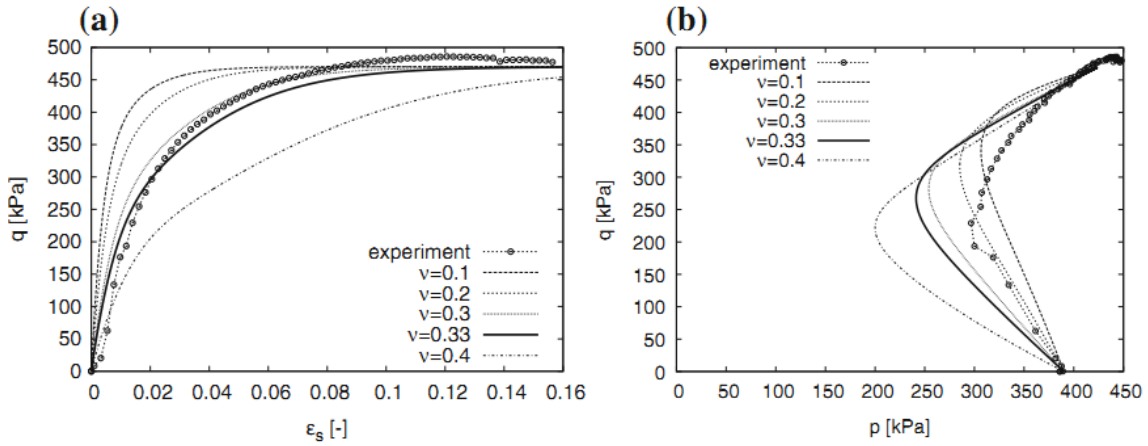

Figure 2-13: Calibration of the parameter μ_{pp} using undrained triaxial tests on Dortmund clay. (a) Stress-strain curves, and (b) stress paths (Mašín, 2018).

As mentioned, the basic Hypoplastic model is useful for predicting only soil responses at large strain levels (*i.e.,* >0.1%), but this was overcome by the addition of intergranular strain concept (Niemunis and Herle, 1997). The intergranular strain tensor is capable of representing the stress history of materials. At this point, model response comprises particle rearrangement of soil skeleton and deformation of intergranular strain layer between soil grains for continuous loading condition, while under reversal of loading direction strains are related only to the intergranular interface at small strain levels.

Intergranular strain concept is incorporated into the model by the addition of six parameters, which are related to the small strain behavior of soils: A_g, n_g, m_{rat}, R, β_r, and χ. The very small strain shear stiffness (small strain shear modulus) is mainly controlled by parameter m_{rat}, considering an initial and 180° strain path reversal loading, supplemented by parameters A_g and n_g. m_{rat} correspond to the very small strain behavior upon strain path reversals and represents the ratio m_T/m_R.

- m_R: parameter controlling the initial (very-small-strain) shear modulus upon 180° strain path reversal respect to the initial loading.
- m_T: parameter controlling the initial shear modulus upon 90° strain path reversal.

Mašín (2015) asserts that this parameter "is difficult to calibrate". The ratio m_{rat} is the ratio G_{90}/G_0, where G_{90} is the initial shear stiffness after 90° change of strain path direction. G_{90} cannot be measured by bender element tests. Identification of this parameter needs accurate strain measurements using local instrumentation. Mašín (2015) recommends obtaining this parameter from parametric analysis.

Parameter R determines the size of the elastic range in the strain space (degradation curves), while β_r and χ control the rate of degradation of the stiffness with strain. If there is an increment on χ or if β_r decreases, it will lead to a stiffer stress-strain response in the model. These parameters need to be calibrated by means of a parametric study by fitting the stiffness degradation curve obtained using accurate local strain measurement, (Mašín, 2015).

Mašín (2015) performed a parametric study in which the influence of the constitutive parameters of the intergranular strain concept on the soil stiffness degradation response was evaluated. **Figure 2-14** shows that parameters β_r, and χ have a similar influence on the stiffness degradation curve, but inversely. For higher values of χ parameter, the soil shows a stiffer response, while for higher of β_r values, the soil stiffness response is softer. As parameter R controls the size of the elastic range of the degradation curve, higher values of this parameter will cause stiffer responses at very small strain levels.

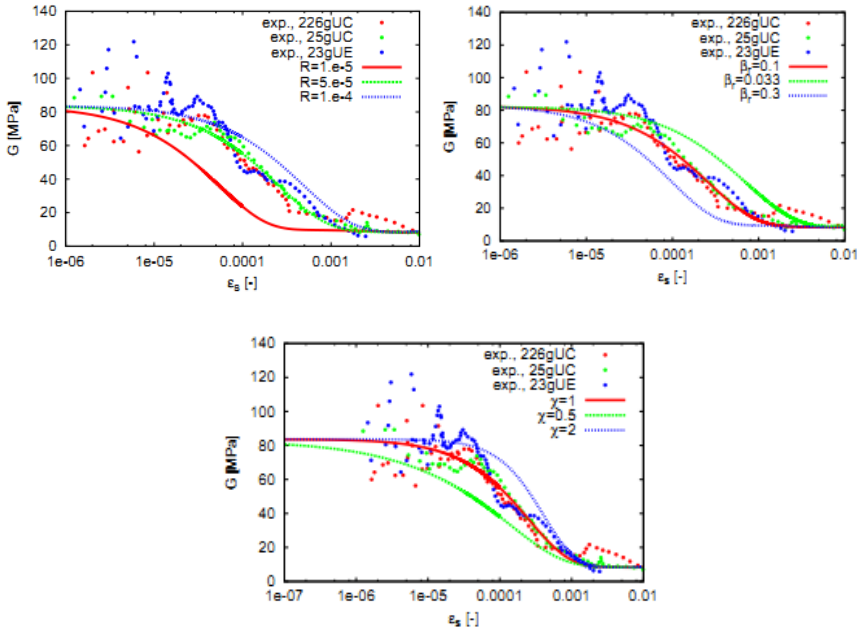

Figure 2-14: Influence of parameters R, β_r, and χ on stiffness degradation, taken from (Mašín 2015).

Table 2-4 summarizes constitutive parameters of the Hypoplastic model enhanced with the intergranular strain concept for different soils in the world. With exception of the parameters corresponding to Chicago clay, all of them were compiled by Mašín (2017).

Table 2-4: Intergranular strain concept constitutive parameters for different soils, (After Mašín, 2017; Arboleda-Monsalve et al. 2017)

Sites	Constitutive Parameters					
	A_g	n_g	m_{rat}	R	β_r	χ
Hochstetten sand	-	-	0.40	1E-04	0.50	6.0
Karlsruhe sand	-	-	-	5E-04	0.30	1.0

Sites	Constitutive Parameters					
	A_g	n_g	m_{rat}	R	β_r	χ
London clay nat.	270	1.0	0.50	5E-05	0.08	0.9
Brno clay	5300	0.5	0.50	1E-04	0.20	0.8
Koper silty clay	-	-	1.00	2E-05	0.09	0.7
Chicago Clay	4100	0.6	1.00	5E-05	0.18	1.3
Min. value	270	0.5	0.40	2E-05	0.08	0.7
Max. value	5300	1.0	1.00	5E-04	0.50	6.0
Avg. value	3223	0.7	0.68	1E-04	0.23	1.8

Unlike data shown in **Table 2-3**, **Table 2-4** shows also parameters corresponding to sandy soils, what means that the Hypoplastic constitutive model has been also implemented for coarse-grained soils in numerical simulations. It can be noticed that parameters A_g and n_g are only presented for three of the six sites compiled by Mašín (2017), and the total amount of available information regarding the parameters of the intergranular strain concept parameters is less than for the basic model. This suggests that the identification of parameters of the intergranular strain concept require more complex procedures.

The constitutive model can be initialized by specifying a constant OCR (which is then scalable by the mean effective stress), or one can specify a constant void ratio. These methods are illustrated in **Figure 2-15**. The selection of a constant void ratio must match with the OCR definition of the model, which does not consider the preconsolidation pressure p_p, but the Hvorslev's equivalent pressure, p_e, which represents basically the void ratio corresponding to a given mean stress (or vice versa), so that $OCR = p_e/p$ [see Equation (51)].

$$e = \exp[N - \lambda^* \, ln(OCR) * p] - 1 \tag{51}$$

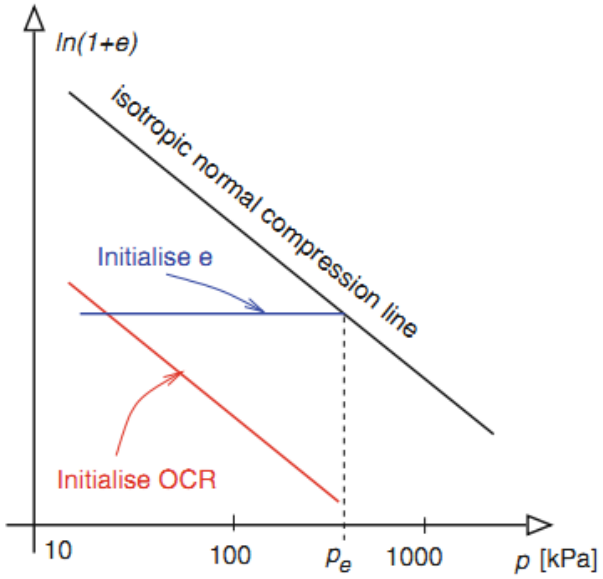

Figure 2-15: **T**wo methods of initialization of the void ratio for the Hypoplastic clay model in finite element simulations: the first method labelled as “initialize e” and the second method labelled as “initialize *OCR*” (Mašín 2018).

Mašín (2017) recommends to initialize the model as follows:

$$if\ initialization\_par < 10, use\ \text{e}$$
$$if\ initialization\ parameter > 10, OCR = initialization_{par} - 10$$

According to Másin (2018), both initialization methods are applicable for clays, but for stiff clays, it is suggested to specify a constant void ratio. In this research, OCR was obtained from several compression tests conducted by Galeano (2020), which’s results led to an average apparent overconsolidation ratio $AOCR \approx 4$ (see chapter 2.3). Thus, the model was initialized with the void ratio, corresponding to the in-situ effective stress conditions, according to the recommendations provided by Másin (2017; 2018).

The parameter Pt corresponds to a shift of the mean stress due to cohesion. According to Mašín (2017), a non-zero value is needed in order to overcome initial stress problems such as stress-free condition prior to a loading process. In this research, Pt was assumed to be equal to the intercept of cohesion of the material.

One of the limitations of the Hypoplastic clay model is the influence of the ratio λ^* / k^*, leading to unrealistic results for low values, reflected on stress-strain soil behavior and the

boundary surfaces shape. Also, under undrained conditions and normally consolidated states, it is typical that the soils exhibit a first shearing path close to be perpendicular to the *p'* axis, and then while higher deviatoric stresses are applied the curve starts to show the progressive reduction in *p'.* This shortcoming is attributed to all the purely hypoplastic-based models which their formulation counts with a translated elliptical response envelope.

2.2 Parameter Optimization

The constitutive parameters of any soil model control the mechanical response. Therefore, their determination is essential to adequately capture observed responses in laboratory testing. Recommendations to calibrate constitutive soil parameters are found in the technical literature and depend on the results of specific laboratory tests and/or the numerical simulation of specific conditions at a laboratory scale. For identifying the best fit between model and laboratory data, inverse analysis techniques will be applied, among which the nonlinear equations stand out. This corresponds to a mathematical routine with the weighted least-squares fit to optimize the process of searching for the parameters that most closely match the experimental information.

Numerical soil modeling will be always associated with several uncertainties related to different factors such as assumptions made in the procedures, precision of the utilized computational tool, approximations to convert a physical scenario into a numerical model (which includes engineering judgment), among others. Another group of important sources of uncertainty are related to the investigated medium, the soil, which carry on with variability of strata and material properties (both in area and depth). A well-founded numerical soil model must start from field or laboratory data that can be considered as observations, which are always limited in terms of funding or time that leads into more uncertainties for the analysis.

Despite uncertainties are sometimes recognized, they are not always quantified and involved in the numerical results or procedures. The accurate recognizing and quantification of uncertainties is one of the first steps that should be followed in order to overcome the problems of the numerical model fit caused mainly by inappropriate input data. A model calibration is basically the way of how some parts (*e.g.,* parameters or

conditions) are changed in order to achieve an accurate fit between measured values (*e.g.*, laboratory or field results) and computed values. Currently, several numerical techniques are available to enhance model calibration, but one of the most employed techniques during the last 10 years is the inverse modeling. Inverse modeling procedures or optimization procedures basically consists of iteratively changing the numerical model input data (*e.g.*, constitutive soil parameters) until computed values match "satisfactorily" the observed available data. As specified by Sarabia (2012), the accuracy of this technique depends strongly in the quantity and quality of the available observations and the quantity of parameters or conditions to be optimized. More model input data to be optimized will require more representative observations to achieve a "correct" fit between model results and experimental data. According to Calvello (2002), the initial set of parameters of a constitutive soil model should be, as far as possible, initially estimated by means of laboratory or field procedures. The initial set is utilized to compute the model and compare results with the target data. The schematic procedure of parameter optimization technique is presented in **Figure 2-16**.

One of the main benefits of parameter optimization in terms of inverse modeling is the replacement of trial-and-error methods which represent an important time demand. Constitutive parameters identification can be better determined with optimization techniques, achieving more reliability. However, parameter definition by means of inverse analysis methods may be subjected to some issues:

- Little changes on parameters can cause notorious changes on soil computed response, what is known as instability.
- Parameters modification does not cause any changes on computed soil response, what is known as insensitivity.
- Different parameters values cause "acceptable" model fit, what is known as non-uniqueness. This situation is strongly correlated with almost all numerical methods typically employed in optimization techniques.

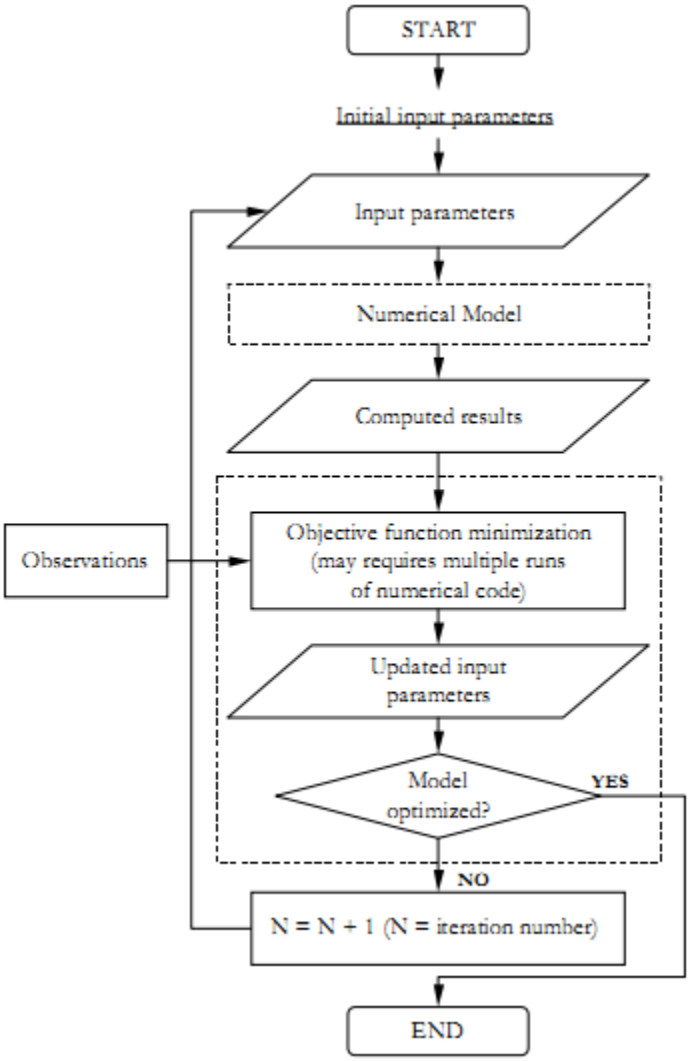

Figure 2-16: Scheme of a basic inverse analysis procedure, taken from (Calvello, 2002).

Authors such as Poeter and Hill (1998), Hill (2000), Calvello (2002), and Sarabia (2012) showed that inverse modeling for parameter estimation represents a valuable tool for soil numerical simulation.

Since the main objective is to match the computed values with the observations, a careful selection of these last is critical to achieve accurate optimization analysis results (Sarabia, 2012). If there are errors in one or more observations, it is possible that the final numerical simulation does not represent the real soil behavior. For this work, all the observations correspond to the laboratory triaxial tests results conducted on Caldas residual soils,

specifically for undrained compression and reduced triaxial extension paths (Galeano, 2020).

Once the observations are defined, the constitutive parameters are selected for the optimization (inverse analysis) process. For this purpose, one must assess the parameters influence on the objective function and their correlation magnitude. The selected parameters for inverse analyses must represent enough sensitivity on the objective function and also exhibit a non-high correlation in order to overcome the issues mentioned in paragraphs above. In order to compare the initial and final (optimized) conditions of the problem, the objective function fit should be measured. Hill (2000) presents some statistical methods of inverse modeling using nonlinear simple regressions to analyze the mentioned points.

The weighted least-squares objective function, $S(b)$, is used to represent a quantitative measure for the fit or match between observed and computed data. It can be expressed as:

$$S(b) = [y - y'(b)]^T \omega [y - y'(b)] = e^T \omega\, e \tag{52}$$

where:

- y is the observation being matched by the regression.
- $y'(b)$ is the vector containing the computed values.
- ω is the observations weight matrix.
- b is the vector containing the parameters to be optimized.
- e is the residual vector.

The objective function value can be used informally to measure the model fit. The better the response fit, the smaller the $S(b)$ value. The $S(b)$ value tends to decrease as more parameters are added to the evaluation, which can lead to confusing results. For a more formal convergence evaluation, the error variance, s^2, is implemented (Hill, 2000).

$$s^2 = \frac{S(b)}{ND - NP} \tag{53}$$

where ND corresponds to the total number of observations and NP to the total number of parameters.

To compare the agreement of the numerical optimized results with the experimental target data, with respect to the initial ones, the fit improvement variable can be computed as:

$$FI = \frac{S(b)_{initial} - S(b)_{optimized}}{S(b)_{initial}} \tag{54}$$

This weighting of the observations corresponds to the importance of each measurement. Weighting process can be highly empirical and could be used to give more influence on statistical results to those observations that are “more trustworthy” and reduce the important of those “less accurate”. Poeter and Hill (1998) and Hill (2000) demonstrated that for inverse analysis to estimate parameters with the smallest possible variance, the assigned weights must be proportional to the inverse of the variance-covariance matrix of the measurement errors. This can be understood as the less observations error the more weight assigned, and vice versa. It is recommended to give more importance to the trustworthy observations. Thus, weight assigning can be expressed with the following Equation:

$$\omega = \frac{1}{\sigma^2} \tag{55}$$

where σ^2 corresponds to the error variance, whose square root (σ) is the standard deviation.

Several statistical procedures can be implemented to evaluate the influence of the estimated parameters on the objective function, correlation between them, influence of observations, among others. Sensitivities allow one to numerically evaluate the relative importance of each parameter involved in the numerical simulation. There are different sensitivity types or quantities which can be estimated for the mentioned purpose, such as

one percent sensitivities (dss_{ij}), scaled sensitivities (ss_{ij}), and composite scaled sensitivities (css_j) [Equations (56), (57), and (58) respectively].

$$dss_{ij} = \frac{\delta y_i'}{\delta b_j}\frac{b_j}{100} \tag{56}$$

$$ss_{ij} = \left(\frac{\delta y_i'}{\delta b_j}\right) b_j\, \omega^{1/2} \tag{57}$$

$$css_j = \left[\frac{\sum_{j=1}^{ND}\left(\left(\frac{\delta y_i'}{\delta b_j}\right) b_j\, \omega^{1/2}\right)^2}{ND}\right]^{1/2} \tag{58}$$

In the previous equations, b_j corresponds to the j_{th} estimated parameter, y_i' to the i_{th} simulated (computed) value, $\frac{\delta y_i'}{\delta b_j}$ is the sensitivity of the i_{th} simulated value with respect to the j_{th} parameter, ND is the total number of observations, and ω is the statistical weight of the i_{th} observation. In these numerical expressions, b is the vector containing the parameter values at which the sensitivities are being evaluated.

Scaled sensitivities (ss_{ij}) and composite scaled sensitivities (css_j) are dimensionless quantities useful to evaluate the importance of several observations on a single parameter or the importance of several parameters on the simulation (objective function), and in both cases a greater sensitivity value represents a higher importance. As shown in Equation (58), composite scaled sensitivities (css_j) are estimated using the scaled sensitivities of all observations and their respective weights.

One percent sensitivities represent the influence of the evaluated parameter in the objective function with that parameter perturbed (increased) in exactly one percent (1%). It must be noted that dss_{ij} formulation does not consider the weight of the observations. One percent sensitivities reflect dimensional quantities and are useful when comparing the importance of different types of observations in an isolated way (not in a composite form).

Composite scaled sensitivities reflect the total amount of information provided by the available observations; therefore, it is probably the most important statistic parameter to identify the importance of the model parameters (Calvello, 2002). Only composite scaled sensitivities will be considered in this work to evaluate relative influence of parameters.

According to Hill (2000), despite composite scaled sensitivities represent good measures related to a single parameter and they are independent of the model fit, its formulation does not consider the fact that numerical simulation involves several parameters simultaneously, and consequently it misses the influence of the parameter's correlation on the model response (objective function). Variance-covariance matrix $V(b')$ can be implemented to estimate the reliability and correlation of the estimated parameters (Hill, 2000).

$$V(b') = s^2(X^T \omega X)^{-1} \tag{59}$$

where $(X^T \omega X)$ is a symmetric square matrix with *NP* by *NP* dimensions, and *NP* is the total number of parameters. s^2 is the calculated error variance and ω is the weights matrix. $V(b')$ is an *NP* by *NP* matrix whose diagonal elements represent the parameters variance and the off-diagonal elements represent parameters' covariance, as shown in the following example of a 3-parameters scenario.

$$\begin{bmatrix} var(1) & cov(1,2) & cov(1,3) \\ cov(2,1) & var(2) & cov(2,3) \\ cov(3,1) & cov(3,2) & var(3) \end{bmatrix}$$

where $var(1)$ is the variance of parameter 1, $cov(1,2)$ is the covariance between parameter 1 and parameter 2, and so on. $V(b')$ matrix must be always symmetric such that $cov(1,2)$ must be the same than $cov(2,1)$. Matrix size will depend on the total quantity of parameters.

Correlation coefficients between two parameters can be expressed in terms of their covariance and standard deviations (squared root of their variance) resulting of the $V(b')$ matrix, as shown in Equation (60).

$$cor(i,j) = \frac{cov(i,j)}{var(i)^{1/2}\ var(j)^{1/2}} \tag{60}$$

Correlation coefficients range from -1.0 to 1.0. Values close to these thresholds indicate that parameters should be estimated considering more observations than the considered. These correlation limits also indicate that parameters are highly correlated and should not be optimized simultaneously. $cor(i,j) < 0.90$ may indicate that does not exist a significant correlation between the evaluated parameters.

Both sensitivities analyses and optimization procedures will be carried out considering undrained triaxial compression and reduced triaxial extension laboratory tests, whose results are the aforementioned “observations”. For both sensitivities and correlation analyses, forward difference approximation method was considered [Equation (61)].

$$\frac{\delta y_i'}{\delta b_j} = \frac{y_i'(b_j + \Delta b_j) - y_i'(b_j)}{(b_j + \Delta b_j) - (b_j)} \tag{61}$$

In this work the inverse analysis for parameter optimization was conducted utilizing Python version 3.10.4. Python counts with optimization modules with several functions which can be implemented to minimize or maximize objective functions. In this work, the selected solver was nonlinear least-squares equations. This tool is useful for solving nonlinear least-squares curve fitting problems taking the following form:

$$\min_x \ || f(x) ||_2^2 = \min_x (f_1(x)^2 + f_2(x)^2 + \dots f_n(x)^2) \tag{62}$$

considering optional upper and lower bounds (function limits, in this works related to the parameters variation ranges) of the function x. This nonlinear solver requires the user to specify the specific function to be optimized. One of the main advantages of using Python is that it can be integrated directly with Plaxis software, so the code will automatically bring the output results. An example of the employed code structure is presented in Appendix A. The code “Opytimization” was developed by Alan Jared Aparicio (2022).

Python solver tool also asks the user to specify an algorithm or method. In this work, the Levenberg-Marquardt Method (Moré, 1978) was employed. A general Levenberg-Marquardt Equation can be written as:

$$\underset{x \in \Re^n}{min} \int_{t_1}^{t_2} (y(x,t) - \varphi(t))^2 dt \tag{63}$$

where x is the objective vector, t_1 and t_2 are scalars bounds, and $y(x,t)$ and $\varphi(t)$ are scalar functions. Details of this method are presented by Moré (1978). In order to solve the nonlinear system, an initial vector or matrix x_0 is needed, which corresponds in this case to the initial parameter value.

The number of total iterations depend mainly on the defined stopping criteria, which can be understood as thresholds that stop the process if crossed. The stop criteria in the Python code were *ftol, xtol,* g*tol, diff_step,* and *max_nfev.* The first tolerance criterion refers to the tolerance for termination by change of the function cost, the second one to the termination by the change of the independent variables, the third one to the gradient, *diff_step* determines the relative step size for the change of each iteration, and *max_nfev* refers to the maximum number of evaluations.

Since the relative step size is a constant value within the iterative process, a scaling function was included in order to convert the parameters to similar magnitudes, as recommended by Hill (2000):

$${X_0}^{scaled} = \frac{X_0 - X_{min}}{X_{max} - X_{min}} \tag{64}$$

where ${X_0}^{scaled}$ corresponds to the scaled parameter, X_0 is the parameter to be scaled (initial real value), and X_{max} and X_{min} corresponds to the maximum and minimum expected values of the parameter (*i.e.,* the thresholds). It must be clarified that these limits do not constrain the result of the optimization process, X_0 can take values out of the range of X_{max} and X_{min}.

The main output arguments of the adopted optimizing solver are the solution vector, x, which contains resulting optimization parameters, the squared norm of the residual, returned as a nonnegative real, residual vector of the function corresponding to the difference between the observed and computed responses, the cost at the solution, the optimality, status, and termination message. The selected criterion to quantify the accuracy of each iteration was the residual vector, which was computed as the root mean squared error:

$$Residual = \sqrt{\frac{1}{n}\sum_{i=1}^{n}(\hat{y}_i - y_i)^2} \tag{65}$$

where n corresponds to the number of observation points (*i.e.,* points on the soil response curve), $\hat{y}_i$ corresponds to the computed value, and y_i corresponds to the experimental value. One of the main limitations of the nonlinear functions is the non-uniqueness of the results. With pure numeric optimization techniques, one cannot be sure of finding the global minimum result even for functions that are not very complicated. Rarely optimization results will show the same results, that in this case would be the set of parameters. Nonlinear least-squares solver stops the iterating process when reaching the defined tolerance conditions, or even when reaching local minima, which means a function fit between the observed and calculated data, but specifically in one point. To overcome these issues, it is recommended to run optimization codes with different initial values and employ geotechnical judgment to define which results are more accurate for the objective function overall fit.

2.3 Advanced Testing in Residual Soils

Climate conditions at inter-tropical latitudes represent preferential weathering factors for the formation of residual soils. According to UN DESA (2019), approximately 40% of the earth's surface is constituted by the tropics, corresponding to the home of approximately 40% of the world's population nowadays. The previously described, information suggests that residual soils and their associated civil engineering projects development constitute an important part of the world's earth surface. Nevertheless, these soils are not that frequently studied and the available technical literature dealing with their fundamental mechanical behavior is reduced.

In contrast to sedimentary soils, geological history of residuals is not influenced by sedimentation or consolidation processes, but by weathering processes where the structure of the parental material is modified by chemical alteration. According to Wesley (1990), the diagenetic bonds and cementation developed during the geological history of the of the parent rock are destructured by weathering, resulting in several material property changes such as strength, stiffness, loss of mass, and increment in void ratio and porosity. Since it is known that weathering in residual soils is also affected by surface erosion, which indicates that stress history from weathering corresponds to unloading, it is not technically feasible to track the stress history of residual soils (Vaughan and Kwan 1984).

According to Vaughan and Kwan (1984), while under residual conditions the initial stress conditions of the parental rock tend to disappear due to weathering processes, the state of stress of residual soils is not affected by them and tends towards K_0-state (at-rest) stress state. Most of the research works carried out on residual soils (*e.g.*, Rahardjo et al. 2004; Chiu et al. 2014; Ng et al. 2019) have been conducted considering triaxial experimental laboratory tests under isotopically consolidated conditions, but there are not many available research works in the technical literature where the in-situ stress conditions were estimated under advanced triaxial testing reconsolidation conditions.

Few research works in which mechanical residual soil behavior have been studied by implementing advanced techniques can be found in the geotechnical literature. Wang and Ng. (2005) studied the effects of different stress paths on the small-strain stiffness behavior of a residual soil derived from weathered granitic rocks. Rocchi and Coop (2015) studied the effects of weathering on the physical and mechanical properties of granitic saprolite. Ng et al. (2004) evaluated the response of a loose decomposed granite under different stress ratios. Viana da Fonseca (1997) and Lim et al. (2019) are part of the few authors that have evaluated K_0-recompression paths on residual soils. They found an acceptable agreement between K_0 measured from laboratory procedures, Jaky (1994) empirical correlation, and pressuremeter (PMT) tests.

Galeano (2020) studied the mechanical behavior of a residual soil located in Colombia, implementing an advanced triaxial testing system that allowed the control of stresses,

strains, and volume change conditions to bring the soil specimens to their in-situ stress conditions. Galeano performed laboratory tests under different stress paths, drained and undrained conditions at small and large strain levels, one-dimensional compressibility, secant shear modulus evaluation, among others. Regarding the local state of art and practice, this is the only available experimental advanced evaluation of residual soil mechanical behavior that fulfilled the specific objectives of this research (see chapter 1.3). Galeano's work was selected for the evaluations presented in this research.

In this work, numerical simulations of the mechanical behavior of a residual igneous soil in the northwestern branch of the Colombian Andes (Cordillera Central) is presented. The description specified in the following chapters correspond to the location of the site of study, soil sampling procedures, geological and stratigraphic conditions, and the laboratory testing program conducted by Galeano (2020).

2.3.1 General description

The general scope of the Galeano's (2020) work was the analysis of the static and dynamic mechanical response of a residual soil located in the Colombian Andes, at both small and large strain levels. Rigidity of the materials were assessed mainly under the execution of field Multichannel Analysis of Surface Waves (MASW) tests and Cross-correlation techniques and Bender Element (BE) tests. The in-situ stress state and compressibility behavior were evaluated by means of a laboratory testing program composed of Incremenal Loading (IL), Constant Rate of Strain (CRS), and pseudo K_0-triaxial tests, as well as field tests, including Pressuremeter (PMT) tests. The stiffness degradation and the kinematic yielding were assessed mainly based on the results of drained and undrained triaxial laboratory tests (directional stress probes) performed on high-quality samples. A more precise description is presented in Sections from 2.3.2 to 2.3.5.

Some limitations mentioned by Galeano (2020) relate to the evaluation of the stiffness anisotropy of residual soils and the relationship between the void ratio, mean normal effective stress, and maximum shear stress for different degrees of cementation.

The location of the study site is shown in **Figure 2-17**. The investigation site is located at the northern end of the Central Cordillera in the Colombian Andes, specifically in the south of Antioquia (Aburrá Valley), Caldas city.

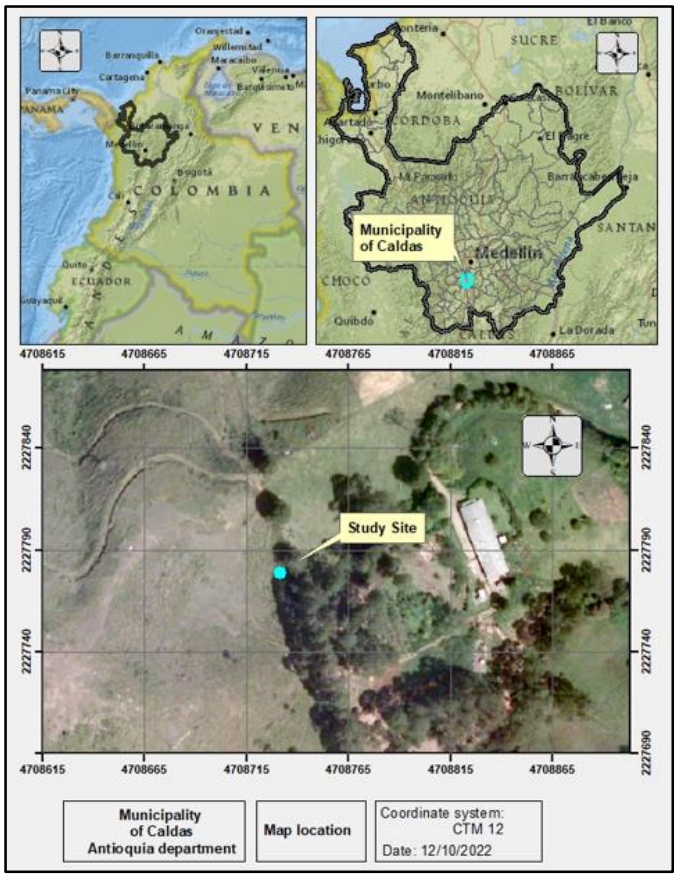

Figure 2-17: Investigation site location, northwestern branch of the Colombian Andes in South America. (Source: Google Earth 2022).

2.3.2 Field testing program

The field-testing program consisted mainly of geophysical Multichannel Analysis of Surface Waves (MASW), DownHole, Pressuremeter, and Standard Penetration (SPT) tests. Results of the field tests are summarized in Section 2.3.5. Further details of the involved procedures during field testing are presented by Galeano (2020).

2.3.3 Soil Sampling

Block samples from an excavated test pit in Caldas, Antioquia, were manually extracted at depths of 3.5 m, 5.5 m, 7.5 m, and 9.5 m measured from the ground surface. After extraction, the soil samples of residual soil were covered with paraffin wax and plastic wrap to minimize loss of moisture. Soil specimens were trimmed in the laboratory from the block samples to be later tested. The herein evaluated soil specimens correspond to the block sample retrieved at a depth of 5.5 m.

Figure 2-18: Test pit excavation. [From: Galeano (2020)].

The specific description of the sampling processes and specimen preparation are presented in detail by Galeano (2020) including all the followed standards.

2.3.4 Laboratory testing program

The laboratory experimental program conducted by Galeano (2020) in the University of Central Florida, included soil specimens tested under one-dimensional and triaxial conditions, *i.e.,* incremental loading (*IL*) and constant rate of strain (*CRS*) oedometer tests and pseudo K_0-TX tests, respectively, for the evaluation of soil compressibility.

IL tests were conducted under method B of ASTM D2435 on a fixed ring oedometer cell with double drainage with digital axial strain reading, including one unload-reload cycle. Soil specimens for these tests were trimmed to a diameter of approximately 50.8 mm and initial height of 19.1 mm. A constant Rate of Strain device with cell and a digital pressure/volume controller was employed to conduct CRS tests. Soil specimens trimmed to an average

diameter of 50 mm and 22 mm in height were used. Two cycles of unloading-reloading were considered for CRS tests. An electromechanical dynamic triaxial testing system was implemented to conduct pseudo K_0-TX tests. Internal instrumentation was installed on soil specimens, which included one set of vertical Bender Elements (BE), a submersible load cell, and three Hall Effect (HE) transducers. Specimens for pseudo K_0-TX tests were trimmed to an average diameter of 70 mm and initial height of 150 mm. Further details regarding laboratory test conditions and procedures are presented by Galeano (2020).

For the evaluation of the yielding and stiffness degradation, Galeano conducted triaxial K_0-consolidated laboratory tests following different stress paths. Firstly, soil specimens were brought to in-situ conditions under K_0 conditions (*i.e.,* zero lateral strain) to be later subjected to the following stress paths: triaxial compression (TXC), reduced triaxial extension (RTXE), constant mean stress (CMS), constant mean stress extension (CMNE), constant q load (CQL) and constant q unload. **Figure 2-19** illustrates the directional stress probes under triaxial conditions. Soil specimens following TXC and RTXE paths were sheared also under undrained conditions.

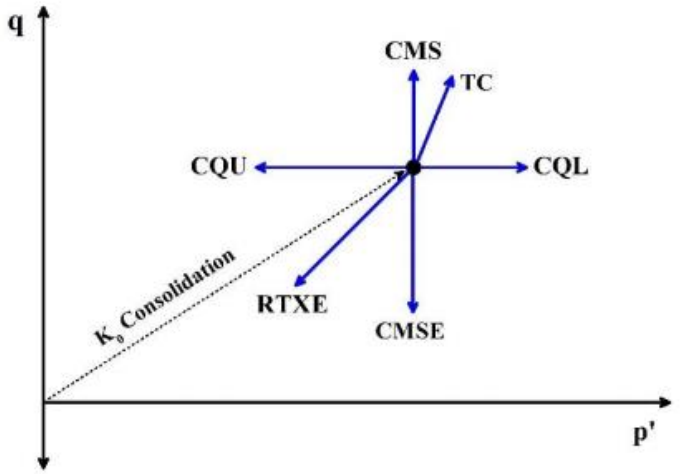

Figure 2-19: Graphical representation of the stress paths followed during reconsolidation and shearing stages in the experimental program conducted by Galeano, (2020).

For the execution of the triaxial laboratory tests, cylindrical specimens were hand-trimmed to approximately the average dimensions of 70 mm in diameter and 150 mm in length. An advanced electromechanical dynamic triaxial testing system was employed to conduct the

triaxial stress probes, which is capable of inducing axial forces and displacements, and is equipped with a balanced ram that also eliminates the disturbance to constant cell pressure conditions. Triaxial device counts also with digital volume controllers, pore pressure transducers, internal instrumentation (load cell and HE transducers) to measure small strains (<0.1%), among others. One set of vertical Bender Elements was used to measure propagation velocities and estimate soil stiffness at very small strain levels (<0.001%) during K_0-reconsolidation. Further details of laboratory equipment and procedures are presented by Galeano (2020).

2.3.5 Geology and stratigraphy of the investigation site

Figure 2-20 illustrates the subsoil conditions of the investigation site that were determined from laboratory and field tests with respect to depth. Water table level was not found during the exploration program. **Table 2-5** summarizes the index and compressibility properties obtained for all the soil specimens of the block samples recovered at depth of 5,5 m. A total of 12 specimens were evaluated, 6 corresponding to incremental loading and CRS tests, and 6 corresponding to triaxial probes.

Table 2-5: Summary of index and compressibility properties, taken from (Galeano, 2020)

Properties	Investigation site
Liquid limit [%]	77.9
Plastic index [%]	33.4
Specific gravity [-]	2.62 ~ 2.65 (2.63, 0.01)
Vertical effective stress [kPa]	110
Apparent overconsolidation ratio [-]	3.1 ~ 4.9 (4.2, 0.5)
Compression index [-]	0.327 ~ 0.498 (0.431, 0.070)
Recompression index [-]	0.044 ~ 0.059 (0.053, 0.005)

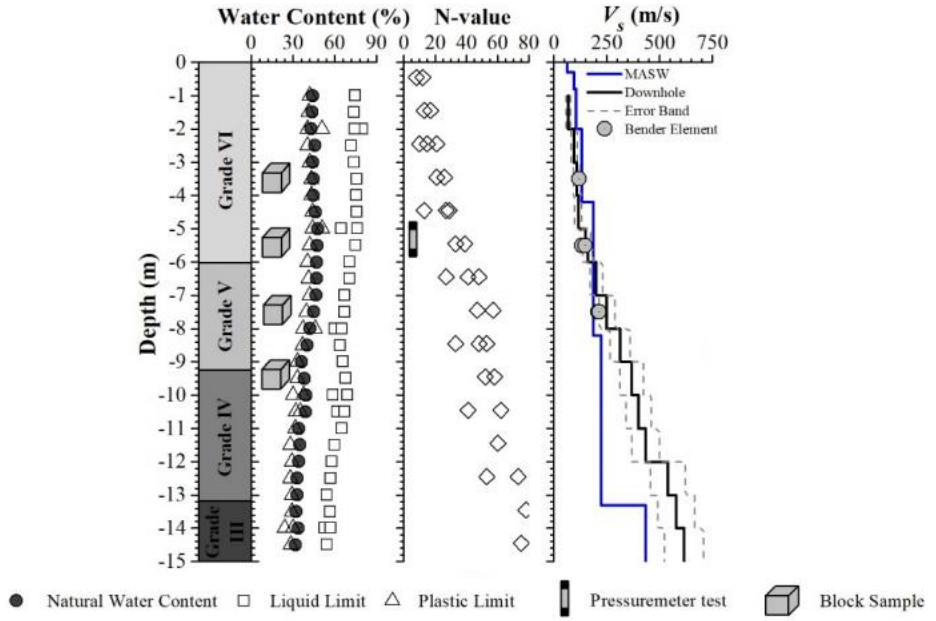

Figure 2-20: Subsoil conditions of the investigation site determined from field and laboratory tests. Taken from (Galeano, 2020).

As it can be observed in **Figure 2-20**, standard penetration test blow counts corrected to 60% energy efficiency (N60) increases with depth, varying from 5 close to surface to 70 reaching the 15.0 m below the ground surface. All tested samples show that the material corresponds to a semi-solid state in which the natural water content is between plastic and liquid limits. Both natural water contents and Atterberg's limits decrease slightly with depth. According to the Unified Soil Classification System (ASTM D 2487-11), the tested materials are classified as high plasticity silts (MH). Further physical soil properties and details are presented by Galeano (2020). Shear wave velocities (Vs) measured by means of field procedures increases with depth, while results from Bender Element tests do not show a similar trend.

The igneous basement that composes the site in study corresponds to volcanic rocks of the Quebradagrande Complex, which exhibits green rocks due to the chloritization of basalt rocks. According to AMVA (2006), Quebradagrande Complex rocks are composed in terms of mineralogy of highly altered plagioclase and augite as predominant mafic mineral. These rocks textures are described as porphyric and felsic. The soil of the study site corresponds to a residual profile formed by weathering of the igneous basement. According to Dearman (1991) classification criterion, Galeano (2020) stablished that the retrieved soil samples

correspond to V and VI lithological units, describing advanced weathering processes (see **Figure 2-20**), on the upper unit VI soil horizon. The microstructural characteristics of the residual soil and its mineralogical composition were evaluated using X-ray diffraction (XRD) and scanning electron microscopy (SEM) techniques. The XRD test results showed diffraction peaks associated with a predominance of kaolinite, silicon dioxide, pyroxene, and magnetite. Kaolinite and silicon dioxide minerals correspond to an advanced weathering process of the basaltic volcanic rocks. SEM results revealed a porous structure and particle aggregations formed by secondary minerals such as kaolinite and magnetite.

Samples recovered from unit V permitted the identification of planes of discontinuity and structures inherited from parent rock. Recall that all the tests results evaluated in this research correspond to the VI horizon samples. Further geology and mineralogy details are presented by Galeano (2020).

The assessment of sample quality and compressibility parameters are summarized in **Table 2-6**. Loading strain rate effects were not identified in the test results. This finding suggest that conventional IL oedometer tests (typically completed in approximately one week) may provide similar compressibility parameters respect to CRS tests (typically completed in less than 8 hours). Galeano (2020) suggests to investigate further in order to extrapolate this finding to other residual soils.

Table 2-6: Summary of compressibility parameters and sample quality assessment, taken from (Galeano, 2020)

Specimen ID	C_r	C_s	$\sigma'_y{}^a$ $[kPa]$	R_{u-max} [%]	AOCR[b]	Sample quality assessment	
						ε_{v0} to $\sigma'_{v0}{}^c$	$\frac{\Delta e}{e_0}$ to $\sigma'_{v0}{}^d$
S1-IL	0.052	0.400	500	-	4.54	2.65 (C)	0.042 (2)
S1-CRS-1	0.045	0.327	500	2	4.54	2.06 (C)	0.037 (2)
S1-CRS-5	0.056	0.481	660	3	6.00	1.50 (B)	0.026 (2)
S1-CRS-10	0.044	0.488	600	1	5.45	2.27 (C)	0.041 (2)
S1-CRS-20	0.059	0.460	660	8	6.00	2.47 (C)	0.060 (3)
S1-CRS-40	0.055	0.460	660	11	6.00	0.87 (A)	0.017 (1)

Specimen ID	C_r	C_s	$\sigma'_y{}^a$ $[kPa]$	R_{u-max} [%]	AOCR[b]	Sample quality assessment	
						ε_{v0} *to* $\sigma'_{v0}{}^c$	$\frac{\Delta e}{e_0}$ *to* $\sigma'_{v0}{}^d$
S1-UTXC	–	–	–	–	–	1.35 (B)	0.019 (1)
S1-URTXE	–	–	–	–	–	1.58 (B)	0.006 (1)
S1-CMNS	–	–	–	–	–	1.62 (B)	0.010 (1)
S1-CMNU	–	–	–	–	–	1.53 (B)	0.032 (2)
S1-CQL	–	–	–	–	–	1.75 (B)	0.026 (1)
S1-CQU	–	–	–	–	–	1.12 (B)	0.018 (1)

Note: Rating categories are shown in parentheses. For Andresen and Kolstad (1979): A, very good to excellent; B, good; C, fair; D, poor; E, very poor. For Lunne et al. (2006): 1, very good to excellent; 2, good to fair; 3, poor; 4, very poor. For Ferreira et al (2011): A, excellent; B, very good; C, good; D, fair; E, poor. e, void ratio; e_0, initial void ratio taken as the on table void ratio; ε_{v0}, vertical strain to reconsolidate to σ_{v0}.

[a] Based on the energy approach by Becker et al. (1987).
[b] Apparent OCR.
[c] Based on Andresen and Kolstad (1979)
[d] Based on Lunne et al. (2006)

The evolution of coefficient of earth pressure at rest during K0-reconsolidation shown in **Figure 2-21** suggests that there is a reasonable agreement between K0 values calculated based on the Jaky (1944) proposal and those obtained from PMT and pseudo K0-TX tests.

Despite the common residual soils characteristics such as porous structure, high void radios, and unsaturated nature, the evaluated soil is not susceptible to collapse or expansion. This was demonstrated by Galeano (2020) in laboratory procedures were abrupt volume changes were not observed under different stress levels and saturated conditions.

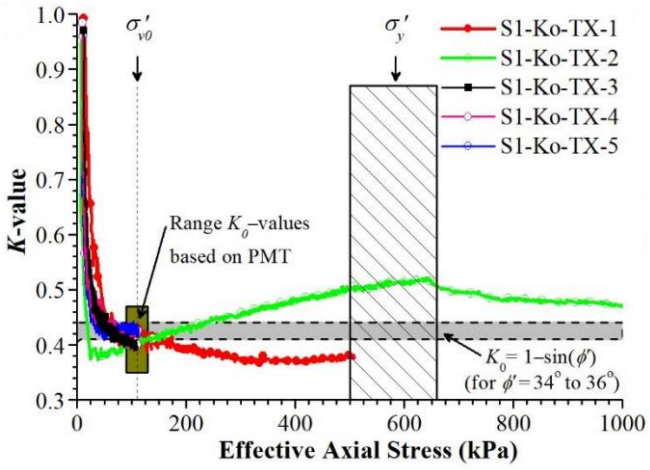

Figure 2-21: Evolution of the coefficient of earth pressure at rest during K_0 reconsolidation. Taken from (Galeano, 2020).

Figure 2-22 shows the studied residual soil behavior at small and large strain levels. The mechanical responses are presented in terms of shear stiffness degradation and deviator stress-shear strain responses for four (4) different stress paths. The stress path rotation angles, θ, were calculated as the change of direction between the K_0-reconsolidation path and the shearing stress path. These angles range between 15° and 170°. The influence of the stress path rotation angle is discussed in the following section.

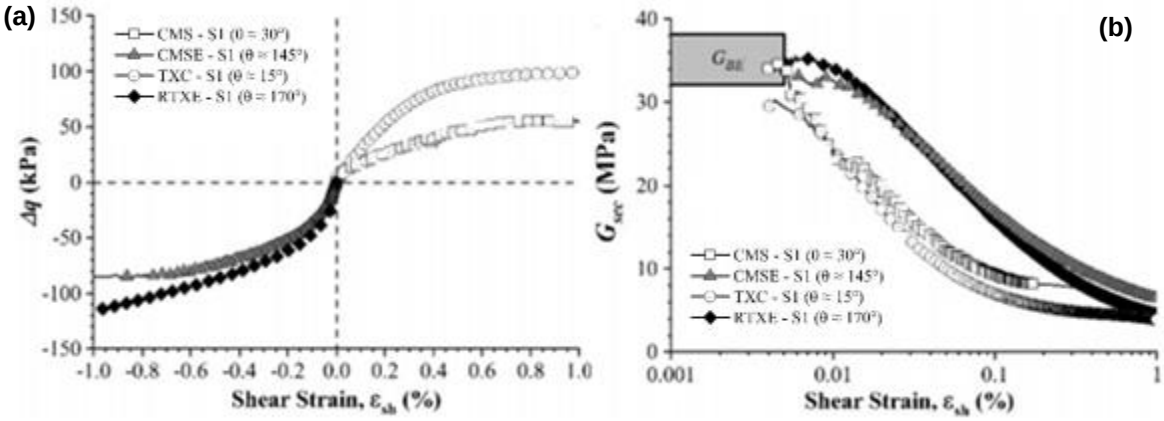

Figure 2-22: (a) Δq-$\Delta\varepsilon_{sh}$ responses; (b) Secant shear modulus degradation curves. Modified from (Galeano, 2020).

The mechanical response in terms of mean stress-volumetric strain and bulk stiffness degradation (*Ksec*) responses are presented in **Figure 2-23**, for both large and small

strains. Similar to shear stiffness, the secant bulk modulus exhibited stress path dependency.

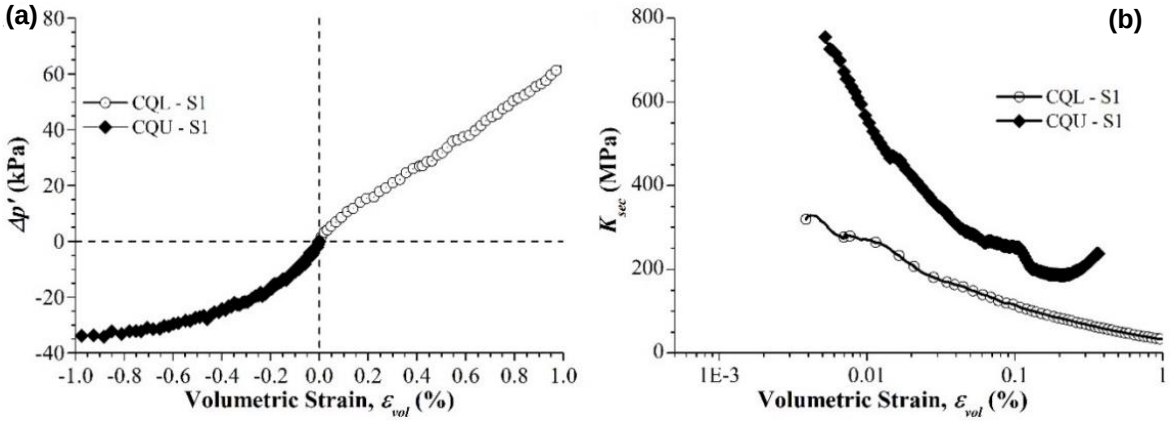

Figure 2-23: (a) $\Delta p'$-$\Delta \varepsilon_{vol}$ responses; (b) Secant Bulk modulus degradation curves. Taken from (Galeano, 2020).

The evolution of G_0 as a function of p' is presented in **Figure 2-24**. Galeano (2020) observed a linear trend between the small strain elastic shear modulus and mean normal effective stress, which differs with the normal behavior of sedimentary soils, where power functions better describe soil stiffness response in this space of analysis.

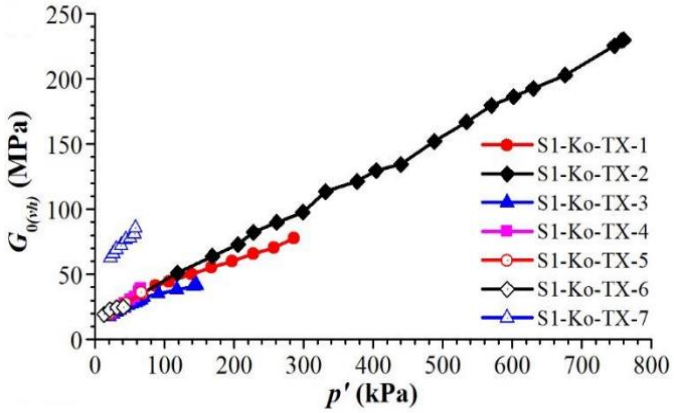

Figure 2-24: Small strain elastic shear modulus response during pseudo K_0-TX reconsolidation. Taken from (Galeano, 2020).

2.4 Stress path rotation angle

"Soil recent stress history" was a term adopted by Atkinson et al. (1990) to describe the current stress path direction with respect to the previous stress path, θ. It was observed

that stiffer responses were obtained when θ approaches 180°. Other authors (Jardine (1992); Smith et al. (1992); Callisto and Rampello (2002); among others) also found that pre-shearing paths influence soil stiffness in compression and extension triaxial tests under drained and undrained conditions.

Finno and Kim (2012) investigated the recent stress history effects (stress path rotation angle) on the small strain responses and secant shear modulus degradation of the Chicago glacial clays. The adopted pre-shearing paths are illustrated in **Figure 2-25**. Soil specimens were sheared under undrained conditions following extension and compression stress paths in a triaxial device with on-specimen instrumentation, subminiature LVDTs and bender elements. The soil specimens selected to evaluate recent stress history were taken to the same stress state prior to shearing, but with a different pre-shearing path.

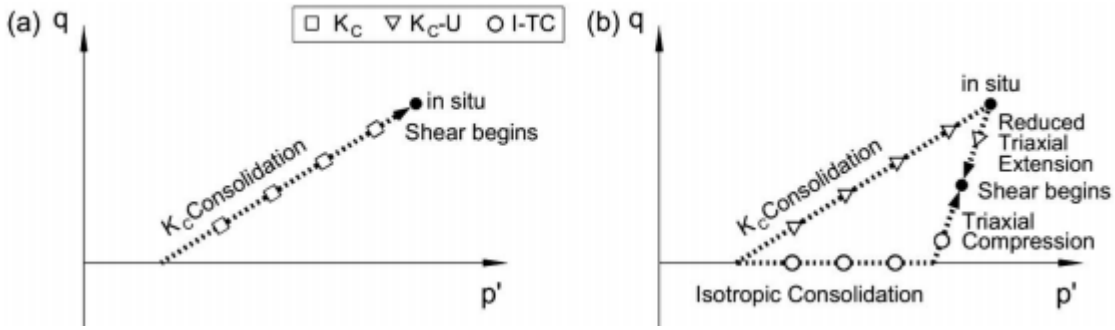

Figure 2-25: Pre-shear paths: (a) recompression to in situ stresses; (b) evaluation of recent stress history, taken from (Finno and Kim, 2012).

(θ) is used as the index to illustrate recent stress history effects. The rotation angle was calculated by Finno and Kim (2012) as the angle change from the previous stress path (0°) to a complete stress reversal (180°) for different stress paths. An example of the stress path rotation angle is shown in **Figure 2-26**.

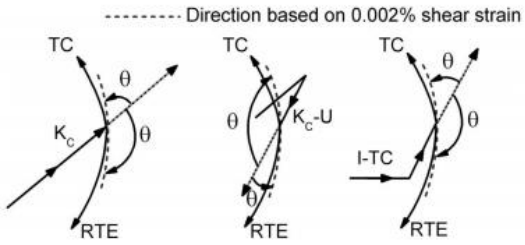

Figure 2-26: Illustration of the rotation angle, taken from (Finno and Kim, 2012).

(Finno and Kim, 2012) observed that the stress path rotation angle has an influence on soil stiffness. This effect was measured under different conditions: different pre-shearing path with same shearing path, and same pre-shearing path with different shearing path. For the cases when the rotation angle was close to 180°, the secant shear modulus degraded from the value evaluated from the bender element results, which did not occur for all other stress paths with different *θ,* as shown in **Figure 2-27**.

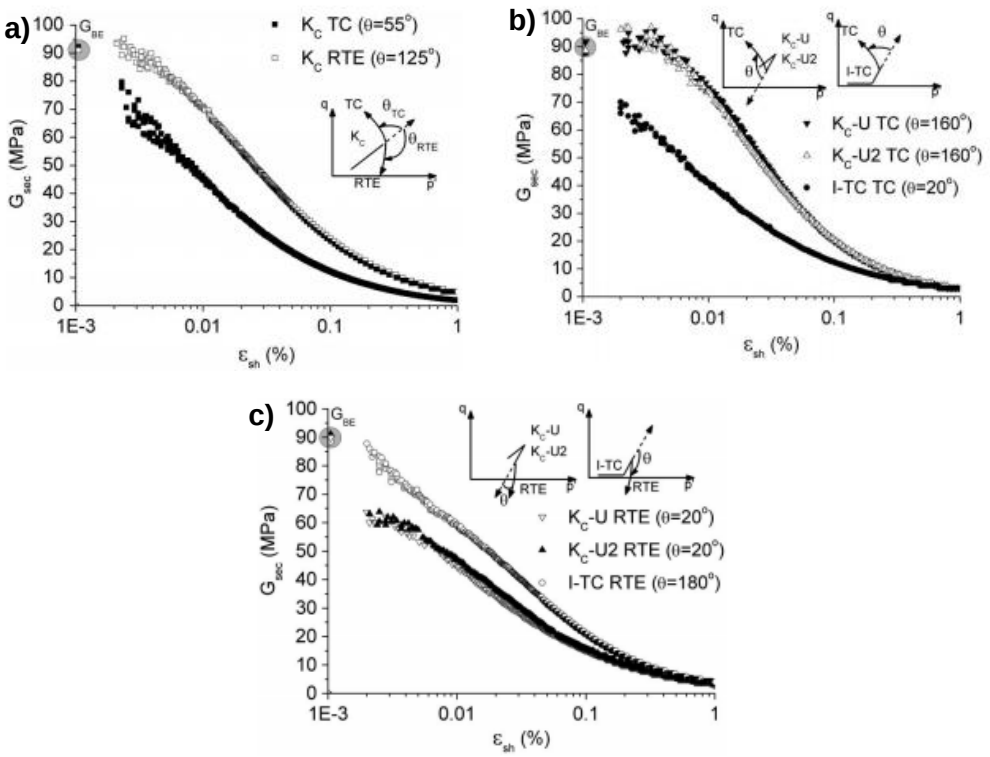

Figure 2-27: Secant shear modulus degradation curves. a) K_0 TXC and K_0 RTE. b) TXC with the pre-shear stress path of K_0-U and I-TC. c) RTXE with Pre-shear stress path of K_0-U and I-TC. Taken from [Finno and Kim (2012)]

After evaluating stress probe triaxial tests following different stress paths, Finno and Cho (2011) stated a hypothesis in which the secant shear modulus degradation curves would always start from the dynamically measured values if the internal LVDTs had sufficient accuracy to measure under a smaller strain range. **Figure 2-28** illustrates the experimental results of Finno and Kim (2012) which support the mentioned hypothesis.

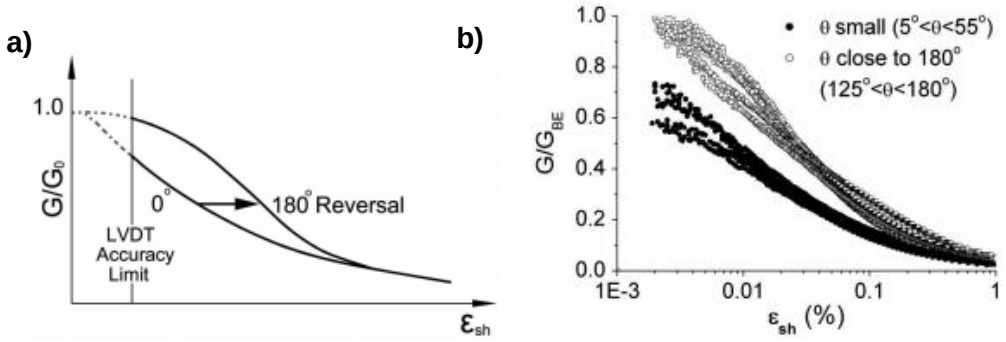

Figure 2-28: a) Hypothesized effects of recent stress history. b) Normalized stiffness degradation curves. Taken from (Finno and Kim (2012))

3. Modeling of Boundary Element Problems

The objectives of this research involve the numerical simulation by finite elements of boundary element problems. Therefore, the constitutive soil models to be evaluated are those already implemented in commercial software, specifically in Plaxis 2D® v21.01 by Bentley Systems©. This geotechnical software is widely used between practitioners. In this research, three different constitutive models were assessed: Hypoplastic model for clays, HSsmall, and Modified Cam Clay model. These models were presented and described in Section 2.1. Numerical model procedures, assumptions, and results are described in this chapter. The Modified Cam Clay model can be considered the simplest model mainly due to its limited capability to reproduce material-rate dependency and softening-hardening behavior. This constitutive model does not capture anisotropy and non-linear stiffness at small strain levels. However, it is easy to calibrate and used in local geotechnical modeling practice. It was selected and evaluated to demonstrate its applicability on the studied Igneous residual soil.

At large strains, the HSsmall model can reproduce the stress-dependency of soil, stress history effects, hardening, dilatancy, among others. Since one of the main variables analyzed in this work is the stiffness of the material and its degradation with respect to the stress path, the HSsmall model is suitable to capture the stiffness dependency related to the density.

The residual soil evaluated in this research showed apparent-preconsolidated behavior computed from compression laboratory tests [see Section 2.3]. The Hypoplastic clay model is capable to capture recent stress history effects (preconsolidation effects) with a single set of parameters, even for different OCR's (Hájek et al. 2009), small strain non-linearity and stiffness dependency on the stress path direction. Sarabia (2012) demonstrated that the Hypoplastic clay model can capture cross-anisotropy on the shear modulus. Several investigations have shown that this constitutive model can reproduce the mechanical

behavior of soils under drained and undrained conditions, at large and small strain levels, and under different shearing stress paths (*e.g.*, Arboleda-Monsalve et al. 2017; Sarabia, 2012; Kim, 2018). Due to the capabilities of this soil model, the Hypoplastic clay model was considered a priori as the most advanced of the three evaluated to reproduce the mechanical behavior of a soil, in general terms.

3.1 Numerical Simulation Conditions

For the evaluation of the constitutive soil models, two-dimensional (2D) finite element models were constructed under axisymmetric conditions using the software Plaxis 2D® v21.01. The numerical models simulated two stages performed in the triaxial tests: reconsolidation and shearing following compression and extension stress paths.

The Plaxis output data related to the stresses (q, p') and strains (axial, radial, volumetric, and shear strains) were compared to the laboratory tests results to evaluate the capability of the constitutive model and the defined set of parameters to represent the soil behavior under different conditions (stress paths). Due to the circular geometry of the soil specimens and the location of the loads acting on it (laboratory stresses), an analysis under axisymmetric conditions was employed.

Under this type of analysis, the stress state on any radial plane is the same, while the shear stresses on a circumferential plane (z) are zero. The radial deformation produces also circumferential deformation which are taken into account. In Plaxis software, this is denoted by the following equation:

$$\varepsilon_{zz} = \frac{1}{r} U_x \tag{66}$$

where U_x is the circumferential displacement and r is the radial initial length.

Equation (67) shows as an example of the stiffness matrix of an elastic linear material under axisymmetric conditions, which is modified in each constitutive soil model, maintaining the coordinate system.

$$\begin{bmatrix} \sigma'_{xx} \\ \sigma'_{yy} \\ \sigma'_{zz} \\ \sigma'_{xy} \end{bmatrix} = \frac{E}{(1-2\nu')(1+\nu')} \begin{bmatrix} 1-\nu' & \nu' & \nu' & 0 \\ \nu' & 1-\nu' & \nu' & 0 \\ \nu' & \nu' & 1-\nu' & 0 \\ 0 & 0 & 0 & 1-\nu' \end{bmatrix} \begin{bmatrix} \varepsilon_{xx} \\ \varepsilon_{yy} \\ \varepsilon_{zz} \\ \gamma_{xy} \end{bmatrix} \quad (67)$$

where E refers to the Young modulus, ν' refers to the Poisson coefficient, σ corresponds to the applied stresses under axisymmetric conditions in their respective directions, and ε and γ correspond respectively to the axial and shear strains under axisymmetric conditions. Directions *xx*, *yy* and *zz* indicate the principal planes, while *xy* subscript indicates shear stress and strain.

In **Figure 3-1**, the axisymmetric conditions of the numerical model are shown. In later sections, the boundary, geometry, meshing, and saturation conditions are explained in detail.

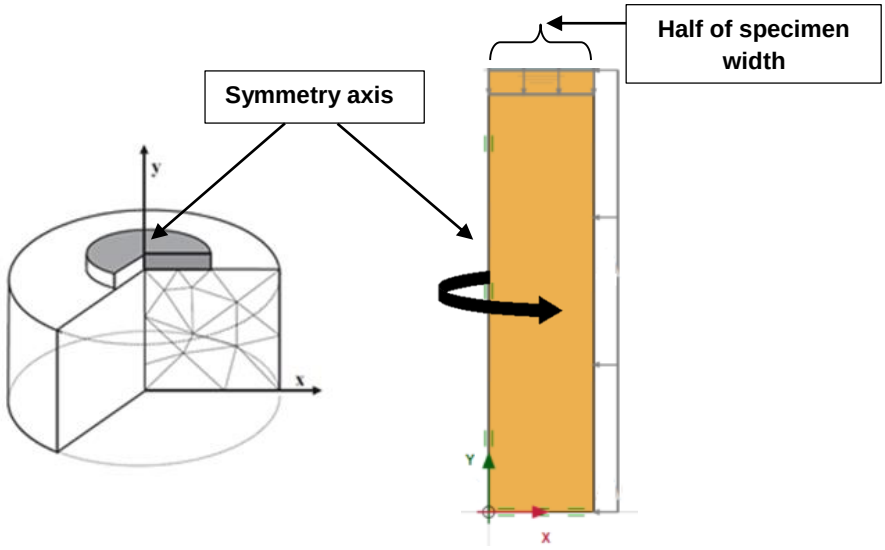

Figure 3-1: Axisymmetric conditions scheme, modified from (Brinkgreve et al. 2017).

In this work, the following notation is employed, unless another notation is specified (axisymmetric conditions):

$$p' = (\sigma'_a + 2\sigma'_r)/3 \quad (68)$$

$$q = \sigma'_a - \sigma'_r \quad (69)$$

$$\varepsilon_{vol} = \varepsilon_a + 2\varepsilon_r \tag{70}$$

$$\varepsilon_{sh} = (2/3)\,(\varepsilon_a - \varepsilon_r) \tag{71}$$

Where σ_a'' and σ_r' correspond respectively to the axial and radial effective stresses, and ε_a and ε_r correspond to the axial and radial strains, respectively.

3.1.1 Geometry, Mesh, Boundary, and Saturation Conditions

According to the soil specimen preparation performed in the experimental program, described in Section 2.3.4, the element dimensions in the numerical model were standardized for all the triaxial stress probes as 152 mm in height and 76 mm in radius. 19.1 mm in height and 25.4 mm in radius for IL tests, and for CRS tests, 22 mm in height and 25 mm in radius. Recall the numerical model represents axisymmetric conditions. The assumed element dimensions correspond to an average measurement of the soil specimens presented by Galeano (2020). The numerical models were carried out considering a non-weight material, so the results were not influenced by the size of the finite element.

In order to reproduce the stages performed in the triaxial tests, the left and bottom boundaries were normally fixed (recall the left boundary corresponds to the axisymmetric axis, which must always be laterally fixed and seepage-closed). Upper and right boundaries were not fixed to allow the soil element to displace in both directions. Stresses were applied directly to these boundaries. See Section 3.1.2 for further details and graphic representations. For the oedometer tests, the bottom, right, and left boundaries were normally fixed to simulate the lateral constrained conditions, which represent K_0 conditions. The only free boundary is the upper one. **Figure 3-2** shows the element boundaries of both oedometer and triaxial stress probe tests. Oedometer tests were numerically simulated with no stress path prior to the compression loading. Vertical loads were incrementally applied on top of the soil cluster, as shown in **Figure 3-2**.

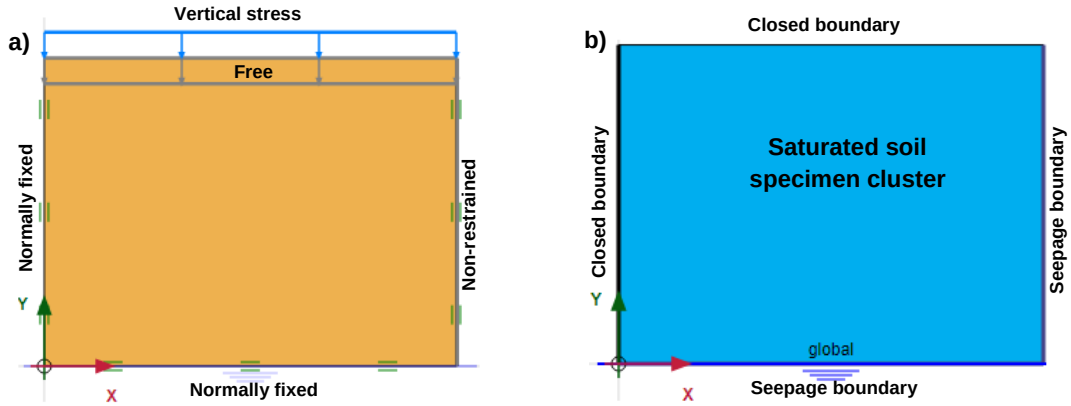

Figure 3-2: Numerical oedometer model. a) Loading and constraining conditions, b) Saturation and drainage conditions.

To simulate saturated conditions, the water table was defined at the bottom of the soil cluster, so that no external water column influences the numerical results as it occurs when the water table is set at the top of the soil cluster (*i.e.,* active water pressure). Regardless the position of the water table, the cluster can be set as saturated and then the model is able to compute excess pore pressures. In the experimental laboratory program, the specimens for IL tests were flooded according to the ASTM D2435, and CRS tests specimens were saturated by means of cell pressure, according to ASTM D4186. Further details are presented by Galeano (2020).

The mesh of the numerical model was defined as coarse, composed by 15-node triangular elements, as recommended by Brinkgreve et al. (2017). According to the Plaxis reference manual, the exact number of mesh elements depends on the shape of the geometry and optional local refinement settings. A mesh composed by 15-node elements give a more precise distribution of the nodes and more accurate results, but a 6-node mesh is less time-consuming and leads to fairly accurate stress and strain distributions results. 15-node triangle meshing has demonstrated accurate results regarding high quality stress distribution for difficult geotechnical problems such as incompressible soil numerical simulations, also it is particularly recommended for axisymmetric analysis (Brinkgreve et al. 2017). Thus, it was selected for the modeling processes.

Figure 3-3 illustrates the difference between the position of the nodes and stress points in soil elements composed by a 15-node triangle and a 6-node triangle.

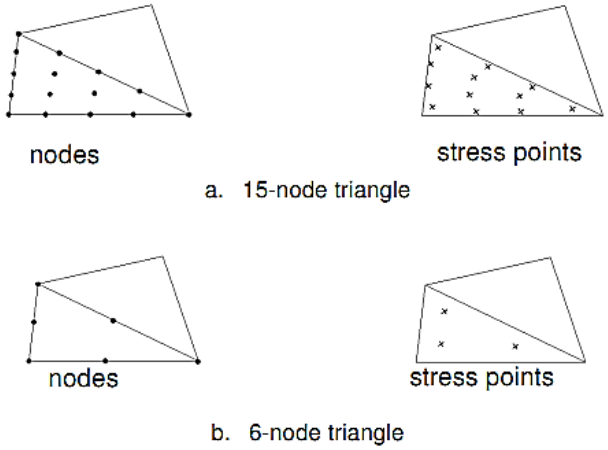

Figure 3-3: Position of the nodes and stress points in soil elements. Taken from Plaxis reference manual

Considering that the numerical models were integrated with other numerical tools such as Python and iterative processes were implemented in order to achieve parameter optimization, the defined mesh allowed to considerably save time. Expert meshing settings were implemented with a relative element size of 16.66 (maximum allowed), yielding two finite elements for the whole mesh.

3.1.2 Numerical Simulation of Triaxial Stress Probes

It is widely known that the soil experiences changes in its stress state from sampling to laboratory testing. Ladd and DeGroot (2003) describes the stress paths undergone by the soil during drilling, tube sampling, tube extraction, transportation and storage, sample extrusion, and specimen preparation, as illustrated in **Figure 3-4**. Despite these stress paths can be idealized and numerically modeled (*e.g.*, Arboleda-Monsalve et al. 2017), as shown in **Figure 3-5**, further data are required to adequately recreate the derived effects from sampling to laboratory testing on the mechanical soil behavior. **Figure 3-6** shows the two pre-shearing stress paths modeled in this research: saturation and reconsolidation in K_0-conditions.

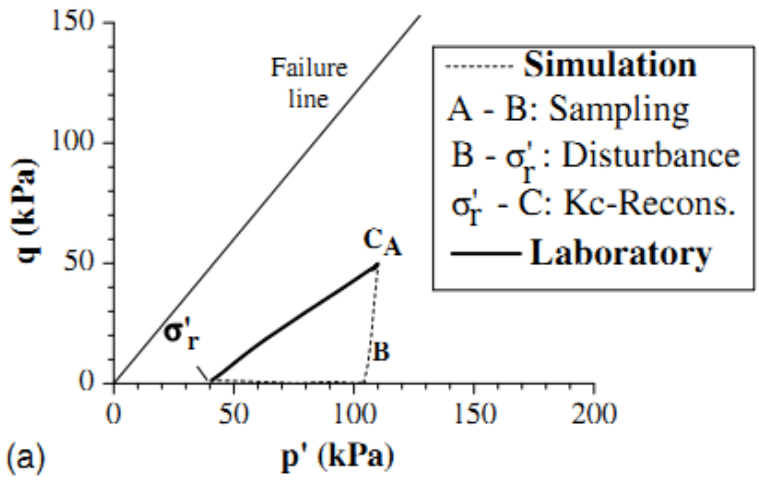

Figure 3-4: Preshearing stress paths followed in the Hypoplastic clay model, taken from (Arboleda-Monsalve et al. 2017)

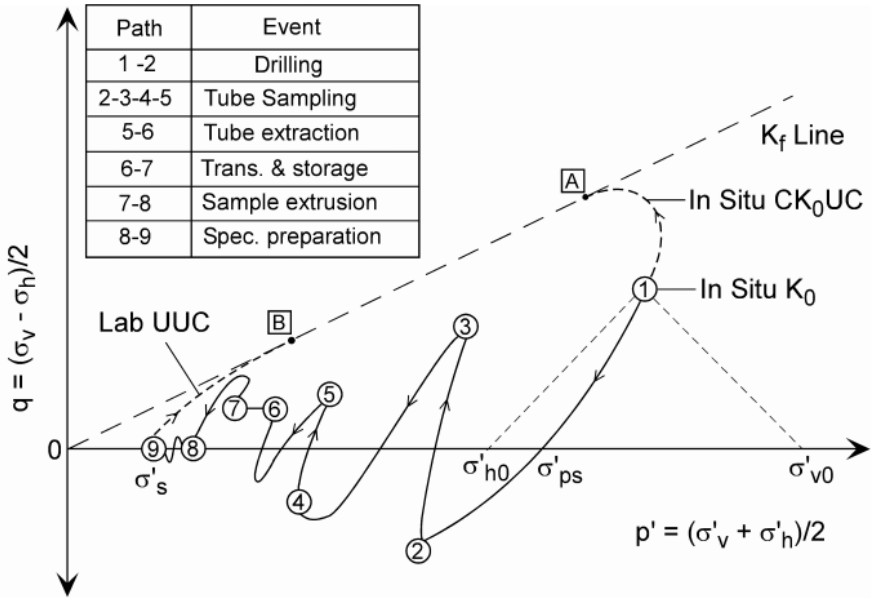

Figure 3-5: Hypothetical Stress Path During Tube Sampling and Specimen Preparation of Centerline Element of Low OCR Clay (after Ladd and Lambe 1963, Baligh et al. 1987), taken from [Ladd and DeGroot (2003)].

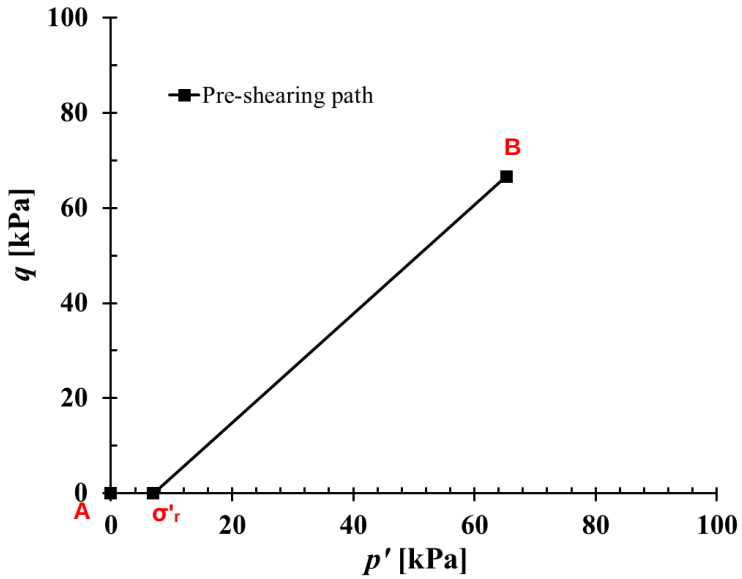

Figure 3-6: Pre-shearing stress paths followed for the numerical simulation of triaxial stress probes.

The path through points A-σ'$_r$ represents the isotropic loading from a stress-free state to the residual stress. Path through points σ'$_r$–B represents the K_0-reconsolidation stage to the in-situ effective vertical stress of the soil. **Figure 3-7** schematizes the shearing paths followed during the numerical simulations. Recall that the triaxial compression and reduced triaxial extension paths were conducted under undrained conditions both in laboratory and in the numerical models, while the others under drained conditions.

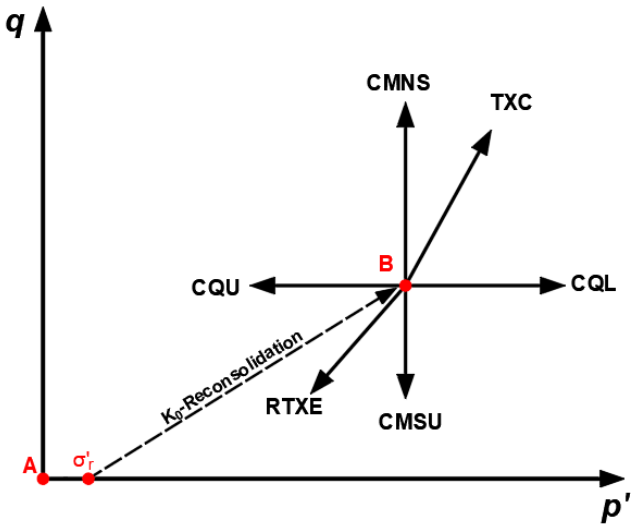

Figure 3-7: Shearing stress paths followed in the numerical triaxial tests simulations

The numerical models were developed to reproduce the laboratory sequence during triaxial stress probing and oedometer testing. For the triaxial stress probes, the following stages were performed:

1) **Initial stage (K_0):** In this stage, the distribution of initial internal stresses influenced mainly by cluster self-weight, water conditions, and geologic history from its formation are calculated, considering the ratio between the horizontal and vertical effective stresses. Assumed initial conditions do not consider the existence of the water table, according to the field exploration results reported by Galeano (2020). A K_0-value of 0.41 was defined as input data based on the oedometer tests, pressuremeter (PMT) tests, and empirical correlations reported by Galeano. The initial stage was conceived as isotropic stress-free state. See **Figure 3-8-b.**

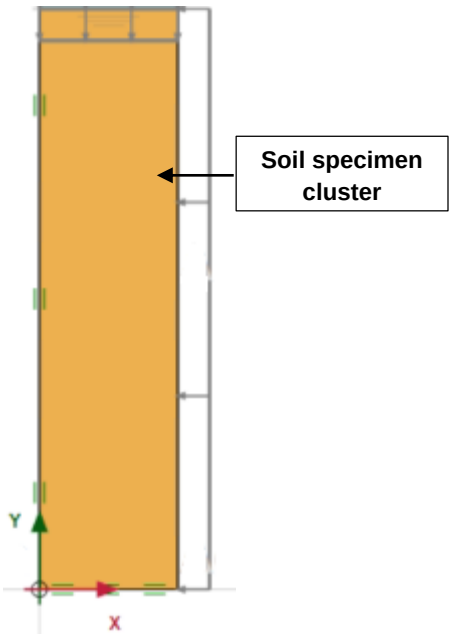

Figure 3-8: Initial conditions of the numerical model in Plaxis 2D.

2) **Saturation stage:** This stage basically represents loading under isotropic conditions to the residual stress. According to Galeano (2020) experimental program, the specimens were backpressure saturated under a constant stress equal to the residual effective stress, to prevent swelling and possible structural degradation. See **Figure 3-9**. During the laboratory experimental program, the residual stress was estimated by means of increments of cell pressure and measurements of the excess pore pressure in the soil specimen. The saturated

conditions were assured by verifying B−values larger than 0.95. This stage was conceived as a drained plastic stage.

3) **Reconsolidation stage:** In this stage, the soil element (cluster) is brought to its in-situ stress by applying a K_0 external load increment. For each different test simulation, the stresses were applied according to the reconsolidation stage of the laboratory procedures presented by Galeano (2020). For all soil specimens (tests for different shearing paths) the vertical effective stress was approximately 100 kPa.

   This stage was conceived as a plastic numerical stage with no excess water pore pressure, so that the next stage (shearing) starts from drained or undrained conditions. After this stage, the displacements and strains were set to zero. See **Figure 3-10**.

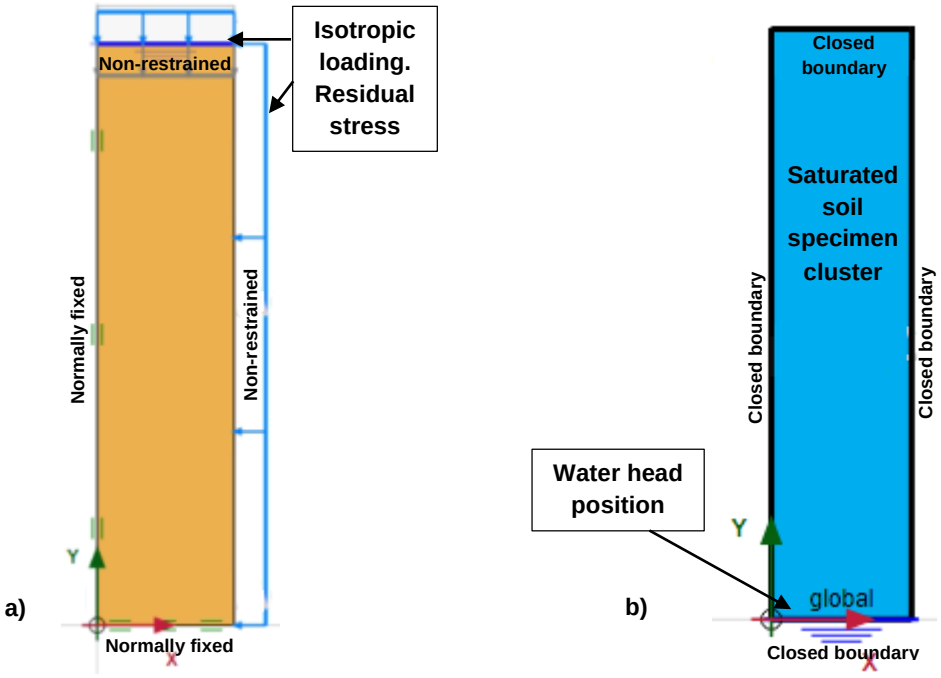

Figure 3-9: Saturation stage. a) Loading and constrained conditions, b) Saturation and drainage conditions, all boundaries closed to seepage.

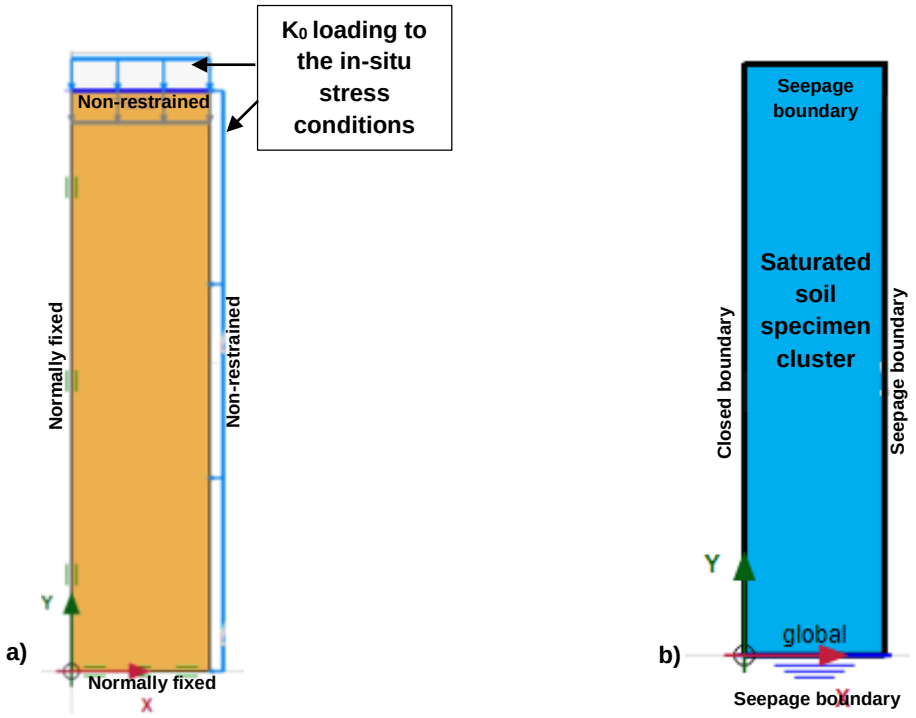

Figure 3-10: K_0 reconsolidation stage. a) Loading and constrained conditions, b) Saturation and drainage conditions, all boundaries opened to seepage.

4) **Shearing stage:** This numerical stage was carried on with external load increments, under stress-controlled conditions. For triaxial compression (TXC) and reduced triaxial extension (RTXE) stress paths, the numerical simulations were conducted under undrained conditions, whereas for constant mean normal stress (CMNS) and constant q load (CQL) stress paths, under drained conditions. The stress paths imposed in the numerical models adequately recreated those in the triaxial stress probe tests. See **Figure 3-11**. All shearing phases were conducted under plastic stages.

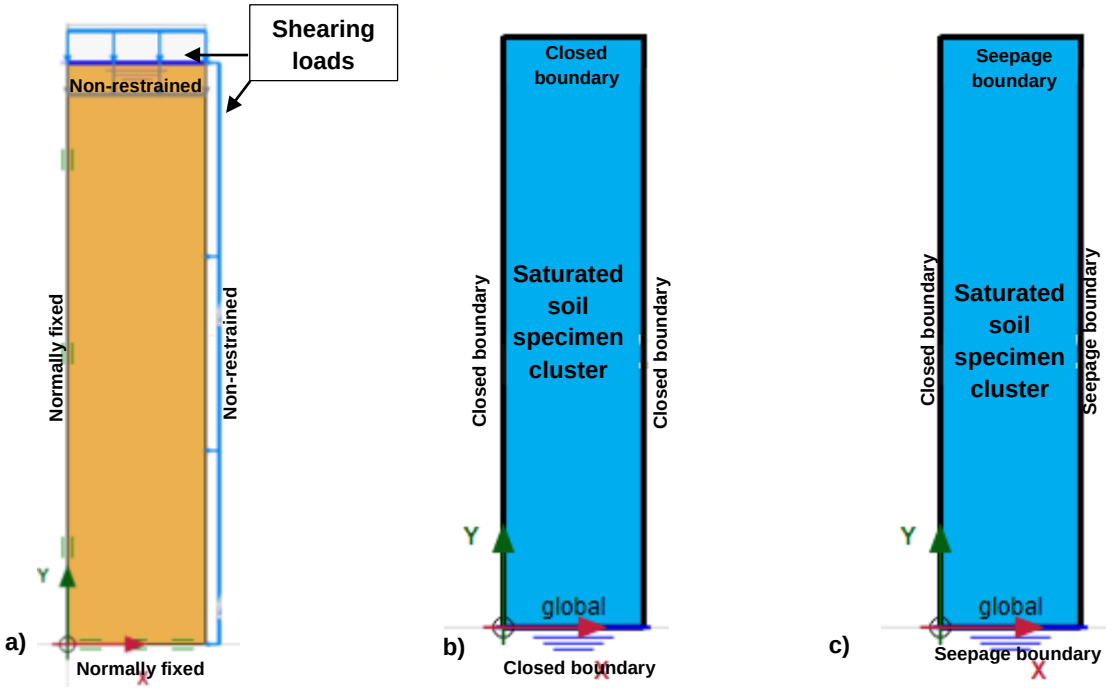

Figure 3-11: Shearing stage under stress-controlled conditions. a) Loading and constrained conditions, b) Saturation and drainage conditions for the TXC and RTXE paths, c) Saturation and drainage conditions for the tests sheared under other paths.

3.2 Parameters Identification

The evaluation of a constitutive model's capabilities must include the determination of all its constitutive parameters. This chapter describes the procedures followed to estimate the constitutive parameters of the Hypoplastic clay, HSsmall, and Modified Cam Clay soil models. Some parameters were directly obtained via the experimental results, while the remaining ones via inverse analysis (optimization techniques).

Some constitutive parameters which compose the assessed models have clear physical meaning, represent a specific characteristic of the soil, and their magnitude can be estimated from laboratory tests, implying that their effect on the soil stiffness, compressibility, strength, among others, can be isolated. On the other hand, the remaining parameters, as for many models, can be identified as fitting parameters or fudge factors which purpose is to match or fit the computed results to the experimental measured data. These parameters can be difficultly linked to soil behavior via laboratory tests. Therefore, their estimation is typically obtained using parametric analysis and/or optimization techniques. In order to obtain accurate results, the optimization processes must be

conducted over constitutive parameters which represent an important effect on the soil response (Calvello, 2002).

3.2.1 Modified Cam Clay model

The compressibility-related constitutive parameters were obtained from the IL and CRS oedometer tests conducted by Galeano (2020). The compression lines and the unloading-reloading cycles of these tests are presented in **Figure 3-12** and **Figure 3-13**, respectively.

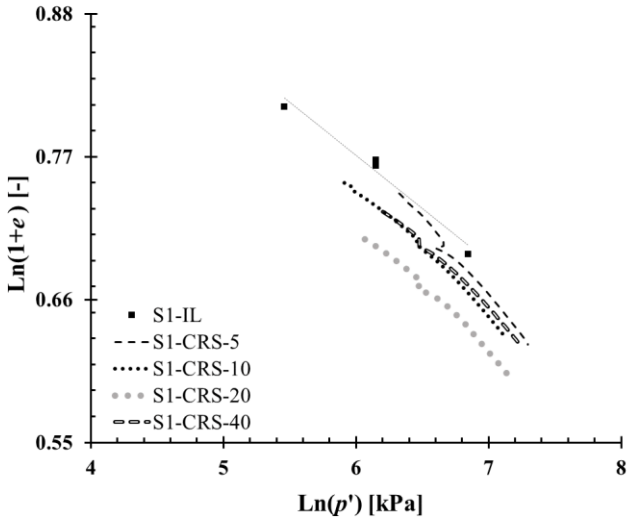

Figure 3-12: Compression range obtained from compressibility tests – Caldas residual soil.

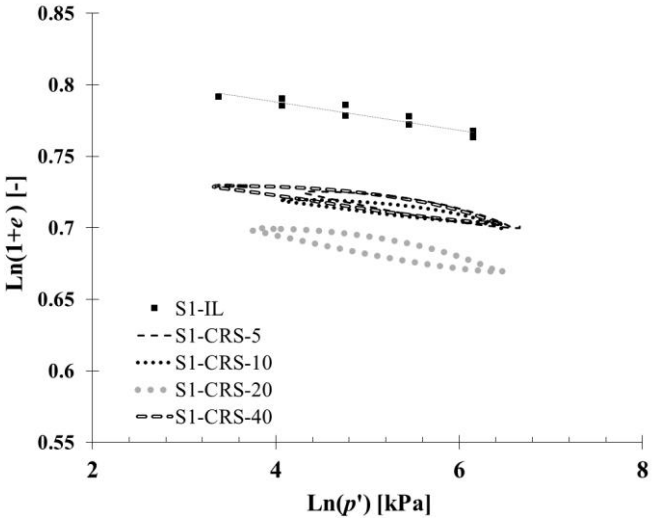

Figure 3-13: Unloading-reloading cycles obtained from compressibility tests – Caldas residual soil.

As it can be observed in **Figure 3-12** and **Figure 3-13**, the slope of the compression lines during primary loading are similar for all the performed tests. Also, for the unloading-

reloading lines. Based on these observations, the constitutive parameter λ ranges from 0.075 to 0.140 and the parameter k ranges from 0.0079 to 0.015.

For the definition of the critical state friction angle (φ'_c), the triaxial tests conducted by (Galeano, 2020) were considered, specifically three stress paths, constant mean normal stress (CMNS), triaxial compression (TXC), and constant *q*-unload (CQU), as shown in **Figure 3-14**.. The critical state line slope, *M*, is related to the critical state friction angle [Equation (72)]. The estimated critical state friction angle varies from 34° to 36°.

$$M = \left(\frac{q}{p}\right)_c = \frac{6 * sin(\varphi'_c)}{3 - sin(\varphi'_c)} \tag{72}$$

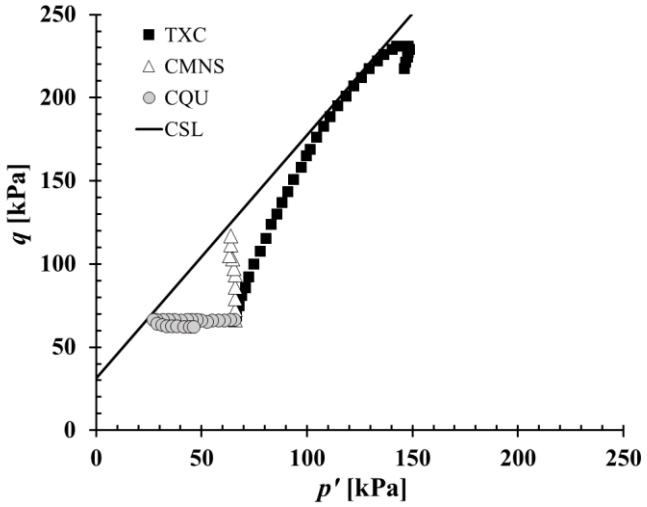

Figure 3-14: Critical state line – Caldas residual soil.

The Poisson's ratio, v_{ur}, was estimated by means of optimization techniques. For the constitutive parameter related to the void ratio, e_{init}, inverse analysis techniques were also applied since the numerical simulations showed that the mechanical behavior was not well represented by the average in-situ void ratio of the material.

3.2.2 HSsmall model

Tangent stiffness for primary oedometer loading was estimated from the compression tests performed by Galeano (2020). It must be noted that there exists a scatter related to the

initial void ratio of the soil specimens, which is reflected in the compression behavior (see Section 2.3.4). The evolution of the Oedometric Modulus (primary loading) with respect to the vertical stress is presented in **Figure 3-15**.

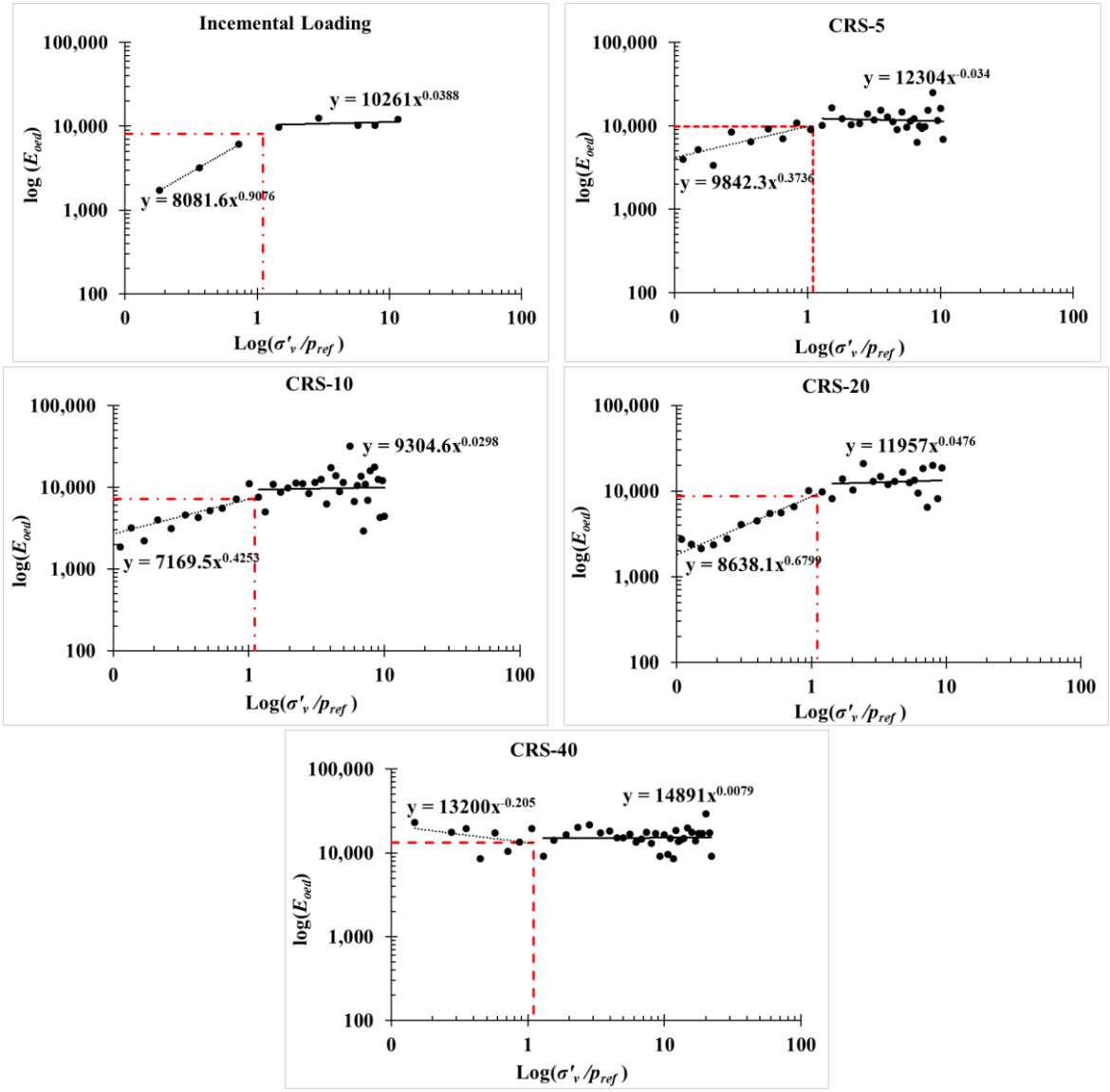

Figure 3-15: Oedometric modulus-vertical effective stress in logarithmic space.

The dashed black lines correspond to the overconsolidated state of the material, while the continuous ones correspond to the normally consolidated state. The red lines mark the change of the state which corresponds to the in-situ effective vertical stress. Note that the slope of the normally consolidated state is practically zero. According to the theory (see

Section 2.1.2), parameter m was assumed as zero since the studied residual soil shows an apparent overconsolidation ratio of 4, as indicated in Section 2.3.

Since the Galeano (2020) laboratory testing program does not count with at least three triaxial compression tests with different confining stress conditions, the parameter ${E_{50}}^{ref}$ was obtained from inverse analysis. The same applies for the ${E_{ur}}^{ref}$ parameter since there are not unload-reload cycles in the reference experimental campaign.

Peak friction angle φ' and cohesion intercept c' were obtained from the triaxial tests conducted by Galeano (2020), $\varphi' = 45°$ and $c' = 16\ kPa$, respectively. In order to obtain the peak strength parameters, an axis translation between *p'-q* space (MIT notation) and Mohr-Coulomb space was employed:

Dilatancy parameter ψ was obtained from expression shown in Equation (27), which also involves the critical state friction angle. Critical state-related constitutive parameters definition is presented in Sections 3.2.1 and 3.2.3. Initially, the obtained dilatancy parameter from the available experimental results was $\psi = 11°$, which was later adjusted by means of optimization techniques (inverse analysis).

The experimental results provided by Galeano (2020) showed dilatancy in the drained triaxial tests, specifically for the CMNS and CMNU stress paths. For CQU and CQL stress paths, dilatancy was not observed.

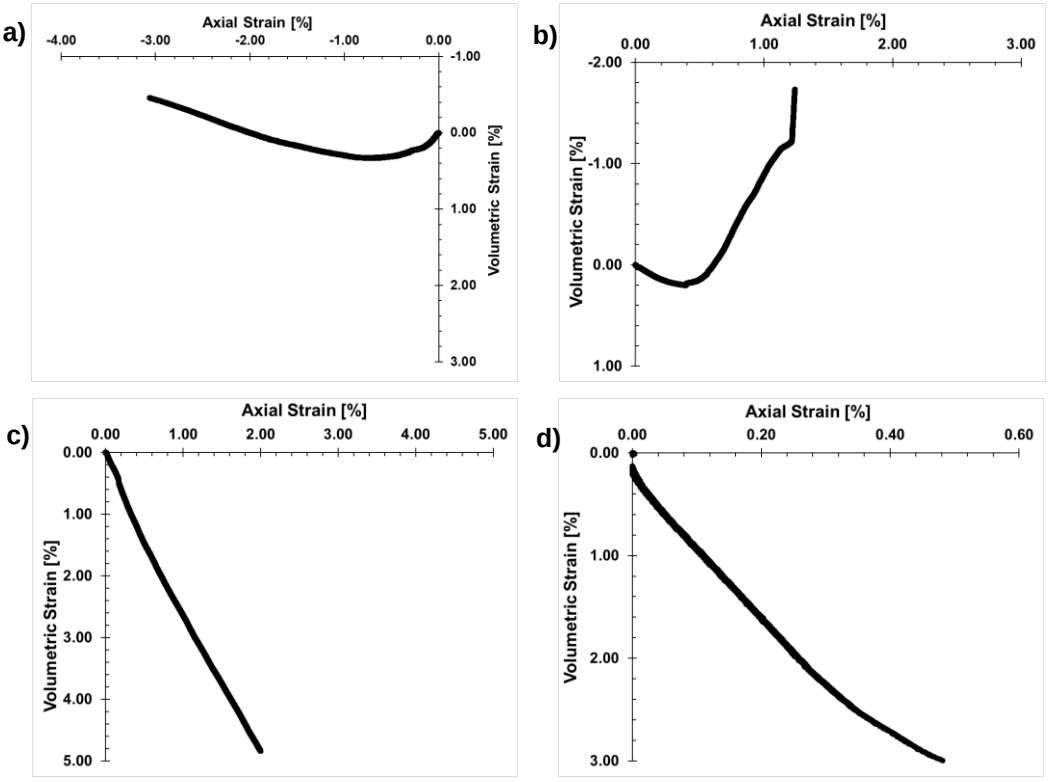

Figure 3-16: Dilatancy behavior evaluated from drained triaxial tests. a) CMNE, b) CMNS, c) CQL, and d) CQU stress paths. Taken from (Galeano, 2020)

The failure ratio parameter was initially set as a default $R_f = 1$, and it was later refined by means of inverse analysis. Poisson's ratio was set to the Plaxis software default $v_{ur} = 0.2$. Tensile strength and increase of cohesion with depth were not considered during the numerical simulations. The lateral earth pressure coefficient parameter was assumed to be ${K_0}^{NC} = 0.41$, which corresponds to an average value measured by Galeano (2020) and explained in Section 2.3.4. Parameter p^{ref} was defined as 100 kPa.

Regarding the small strain stiffness parameters, the initial or very small-strain shear modulus, G_0, was obtained as the average value between the maximum secant shear modulus obtained from the triaxial tests of the Galeano (2020) experimental campaign via HE transducers. The parameter $\gamma_{0.7}$ was obtained also as the average value of the shear strain corresponding to a 70% of each maximum stiffness.

3.2.3 Hypoplastic clay model

Regarding the results from oedometer tests (*i.e.,* IL and CRS tests), a plot with the corresponding data in the $ln(p')$-$ln(1+e)$ space is presented in **Figure 3-17**. Since the mean stress is not known from the evaluated laboratory results, the following expression recommended by Mašín (2015) was used:

$$p = \sigma_V \frac{1+2K_0}{3} \tag{73}$$

where σ_V is the applied vertical stress and K_0 (~0.41) is the ratio between the horizontal and the vertical effective stresses, which was measured by means of in-situ pressuremeter tests and K_0-reconsolidation tests in the compression range (Galeano 2020).

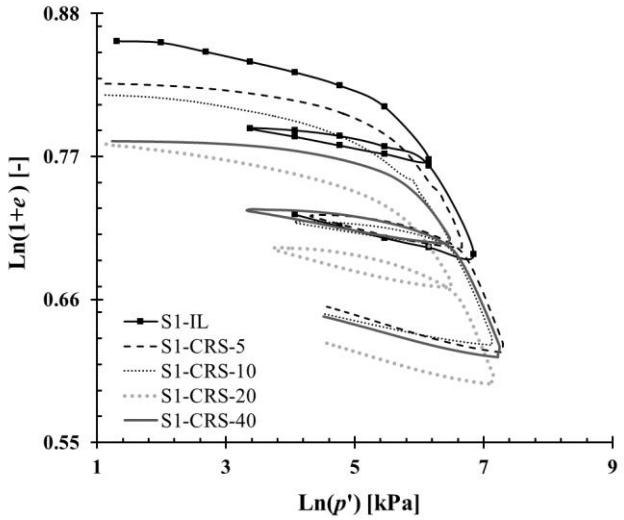

Figure 3-17: Incremental Loading (IL) and Constant Rate of Strain (CRS) oedometer tests in the $ln(1+e)$-$ln(p')$ space for Caldas soil.

In order to estimate the magnitudes of constitutive parameters N and λ^*, the virgin compression portions of each test result is presented in **Figure 3-18**, also in the $ln(1+e)$-$ln(p')$ space. Mašín (2015) suggests obtaining parameters λ^* and N from compression tests (oedometric or isotropic) conducted on reconstituted specimens in order to avoid the effects of soil structure. The reference experimental campaign (Galeano, 2020) did not consider tests on reconstituted specimens; thus, parameters were evaluated from

tests conducted on “undisturbed” specimens, taking into account the effects of soil structure.

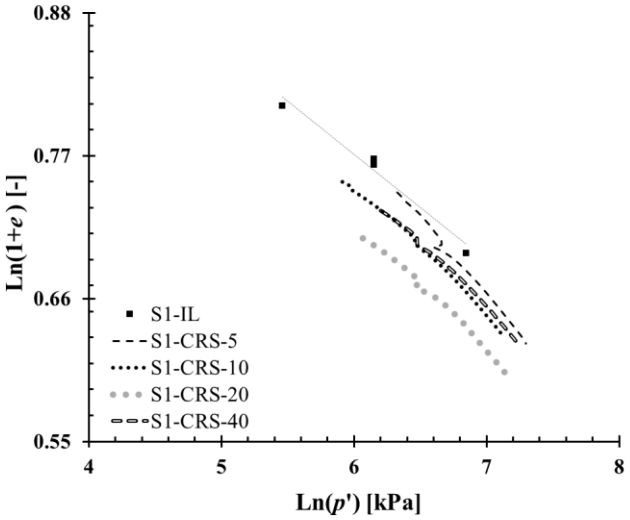

Figure 3-18: Compression range of incremental IL and CRS oedometer tests in the $ln(1+e)$-$ln(p')$ space for Caldas residual soil.

As shown in **Figure 3-18**, different values of N and λ for each curve (test) can be determined. This can be overcome by a normalization of the data. Coop and Cotecchia (1995) and Baudet (2001) suggest the following normalization in the $ln(1+e)$-$ln(p')$ space.

$$v_n = exp\left(\frac{\ln(v) - N_0}{\lambda^*{}_0}\right) \tag{74}$$

where v is the specific volume $(1+e)$ and N_0 and $\lambda^*{}_0$ are the parameters estimated from each test. Applying this normalizing technique, a unique compression line is obtained for all the tested soil specimens, as shown in **Figure 3-19**.

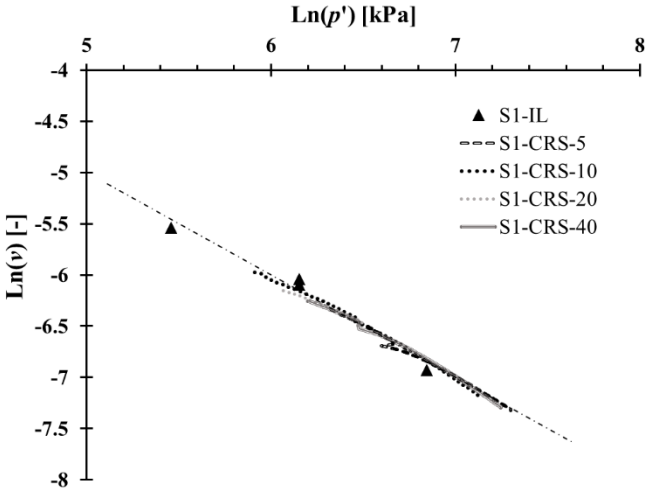

Figure 3-19: Normalized compressibility response for Caldas soil.

For the evaluation of parameter k^*, the unload-reload cycles of each test are presented in **Figure 3-20**. The laboratory tests were performed with one unload-reload cycle denoted as UR, and one unload cycle denoted as U at the end of the test. In IL tests, note that there are not significant differences between each cycle.

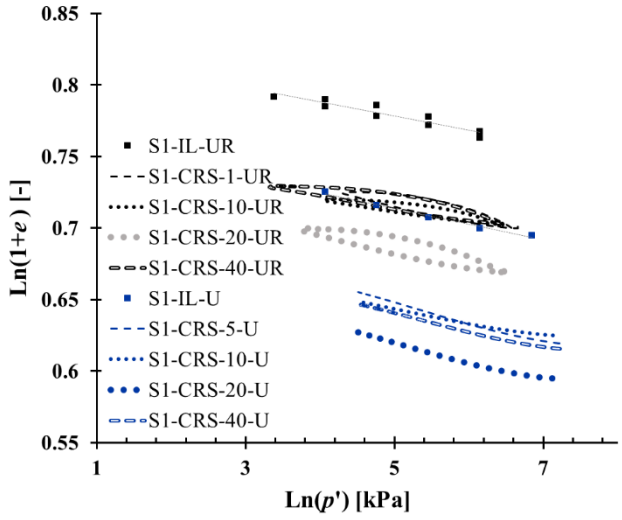

Figure 3-20: Recompression range for the IL and CRS oedometer tests in the $ln(1+e)\ vs\ ln(p)$ space for Caldas Soil – Unload portion

Although the parameter k^* is by definition the slope of the isotropic unloading line in the $ln(1+e)$-$ln(p')$ space, and can be measured directly from the curves shown in **Figure**

3-20, Mašín (2015) suggests to obtain this parameter by a parametric study, simulating isotropic or oedometer compression tests. In this work, optimization techniques were implemented in order to estimate this parameter, starting from the value obtained by the experimental data.

Parameter μ_{pp} was calibrated from drained and undrained shear tests on "undisturbed" soil, as suggested by Mašín (2015). Mašín also recommends reproducing undrained shear tests via FEM discarding the "advanced parameters" which correspond to the Intergranular Strain Concept. The critical state friction angle corresponds to the same parameter estimated for the Modified Cam Clay model, presented in Section 3.2.1.

According to Mašín (2014), the dependency of the initial shear stiffness and effective mean normal stress, can be expressed as follows for the Hypoplastic clay model:

$$G_{vh} = p_r A_g \left(\frac{p'}{p_r}\right)^{n_g} \tag{75}$$

where G_{vh} is the initial shear stiffness (the first letter of the subscript corresponds to the propagation direction of the wave and the second one to the polarization direction) and p_r correspond to a reference pressure, defined as 1 kPa for this model.

For the definition of parameters A_g and n_g, bender element laboratory tests were utilized, which were conducted in triaxial tests following oedometric stress paths. Despite Bender Element tests were carried on during the reconsolidation stage of each triaxial test, they were identified in **Figure 3-21** with the abbreviation of the followed shear stress paths: reduced triaxial extension (RTXE), constant mean normal-unload (CMSU), constant q-load (CQL), and the rest of paths were previously mentioned. The tests identified as K_0-consolidation corresponds to a purely compression tests with no shearing stage.

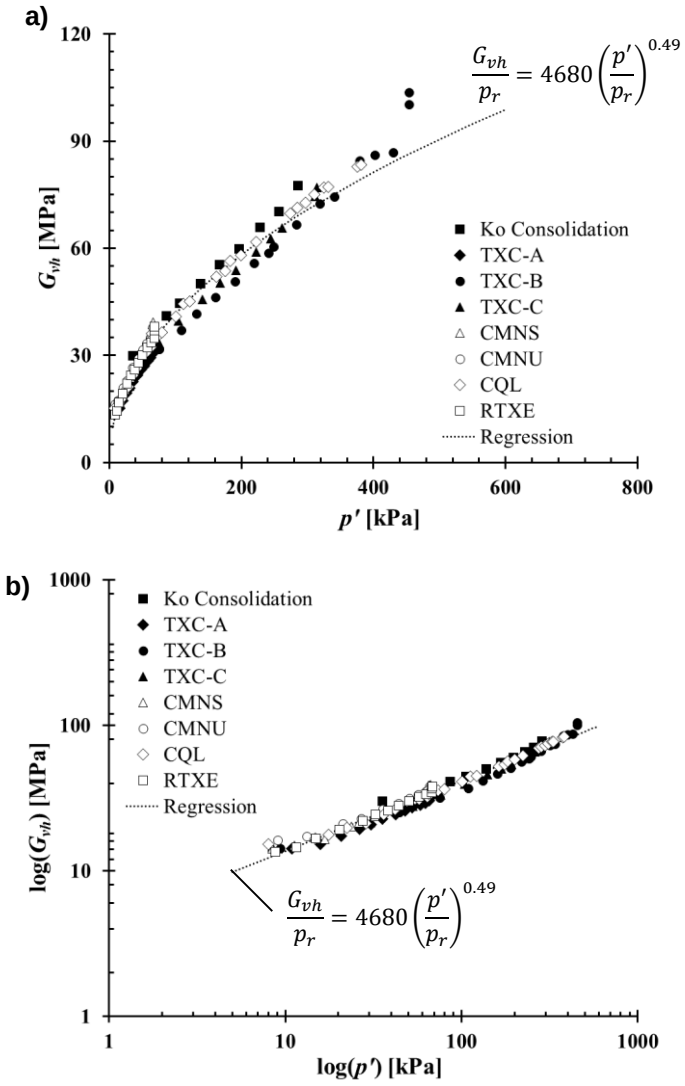

Figure 3-21: Bender Element test results during K_0-reconsolidation – Caldas residual soil. a) Arithmetic space, b) Logarithmic space.

According to the recommendations provided by Mašín (2015), parameter R was treated as a material independent constant ($R = 10^{-4}$). Parameters χ and β_r were determined via optimization techniques. Since there is not enough experimental data to obtain parameter m_{rat}, this parameter was also obtained from inverse analysis.

As mentioned in Section 2.1.3, the numerical models were initialized with the void ratio parameter rather than OCR. The initial void ratio parameter utilized corresponds to the average of the in-situ void ratio measured in the compression tests (IL and CRS). It must be remarked that this parameter must match not only with the compression tests but also

with the triaxial tests. Thus, this parameter was later optimized by inverse analysis in order to reduce the scatter between different void ratio in the soil specimens.

Parameter Pt was determined based on the cohesion of the material Mašín (2017). Its estimation was presented in Section 3.2.2. In this research, the magnitude of the advanced parameter α_f was also determined by inverse analysis to match the experimental results.

3.2.4 Inverse analysis results

Optimization techniques and statistical estimations to define the importance or influence of certain parameters on the soil mechanical response were performed following the procedures indicated in Section 2.2. In this work, the entire statistical observations correspond to the laboratory triaxial tests results conducted on Caldas residual soil (Galeano, 2020), specifically for undrained compression and reduced triaxial extension (U-TXC and U-RTXE, respectively). These responses were also considered for the inverse analyses. Since these observations are represented as response curves, all observations corresponding to the same curve will be weighted with a constant arbitrary value, which means that every single point of the reference laboratory response curve counts with the same importance or accuracy degree. **Table 3-1** summarizes the weights considered for the statistical analysis and computation of the parameter sensitivities.

Table 3-1: Selected weights for the observations.

Test conditions	Response curve - Observation type	Selected Weights
Undrained Triaxial Compression (U-TXC) and Undrained Reduced Triaxial Extension (U-RTXE)	Axial strain (ε_a) - deviatoric stress (q)	σ = 5.0 kPa – Value for q
	Secant shear modulus degradation (G_{sec})	σ = 1.0 MPa – Value for G_{sec}

The laboratory responses were discretized for the statistical analyses considering one observation point each 0.003 (0.3%) of the axial strain (ε_a), while for the secant shear modulus degradation, exactly on the following shear strains (ε_{sh}):

$$\varepsilon_{sh} = \left\{ \begin{matrix} 0.000050;\ 0.000075;\ 0.000100;\ 0.000250; \\ 0.000500;\ 0.000750;\ 0.001000; \\ 0.002500;\ \ 0.007500;\ 0.010000 \end{matrix} \right\} \quad (76)$$

The initial set of parameters for each constitutive model is presented from **Table 3-2** to **Table 3-4**. For both the computation of parameter sensitivities and correlation coefficients, the selected parameters were perturbed with a 20% of their original initial value.

Table 3-2: Initial parameter set considered for statistical analysis and optimization techniques – Modified Cam Clay model.

Symbol	Parameter	Value
λ	Compression index [-]	0.135
k	Swelling index [-]	0.015
v_{ur}	Poisson's ratio [-]	0.2
e_{init}	Initial void ratio for loading/unloading [-]	1.19
M	Tangent of the critical state line [-]	1.506
${K_0}^{NC}$	Coefficient of lateral stress in normal consolidation [-]	0.135

Table 3-3: Initial parameter set considered for statistical analysis and optimization techniques – HSsmall model.

Symbol	Parameter	Value
c'	Cohesion intercept [kPa]	16
φ'	Angle of internal friction [°]	45
ψ	Angle of dilatancy [°]	11
${E_{50}}^{ref}$	Secant stiffness at 50% stress level in standard drained triaxial test [kPa]	7000
${E_{oed}}^{ref}$	Tangent stiffness for primary oedometer loading [kPa]	7500
m	Power for stress-level dependency of stiffness [-]	0
${E_{ur}}^{ref}$	Unloading/ reloading stiffness [kPa]	21000
v_{ur}	Poisson's ratio for unloading-reloading [-]	0.2
p^{ref}	Reference stress for stiffness's [kPa]	100
${K_0}^{NC}$	Lateral earth pressure coefficient parameter[-]	0.41
R_f	Failure ratio [-]	0.9
$\gamma_{0,70}$	Strain at 70% of the G_0 [kPa]	33000
G_0	Very small-strain shear modulus [-]	2.63E-04

Table 3-4: Initial parameter set considered for statistical analysis and optimization techniques – Hypoplastic clay model.

Symbol	Parameter	Value
	Basic Hypoplastic model parameters	
φ'_c	Critical state friction angle [°]	36
λ^*	Slope of the isotropic normal compression line [-]	0.109
k^*	Slope of the isotropic unloading line [-]	0.009
N	Position of the isotropic normal compression line [-]	1.428
μ_{pp}	Parameter controlling the shear stiffness [-]	0.26
	Intergranular strain concept parameters	
A_g	Very small strain shear stiffness parameters [MPa] / [-]	4546
n_g		0.49
m_{rat}	Very small strain behavior upon strain path reversals [-]	0.68
R	Size of the elastic range [-]	1E-04
β_r	Control the rate of evolution of the intergranular strain tensor [-]	0.23
χ		1.8
	Additional parameters	
P_t	Shift of the mean stress due to cohesion [kPa]	16
e	Initial void ratio [-]	1.19
α_f	Translation of the response envelope [-]	0.80

Initially, scaled composite sensitivities and correlation coefficients were obtained for each isolated response. Then, they were computed for an overall response composed by the secant shear modulus degradation and deviatoric stress - axial strain response.

Statistical analyses results for Modified Cam Clay model are presented from **Figure 3-22** to **Figure 3-27**. According to **Figure 3-22**, the parameter v_{ur} has larger influence than parameter e_{init} for the UTXC stress path, in contrast with the URTXE stress path, where e_{init} exhibits more relevance for the deviatoric stress-axial strain soil response. For the secant shear modulus degradation (**Figure 3-23**) both stress paths are more influenced by the changes in the parameter v_{ur}.

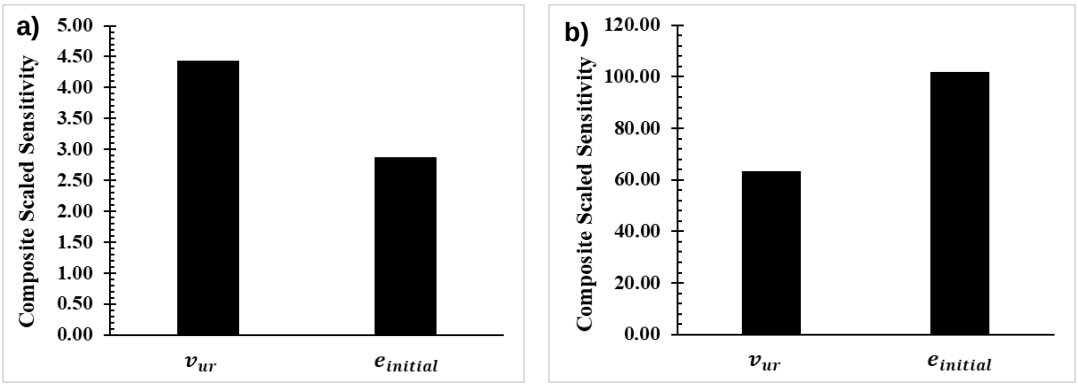

Figure 3-22: Parameters composite scaled sensitivities (css_j) results. Axial strain-deviatoric stress (ε_a-q): a) TXC results and b) RTXE results. Modified Cam Clay model.

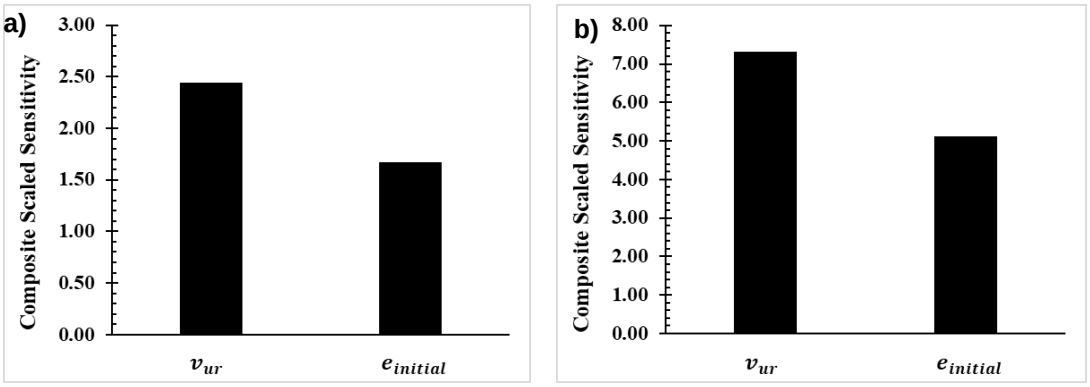

Figure 3-23: Parameters composite scaled sensitivities (css_j) results. Secant shear modulus degradation (G_{sec}): a) TXC results and b) RTXE results. Modified Cam Clay model.

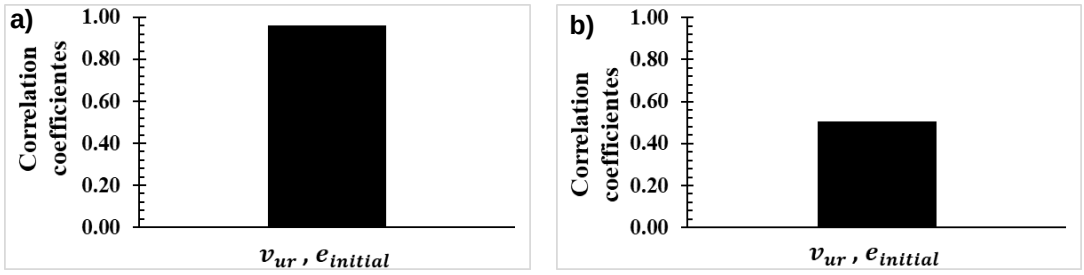

Figure 3-24: Parameter correlation coefficients results. Axial strain-deviatoric stress (ε_a-q) : a) TXC results and b) RTXE results. Modified Cam Clay model.

As shown in **Figure 3-24**, it exists a strong relationship between parameters v_{ur} and e_{init} in the UTXC stress path for the deviatoric stress-axial strain response, while for URTXE, the correlation coefficient is lower than 0.90, which indicates that both parameters could be optimized together. **Figure 3-25** shows that for the secant shear modulus degradation

response both stress paths exhibit high correlation coefficients, indicating that the parameters should be optimized solely.

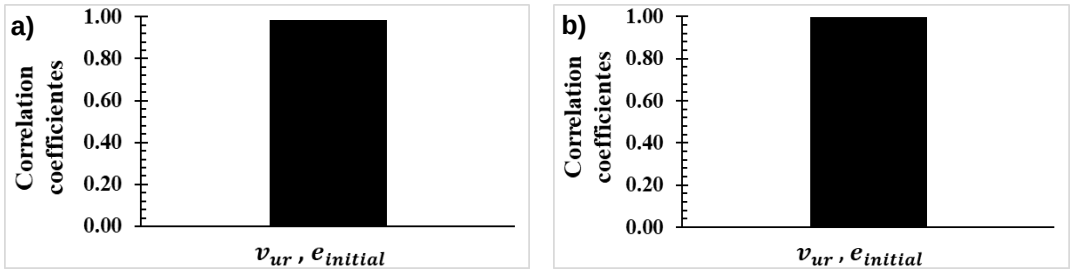

Figure 3-25: Parameters correlations coefficients results. Secant shear modulus degradation (G_{sec}) : a) TXC path and b) RTXE path. Modified Cam Clay model

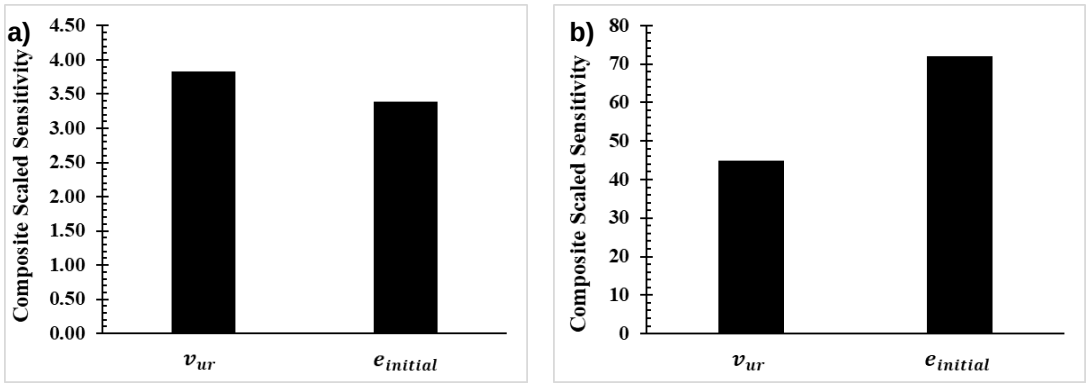

Figure 3-26: Parameters composite scaled sensitivities (css_j) results for overall response. Axial strain-deviatoric stress (ε_a-q) and Secant shear modulus degradation (G_{sec}): a) TXC path and b) RTXE path. Modified Cam Clay model

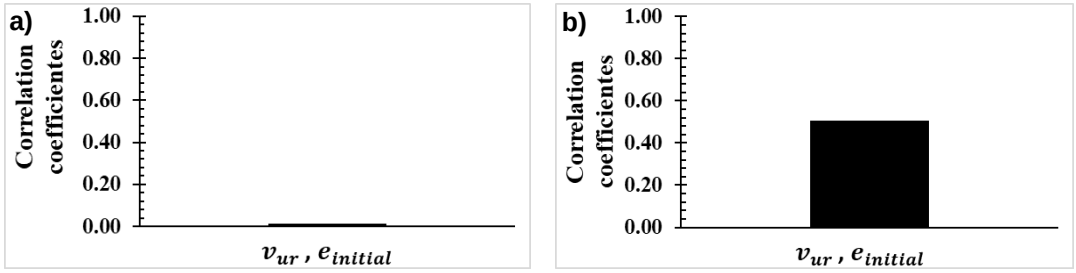

Figure 3-27: Parameters correlations coefficients results for overall response. Axial strain-deviatoric stress (ε_a-q) and Secant shear modulus degradation (G_{sec}): a) TXC results and b) RTXE results. Modified Cam Clay model.

When analyzing both ε_a-q and G_{sec} degradation responses at the same time, the trend remains with being the UTXC stress path more sensitive to the v_{ur} parameter and URTXE more sensitive to the e_{init} parameter, as shown in **Figure 3-26**. Correlation coefficients show a clear decrease when combining both $\varepsilon_a vs\ q$ and G_{sec} degradation responses in the

same analysis, remaining a higher correlation for the RTXE stress path, but anyway under the 0.90 value.

Results from the statistical analyses for the HSsmall Clay model are presented from **Figure 3-28** to **Figure 3-33**.

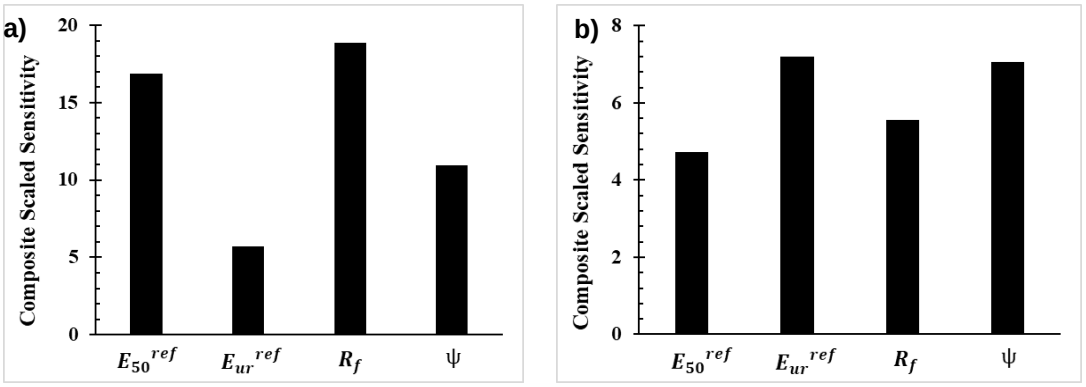

Figure 3-28: Parameters composite scaled sensitivities (css_j) results. Axial strain-deviatoric stress (ε_a-q): a) TXC results and b) RTXE results. HSsmall model.

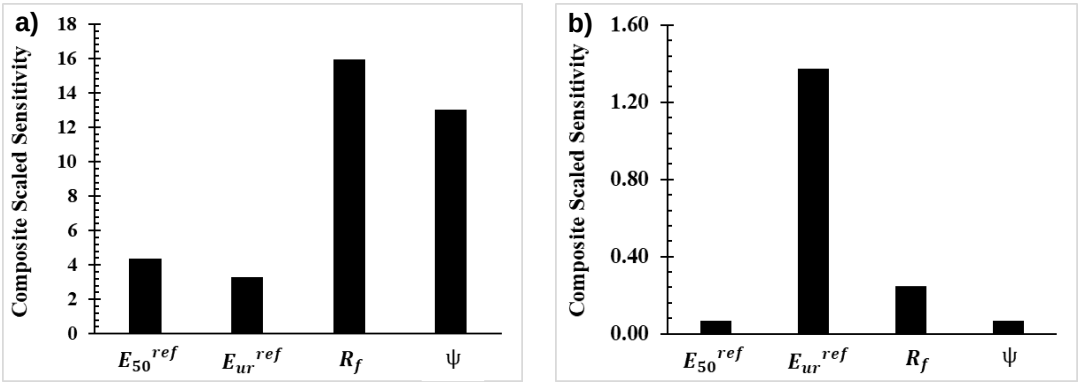

Figure 3-29: Parameters composite scaled sensitivities (css_j) results. Secant shear modulus degradation (G_{sec}) : a) TXC results and b) RTXE results. HSsmall model.

Figure 3-28 shows that the parameter that represents more influence in the ε_a-q response under the UTXC stress path is R_f, and the one with the lowest is $E_{ur}{}^{ref}$, while for URTXE stress path, the most significant parameter is $E_{ur}{}^{ref}$ and the less representative is $E_{50}{}^{ref}$. As shown in **Figure 3-29** for the modulus degradation response, it occurs the same for the parameters R_f and $E_{ur}{}^{ref}$, being both the most relevant for the UTXC and URTXE, respectively. In this case, the differences between the parameter with more relevance and the rest is higher.

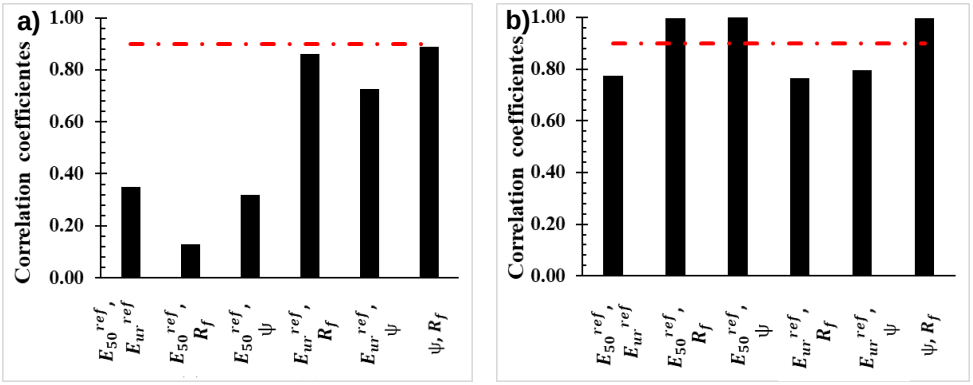

Figure 3-30: Parameters correlations coefficients results. Axial strain-deviatoric stress (ε_a-q) : a) TXC results and b) RTXE results. HSsmall model.

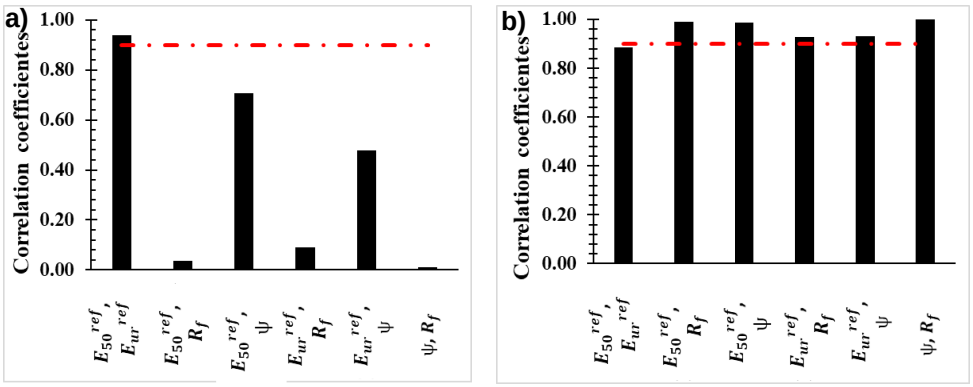

Figure 3-31: Parameters correlations coefficients results. Secant shear modulus degradation (G_{sec}): a) TXC results and b) RTXE results. HSsmall model.

Figure 3-30 shows that for the ε_a-q response in the UTXC stress path, all parameters could be subjected to inverse analysis together since its correlation coefficients are below 0.90, while for the URTXE stress path, there exists a high degree of correlation between parameters ${E_{50}}^{ref}$,ψ; ${E_{50}}^{ref}$,R_f; and ψ,R_f. For the secant shear modulus degradation response (**Figure 3-31**), only parameters ${E_{50}}^{ref}$, ${E_{oed}}^{ref}$ show high correlation for the UTXC stress path, while for URTXE, the only pair of parameters which do not show a correlation coefficient over 0.90 is ${E_{50}}^{ref}$,${E_{oed}}^{ref}$.

Figure 3-32 shows that when analyzing the secant shear modulus degradation and the deviatoric stress-axial strain responses together, the parameter R_f remains as the one with more influence for the UTXC response and ${E_{oed}}^{ref}$ still exhibits the highest influence for the URTXE influence.

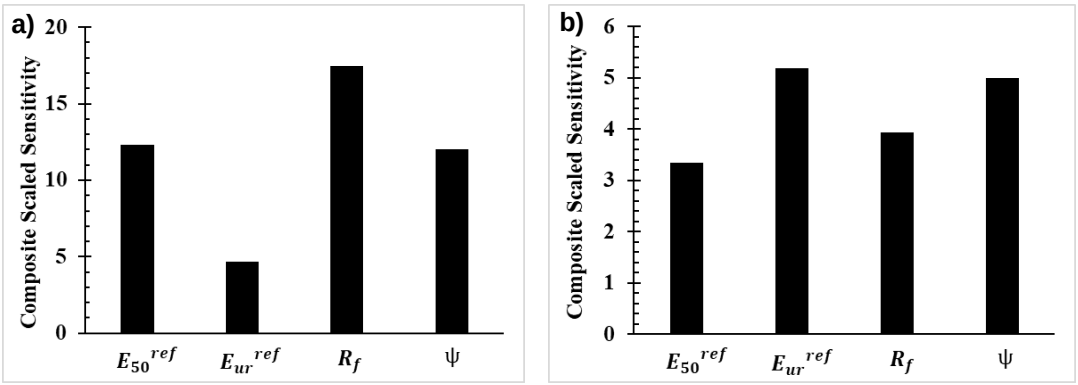

Figure 3-32: Parameters composite scaled sensitivities (css_j) results for overall response. Axial strain-deviatoric stress (ε_a-q) and Secant shear modulus degradation (G_{sec}): a) TXC results and b) RTXE results. HSsmall model.

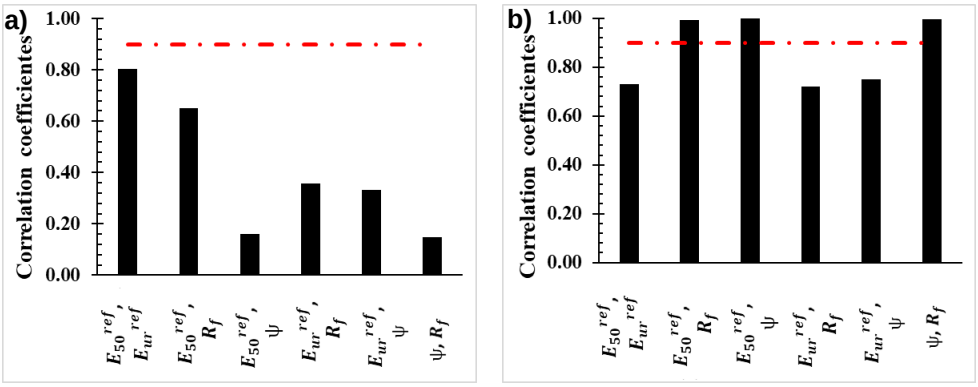

Figure 3-33: Parameters correlations coefficients results for overall response. Axial strain-deviatoric stress (ε_a-q) and Secant shear modulus degradation (G_{sec}): a) TXC results and b) RTXE results. HSsmall model.

For the overall response shown in **Figure 3-33**, there is not high correlation between the constitutive parameters for the UTXC stress path, while for the URTXE stress path, it still remains the high correlation coefficients between parameters $E_{50}{}^{ref}, \psi$; $E_{50}{}^{ref}, R_f$; and ψ ,R_f, indicating that they should not be included together in the same inverse analysis.

Statistical analysis results for the Hypoplastic clay model are presented from **Figure 3-34** to **Figure 3-39**. **Figure 3-34** shows that the more relevant for the deviatoric stress-axial strain response is μ_{pp}, for both UTXC and URTXE stress paths. Parameter m_{rat} exhibits the least sensitivity, which is logical because it is related to the very small strain behavior and the analyzed response is related to large strains.

Figure 3-35 shows that for the secant shear modulus degradation, the parameter which reflects the greatest influence is the μ_{pp} for the UTXC stress path and m_{rat} for the URTXE stress path. It is important to emphasize that despite the largest scaled composite sensitivity for the compression stress path is associated to the parameter μ_{pp}, the parameter m_{rat} exhibit a very similar influence, which reaffirms its influence on the very small strain behavior under compression and extension. As mentioned in Section 2.1.3, the influence of the parameters β_r and χ is mainly focused on the shape of the degradation curve, this means that its influence can be noticeable specifically on a certain portion of the curve, depending on the stress path. Since some specific observation points (points on the degradation curve) are selected for the statistical analyses, it may occur that the influence of these two parameters is not completely captured and for that reason exhibit a lower composite scaled sensitivity than one expects theoretically.

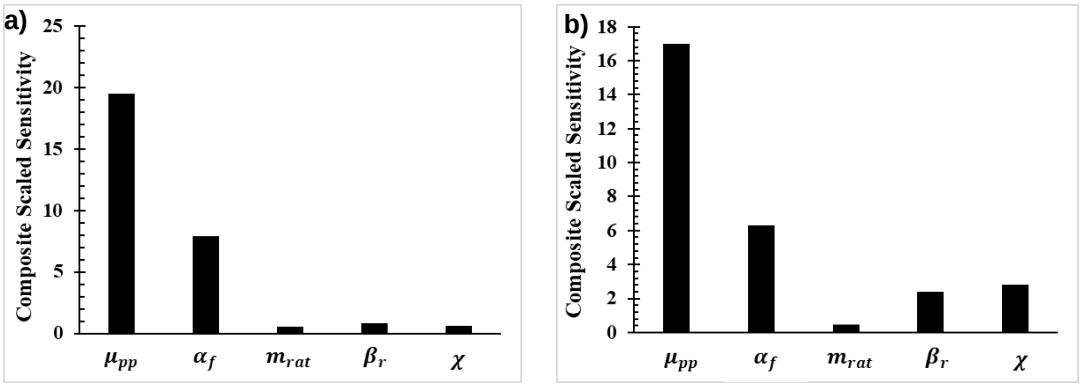

Figure 3-34: Parameters composite scaled sensitivities (css_j) results. Axial strain-deviatoric stress (ε_a-q): a) TXC results and b) RTXE results. Hypoplastic clay model.

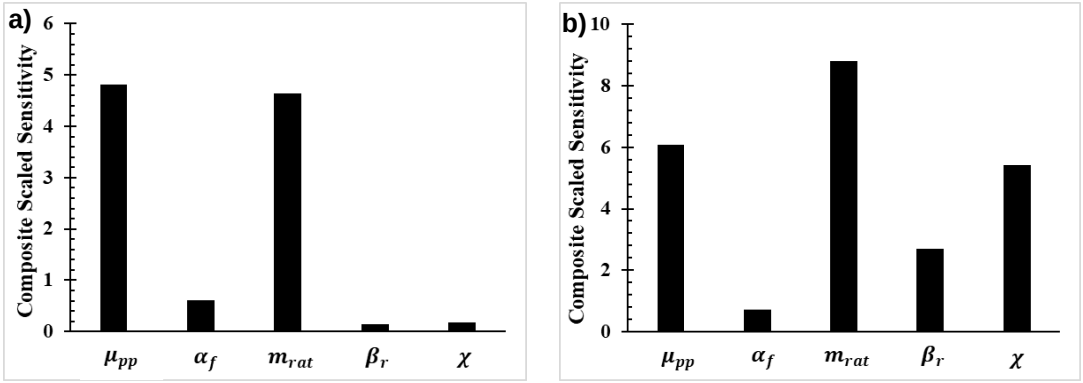

Figure 3-35: Parameters composite scaled sensitivities (css_j) results. Secant shear modulus degradation (G_{sec}): a) TXC results and b) RTXE results. Hypoplastic clay model.

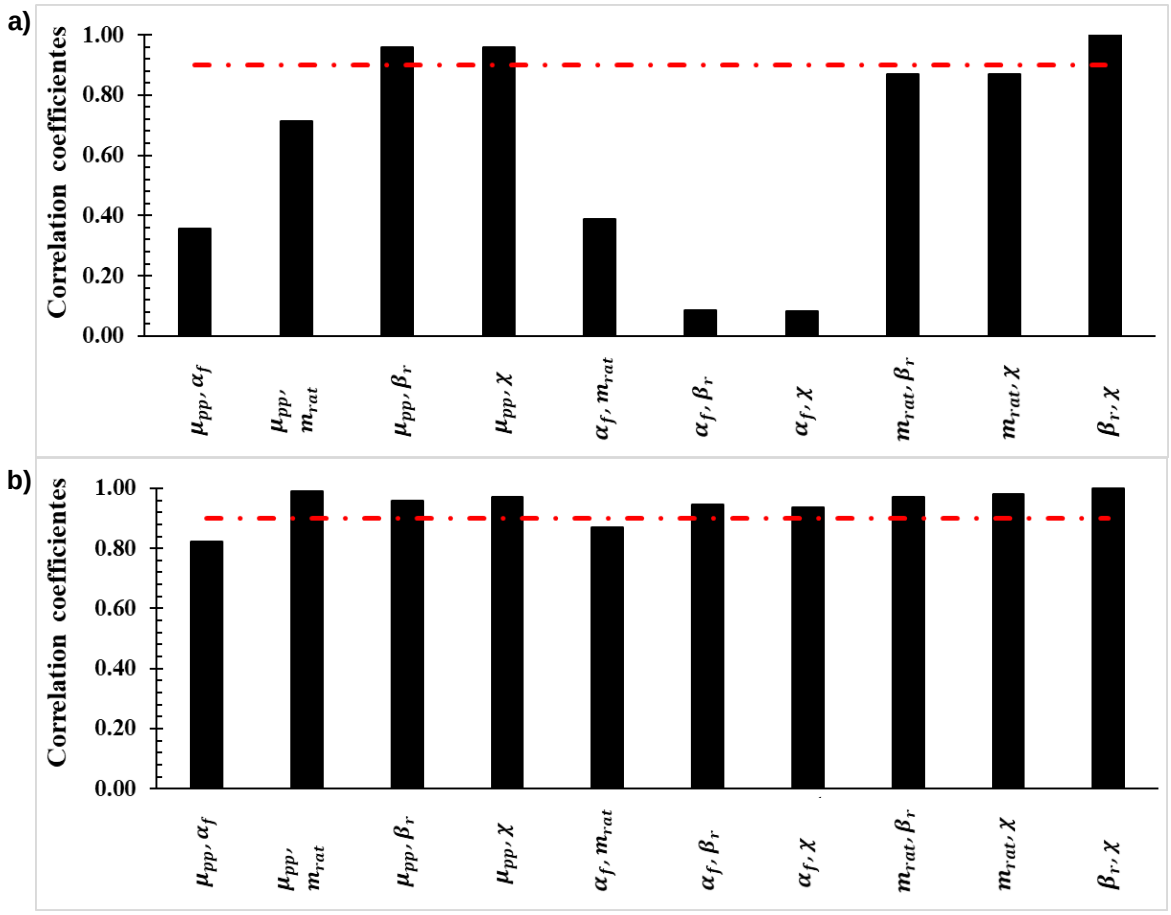

Figure 3-36: Parameters correlations coefficients results. Axial strain-deviatoric stress (ε_a-q): a) TXC results and b) RTXE results. Hypoplastic clay model.

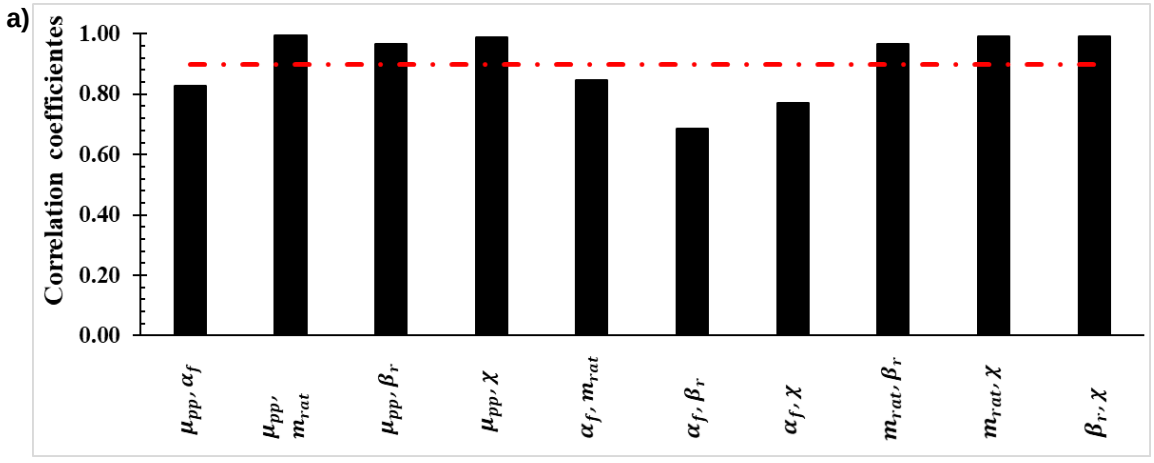

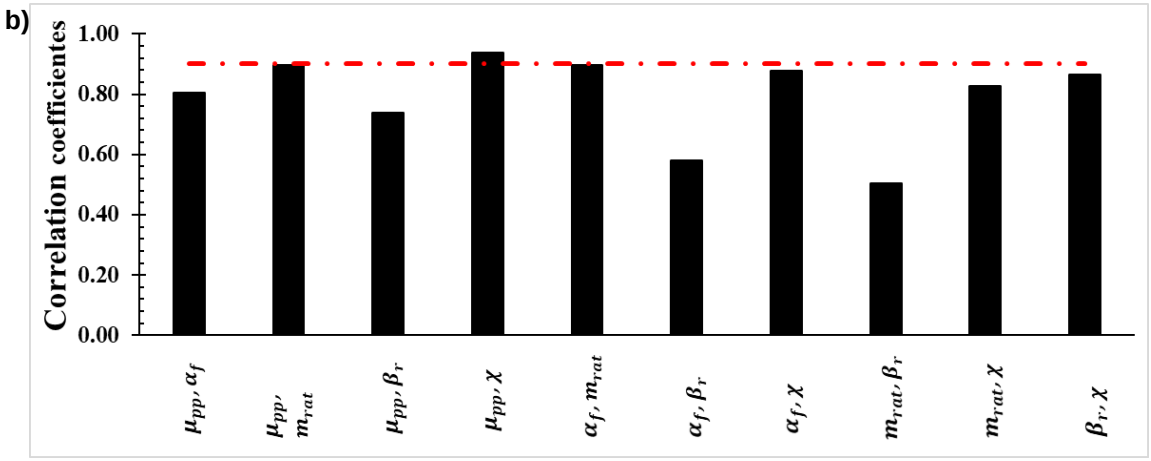

Figure 3-37: Parameters correlations coefficients results. Secant shear modulus degradation (G_{sec}): a) TXC results and b) RTXE results. Hypoplastic clay model.

Figure 3-36 shows that for the deviatoric stress-axial strain response in the UTXC stress path, the parameters that exhibit large correlation are μ_{pp}, χ; μ_{pp},β_r; and β_r, χ, indicating that they should not be optimized together. For the URTXE stress path, it was observed a larger general correlation between parameters μ_{pp},α_f and μ_{pp},m_{rat} are the only pair of parameters with correlation coefficient lower than 0.9. In **Figure 3-37**, it can be observed that for both stress paths it exists a relatively large correlation between parameters in general terms. The only pair of parameters with correlation coefficients lower than 0.9 are the ones related to α_f for the UTXC stress path. For URTXE the only pair of parameters with correlation coefficient larger than 0.90 are μ_{pp},m_{rat}; μ_{pp},χ and α_f,m_{rat}.

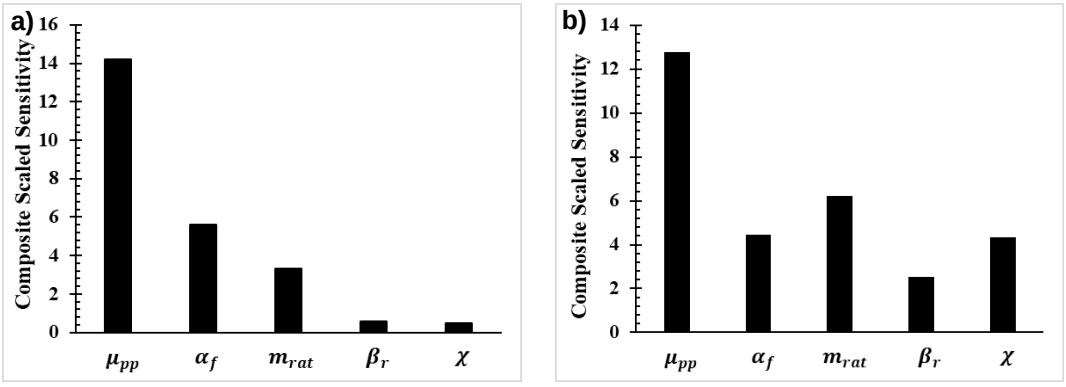

Figure 3-38: Parameters composite scaled sensitivities (css_j) results for overall response. Axial strain-deviatoric stress (ε_a-q) and Secant shear modulus degradation (G_{sec}): a) TXC results and b) RTXE results. Hypoplastic clay model.

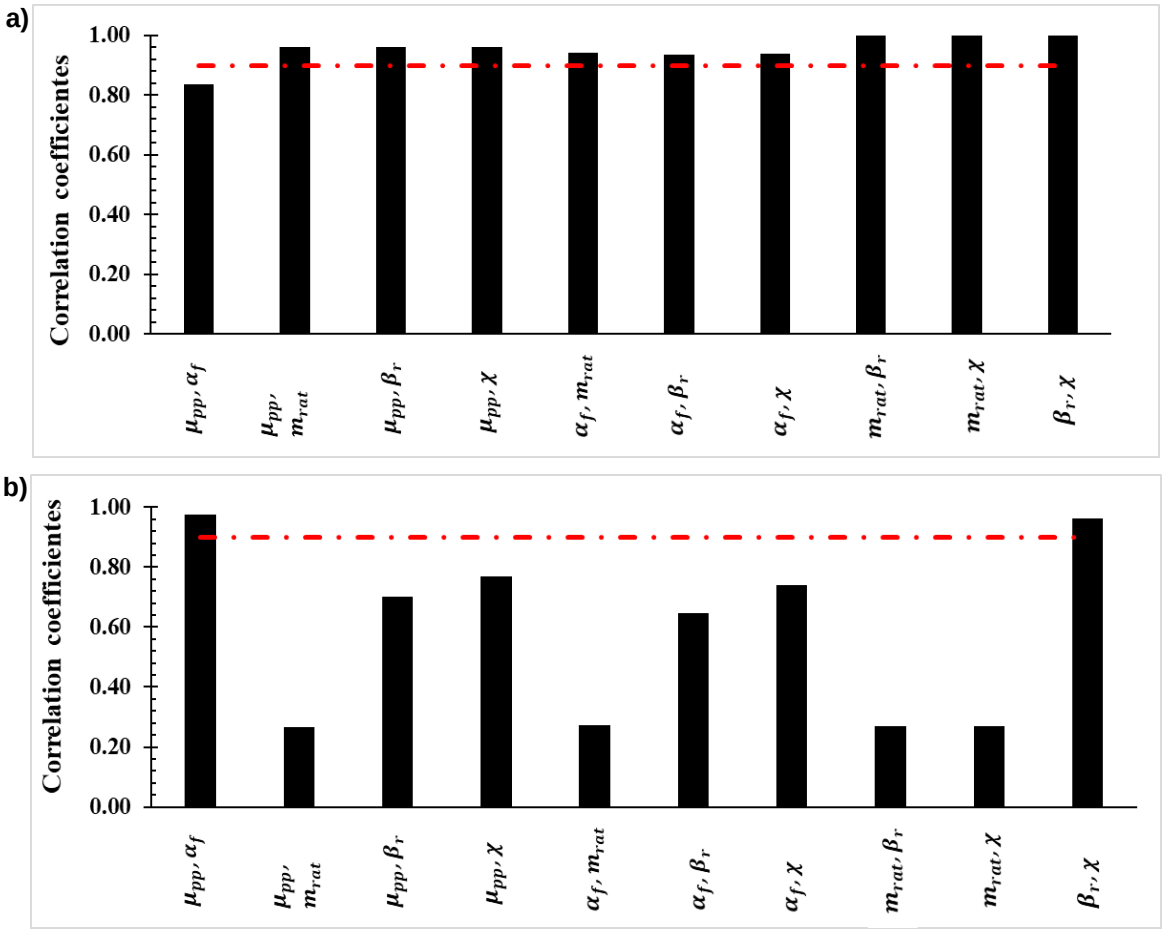

Figure 3-39: Parameters correlations coefficients results for overall response. Axial strain-deviatoric stress (ε_a-q) and Secant shear modulus degradation (G_{sec}): a) TXC results and b) RTXE results. Hypoplastic clay model.

The sensitivity of the parameters on the overall response is presented in **Figure 3-38**. It shows that for both UTXC and URTXE stress paths, the parameter with the greatest relevance is μ_{pp}. In **Figure 3-39**, it can be observed the opposite of what happened with the isolated response, the parameters exhibit a high correlation degree in the UTXC stress path, being the μ_{pp}, α_f the only pair of parameters with a correlation coefficient lower than 0.9. For the URTXE stress path, only two pairs of parameters exhibited a high correlation degree (over 0.9), which correspond to μ_{pp}, α_f and χ,β_r.

According to the statistical analysis results, it was demonstrated that a large sensitivity is associated with large correlation coefficients, which is applicable for all the evaluated constitutive models. Also, it could be observed that the constitutive parameters have

different influence on the model depending on the evaluated response, for instance, a parameter which represents high sensitivity for the secant shear modulus degradation curve under a compression stress path could perfectly represent insignificant importance for the same curve under an extension stress path. It also can be observed that the degree of correlation between parameters is dependent on the amount of data involved in the analysis. Thus, the correlation coefficients will vary between an isolated soil response and an overall response composed by various curves.

The differences found in terms of sensitivities and correlation coefficients for each constitutive model suggest meaningful differences about the effects of each parameter on the soil responses (both isolated and overall) for each stress path, UTXC and URTXE. This was reflected during the inverse analyses that were conducted on both stress paths at the same time, finding out that the resulting parameters did not satisfy the agreement for both paths, or the time consuming was out of the practical applicable range, or the change of the parameters was zero at the end of the process.

As mentioned before, the obtained correlation coefficients were taken into account to organize the sequence of optimization, in order to not have highly correlated parameters in the same inverse analysis run. Since the results of the employed optimization numerical methods depend on the initial value of the parameter, as mentioned in Section 2.2, each inverse analysis was run three times with three different initial parameter values, to finally select the ones which represents the most accurate fit with respect to the experimental data. In this section, the final results of the inverse analyses are presented in terms of fit measurement variables such as the objective function and standard error (as described in Section 2.2).

Table 3-5 and **Table 3-6** show the comparison between the computed initial and final agreement for the three evaluated constitutive models for the UTXC stress path.

Table 3-5: Fit measurement variables. Axial strain-deviatoric stress (ε_a-q) on UTXC stress path.

Fit measurement variable	Constitutive Model					
	Hypoplastic Clay		HSsmall		Modified Cam Clay	
	Initial	Final	Initial	Final	Initial	Final
Variance error [s²]	328	15	126	36	55	51
Standard error [s]	18	4	11	6	7.3	7
Objective function Sb	1639	79	753	217	437	407
Fit improvement	0.952		0.712		0.069	
Residual error*	111716	10513	50682	24178	38192	34695
Visual fit	Bad	Good	Bad	Good	Marginal	Marginal

Table 3-6: Fit measurement variables. Secant shear modulus degradation (G_{sec}) on UTXC stress path.

Fit measurement variable	Constitutive Model					
	Hypoplastic Clay		HSsmall		Modified Cam Clay	
	Initial	Final	Initial	Final	Initial	Final
Variance error [s²]	10	1.3	3.41	3.16	12.75	12.8
Standard error [s]	3	1.1	1.85	1.78	3.56	3.57
Objective function Sb	52	6	20	19	102	102.5
Fit improvement	0.880		0.074		-0.005	
Residual error*	3365	486	1446	1202	2884	3021
Visual fit	Bad	Good	Marginal	Marginal	Bad	Bad

The constitutive model which best capture the soil response measured in the laboratory for the UTXC stress path at the end of the parameter optimization is the Hypoplastic clay model. In general terms, it can be appreciated a higher fit improvement for the $\varepsilon_a vs\ q$ response than for the G_{sec} degradation response. Recall that the differences in terms of fit improvement should not be confused with the general agreement. It must also be emphasized that this constitutive model exhibited the largest fit improvement as well, which means that the most notorious change in terms of agreement. For this stress path, the Modified Cam Clay model exhibited a practically imperceptible agreement improvement for the $\varepsilon_a vs\ q$ response, same as HSsmall model for the G_{sec} degradation response. Negative values obtained in the fit improvement variable suggest that the initial agreement between the experimental data and the simulated data with the average parameters was better than the fit with the last resulting parameters.

It must be clarified that the main objective of this research is to find a constitutive model which represents the mechanical behavior of the Caldas residual soil under different conditions such as drainage and stress shearing paths. It may occur that certain set of parameters represent a good agreement for a specific soil response (*e.g.,* secant shear modulus degradation under an extension stress path) but reflects a non-acceptable fit for the rest of the evaluated responses. If optimization techniques are applied, the resulting optimized set of parameters and simulated response should result on a better overall agreement with respect to the experimental data, but it may cause a fit decrease on particular soil response that probably had an acceptable agreement prior to optimization.

For the UTXC stress path, the lowest fit measurement variables at the end of the parameter optimization were obtained for the Hypoplastic clay model, which indicates that is the model that better represents the soil behavior under the analyzed conditions. **Table 3-7** and **Table 3-8** show the comparison of the computed initial and final fit between the simulated data and experimental laboratory results for the three evaluated constitutive models for the URTXE stress path.

Table 3-7: Fit measurement variables. Axial strain-deviatoric stress (ε_a-q) on URTXE stress path.

Fit measurement variable	Constitutive Model					
	Hypoplastic Clay		HSsmall		Modified Cam Clay	
	Initial	Final	Initial	Final	Initial	Final
Variance error [s²]	122	22	32	16	193	57
Standard error [s]	11	4.5	5	4	13.9	7.6
Objective function Sb	611	112	192	97	1544	462
Fit improvement	0.817		0.495		0.701	
Residual error*	34021	12785	27614	13846	411100	320525
Visual fit	Marginal	Good	Good	Good	Marginal	Marginal

Table 3-8: Fit measurement variables. Secant shear modulus degradation (G_{sec}) on URTXE stress path.

Fit measurement variable	Constitutive Model					
	Hypoplastic Clay		HSsmall		Modified Cam Clay	
	Initial	Final	Initial	Final	Initial	Final
Variance error [s²]	0.212	0.756	0.4	0.52	17.11	15.41
Standard error [s]	0.5	0.870	0.6	0.72	4.14	3.93
Objective function Sb	1.06	3.780	2.5	3.11	136.88	123.28
Fit improvement	-2.547		-0.238		0.069	

Fit measurement variable	Constitutive Model					
	Hypoplastic Clay		HSsmall		Modified Cam Clay	
	Initial	Final	Initial	Final	Initial	Final
Residual error*	145	187	186	286	7761	7015
Visual fit	Good	Good	Good	Good	Bad	Bad

For this stress path, the constitutive model which experimented the higher fit improvement was again the Hypoplastic clay model, specifically for the $\varepsilon_a vs\, q$ response. Under this response, the three models fit was improved. On the other hand, for the G_{sec} degradation response, the measured error increased (so the fit measurement variables increased with respect to the initial values), except for the Modified Cam Clay model which exhibited practically no improvement. It can be observed that for both stress paths the resulting fit improvement is better for the large strain response than for the small strain one. Also, the higher fit measurement variables correspond to the Modified Cam Clay model, what means that is the one which worse represent the Caldas residual soil mechanical behavior for the analyzed conditions.

It can be observed that for the URTXE stress path, both responses showed a slightly better agreement with the HSsmall model rather than with the Hypoplastic clay model. It must be noted that the magnitude of the fit variables corresponds to the selected observation points, and the results could vary if a different quantity of points or different points are selected for the analyses.

Table 3-9 and **Table 3-10** show the comparison of the computed initial and final fit between the simulated data and experimental laboratory results for the three evaluated constitutive models for the URTXE stress path.

Table 3-9: Fit measurement variables for overall response: Axial strain-deviatoric stress (ε_a-q) and Secant shear modulus degradation (G_{sec}) on UTXC stress path.

Fit measurement variable	Constitutive Model					
	Hypoplastic Clay		HSsmall		Modified Cam Clay	
	Initial	Final	Initial	Final	Initial	Final
Variance error [s²]	113	6	48	15	30	28
Standard error [s]	11	2	7	4	5	5
Objective function Sb	1691	86	772	238	539	511
Fit improvement	0.949		0.692		0.052	

Table 3-10: Fit measurement variables for overall response: Axial strain-deviatoric stress (ε_a-q) and Secant shear modulus degradation (G_{sec}) on URTXE stress path.

Fit measurement variable	Constitutive Model					
	Hypoplastic Clay		HSsmall		Modified Cam Clay	
	Initial	Final	Initial	Final	Initial	Final
Variance error [s²]	41	7.8	12	6.2	93	33
Standard error [s]	6	2.8	3	2.5	10	599
Objective function Sb	612	117	148	110	1668	599
Fit improvement	0.809		0.257		0.641	

For the overall response composed by both axial strain- deviatoric stress and Secant shear modulus degradation responses, fit improvement was achieved for the three evaluated constitutive models. This means that the isolated responses in which a fit reduction was found, had less weight than the ones that showed an agreement improvement. The largest fit improvement was again obtained for the Hypoplastic clay model, for both UTXC and URTXE stress paths. However, for the RTXE stress path, the overall soil simulated response exhibited a slightly better agreement for the HSsmall model. The fact that the final fit measurements variables of a model are lower than other, even if its quantified fit improvement is larger, means that both its initial and final agreement are better with respect to the experimental data.

The Modified Cam Clay model was the only one under which the fit improvement was larger under the URTXE than under the UTXC stress path. **Table 3-11** shows the comparison of the computed initial and final fit between the simulated data and experimental laboratory results for the three evaluated constitutive models, under the overall response composed by both URTXE and UTXC stress paths.

Table 3-11: Fit measurement variables for overall response: UTXC and URTXE stress paths.

Fit measurement variable	Constitutive Model					
	Hypoplastic Clay		HSsmall		Modified Cam Clay	
	Initial	Final	Initial	Final	Initial	Final
Variance error [s²]	66	2.8	5	1.5	83	32
Standard error [s]	8	1.4	2	1.2	9.1	6
Objective function Sb	2103	102	192	53	2892	1124
Fit improvement	0.951		0.724		0.611	

The analyzed global soil simulated response shown in **Table 3-11** is composed by both stress paths (UTXC and URTXE) and both singular responses (axial strain-deviatoric stress and secant shear modulus degradation). It can be observed that the Hypoplastic clay model still exhibits the largest fit improvement, and the Modified Cam Clay model is the one with the shortest quantified fit improvement. For this analysis conditions, the best agreement can be observed under the experimental data and the simulated HSsmall model data, presenting little differences with the Hypoplastic clay model. On the other hand, the Modified Cam Clay model exhibits fit measurement variables more than ten times higher than the other two constitutive models, which means the worst agreement with respect to the experimental data.

Considering the parameter optimization results shown and interpreted from **Table 3-5** to **Table 3-11**, it could be concluded that the Hypoplastic Clay and the HSsmall model exhibits better capabilities than the Modified Cam Clay model in order to reproduce Caldas residual soil mechanical behavior. The visual fit presented from **Table 3-5** to **Table 3-9** was an additional subjective agreement measurement method, which can be graphically assessed in Chapter 4, where the graphics with the numerical simulation results are presented.

3.2.5 Definitive set of parameters

From **Table 3-12** to **Table 3-14**, the set of constitutive parameters corresponding to each of the evaluated models is presented.

Table 3-12: Constitutive parameters set – Modified Cam Clay model.

Symbol	Parameter	Initial value	Optimized value
λ	Compression index [-]	0.135	0.135
k	Swelling index [-]	0.015	0.015
v_{ur}	Poisson's ratio [-]	0.2	0.32
e_{init}	Initial void ratio for loading/unloading [-]	1.19	2.05
M	Tangent of the critical state line [-]	1.506	1.506
${K_0}^{NC}$	Coefficient of lateral stress in normal consolidation [-]	0.135	0.135

Table 3-13: Constitutive parameters set – HSsmall model.

Symbol	Parameter [Unit]	Initial value	Optimized value
c'	Cohesion intercept [kPa]	16	16
φ'	Angle of internal friction [°]	45	45
ψ	Angle of dilatancy [°]	11	8
${E_{50}}^{ref}$	Secant stiffness at 50% stress level [kPa]	7000	8000
${E_{oed}}^{ref}$	Tangent stiffness for primary oedometer loading [kPa]	7500	7500
m	Power for stress-level dependency of stiffness [-]	0	0
${E_{ur}}^{ref}$	Unloading/ reloading stiffness [kPa]	21000	28000
v_{ur}	Poisson's ratio for unloading-reloading [-]	0.2	0.2
p^{ref}	Reference stress for stiffness's [kPa]	100	100
${K_0}^{NC}$	Lateral earth pressure coefficient parameter [-]	0.41	0.41
R_f	Failure ratio [-]	0.9	0.5
$\gamma_{0,70}$	Strain at 70% of the G_0 [-]	2.63E-04	2.63E-04
G_0	Very small-strain shear modulus [MPa]	33000	33000

Table 3-14: Constitutive parameters set – Hypoplastic clay model.

Symbol	Parameter [Unit]	Initial value	Optimized value
${\varphi'}_c$	Critical state friction angle [°]	36	36
λ^*	Slope of the isotropic normal compression line [-]	0.109	0.109
k^*	Slope of isotropic unloading line [-]	0.009	0.009
N	Position of the isotropic normal compression line [-]	1.428	1.428
μ_{pp}	Parameter controlling the shear stiffness [-]	0.26	0.062
A_g	Very small strain shear stiffness parameter [-]	4546	4546
n_g		0.49	0.49
m_{rat}	Very small strain behavior upon strain path reversals [-]	0.68	1
R	Size of the elastic range [-]	1E-04	1E-04
β_r	Control the rate of evolution of the intergranular strain tensor [-]	0.23	0.12
χ		1.8	2.2
P_t	Shift of the mean stress due to cohesion [kPa]	16	16
e	Initial void ratio [-]	1.19	1.19
α_f	Translation of the response envelope [-]	0.80	1.15

The agreement between the experimental secant shear modulus degradation curves (small strain behavior) and the numerical simulations is presented from **Figure 3-40** to **Figure 3-42**, comparing the results under the initial and the definitive optimized set of parameters. The soil responses shown on these figures were the ones utilized for the optimization processes.

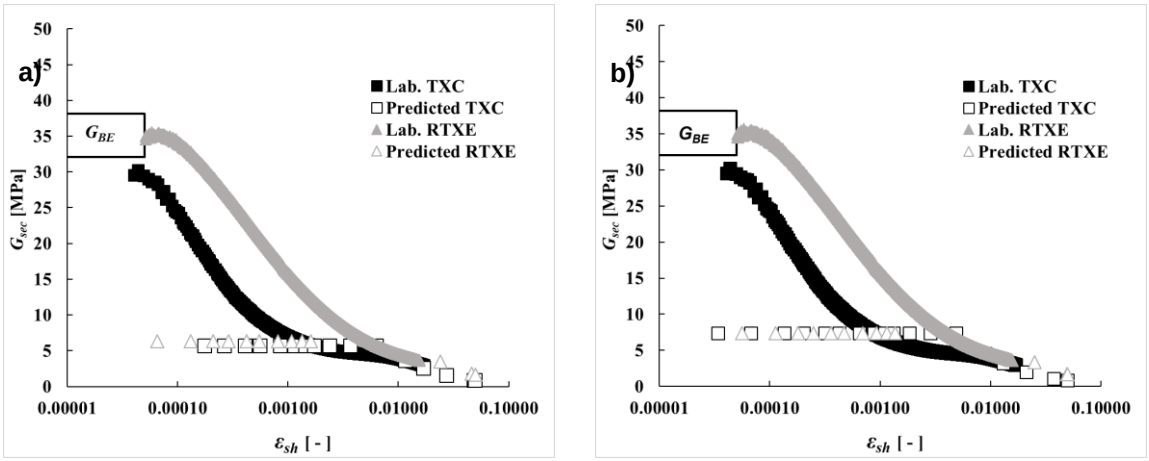

Figure 3-40: Secant shear modulus degradation curves. Modified Cam Clay model a) Initial parameters b) Optimized parameters.

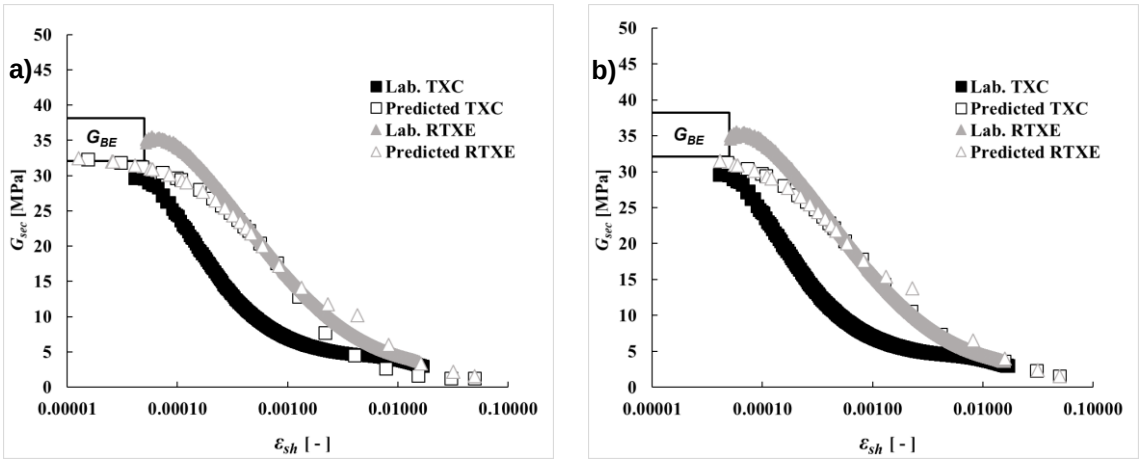

Figure 3-41: Secant shear modulus degradation curves. HSsmall model a) Initial parameters b) Optimized parameters

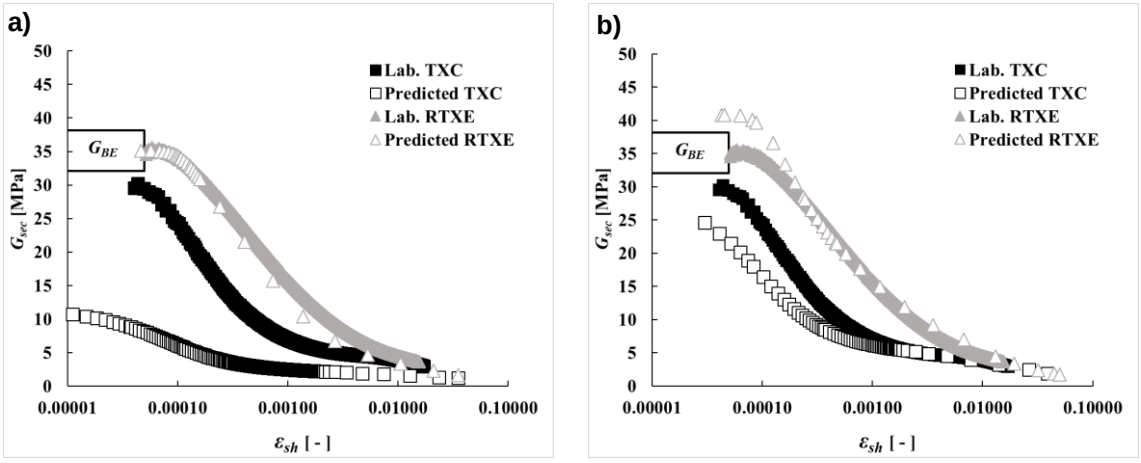

Figure 3-42: Secant shear modulus degradation curves. Hypoplastic clay model a) Initial parameters b) Optimized parameters

The agreement between the experimental axial strain-deviatoric stress curves (large strain behavior) and the numerical simulations is presented from **Figure 3-43** to **Figure 3-45**, comparing the results under the initial and the definitive optimized set of parameters.

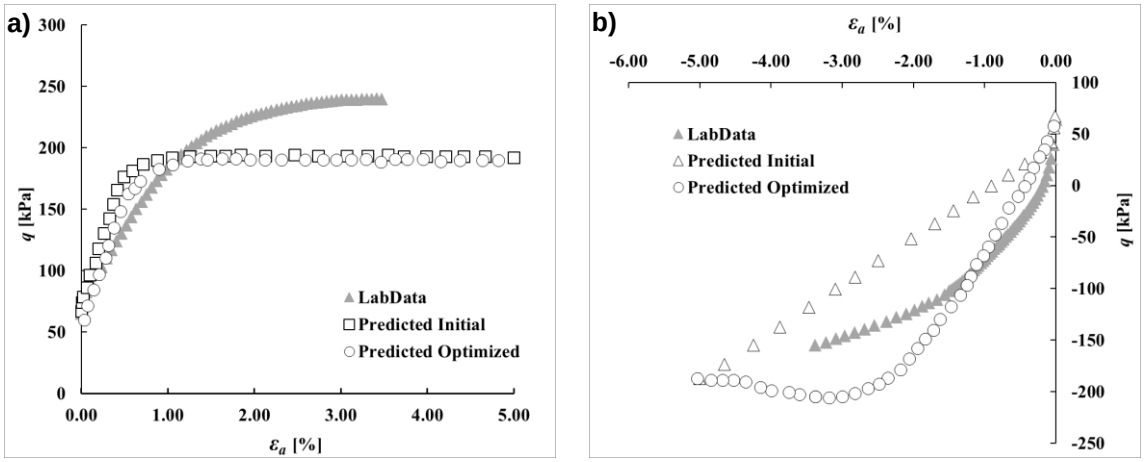

Figure 3-43: Axial strain-deviatoric stress (ε_a-q) curves. Modified Cam Clay model
a) UTXC b) RTXE.

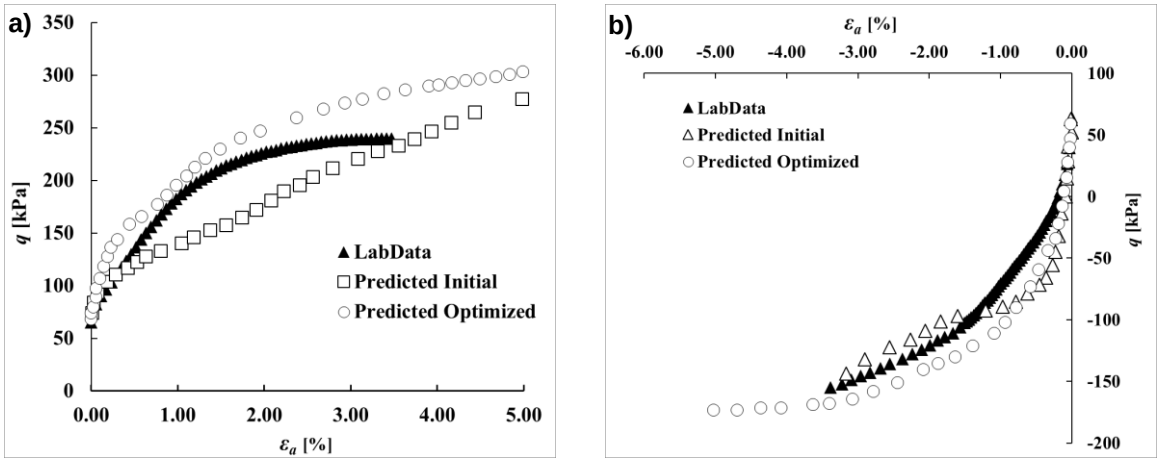

Figure 3-44: Axial strain- deviatoric stress (ε_a-q) curves. HSsmall model
a) UTXC b) RTXE

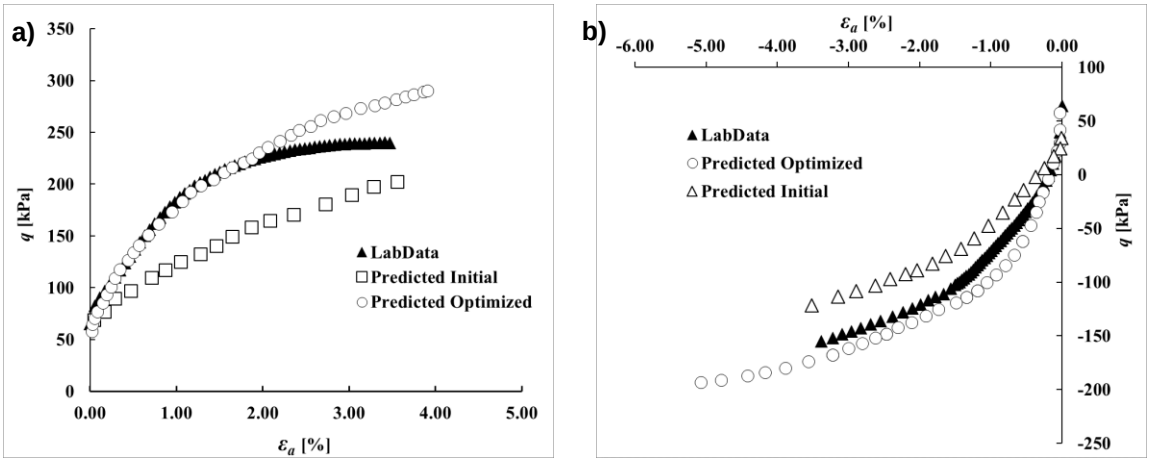

Figure 3-45: Axial strain-deviatoric stress (ε_a-q) curves. Hypoplastic clay model
a) UTXC b) RTXE

4. Numerical Simulation Results

A comparison between the computed soil responses under each of the evaluated constitutive models is presented from **Figure 3-45** to **Figure 4-8**. As it can be observed, the best agreement between the numerical results and the experimental laboratory data is obtained with the Hypoplastic clay model for most of the evaluated responses.

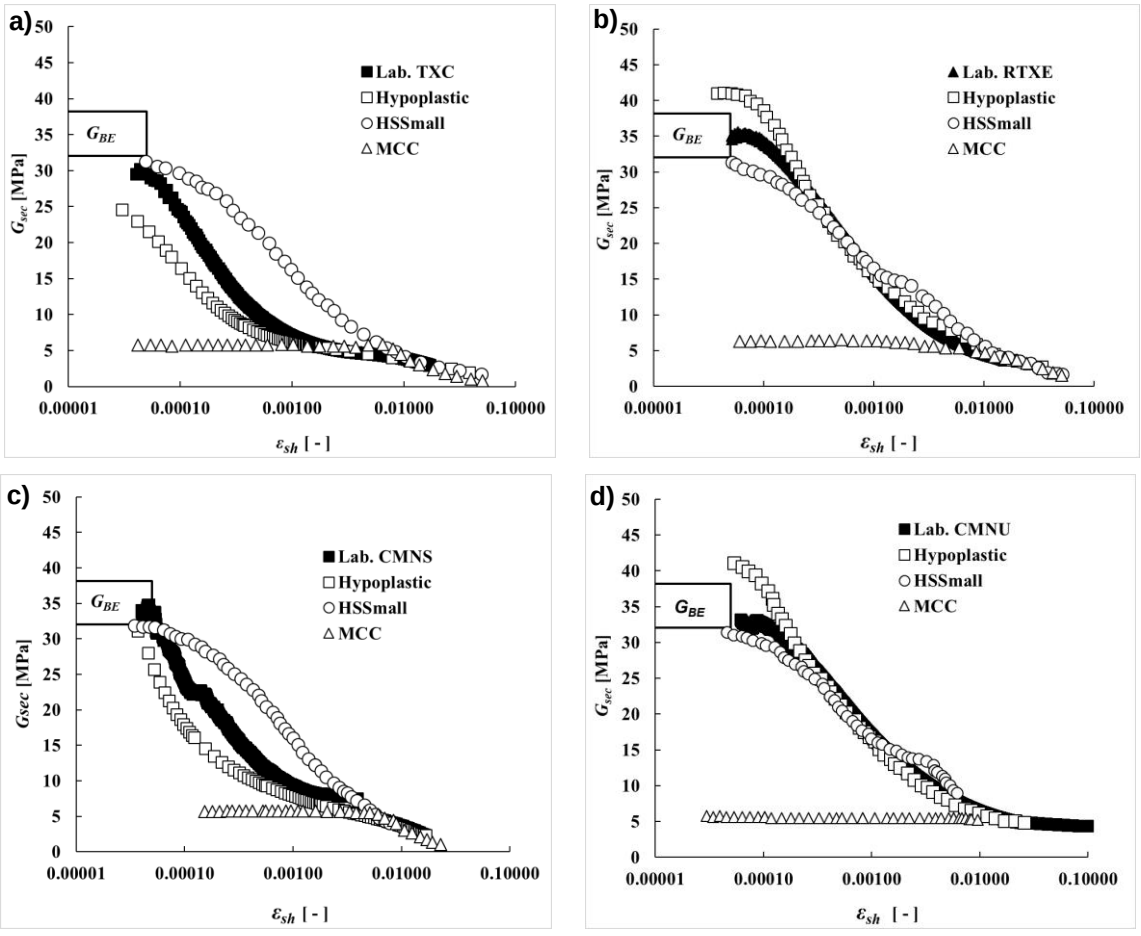

Figure 4-1: Secant shear modulus degradation. Experimental versus simulated data a) UTXC, b) URTXE, c) CMNS, and d) CMNU.

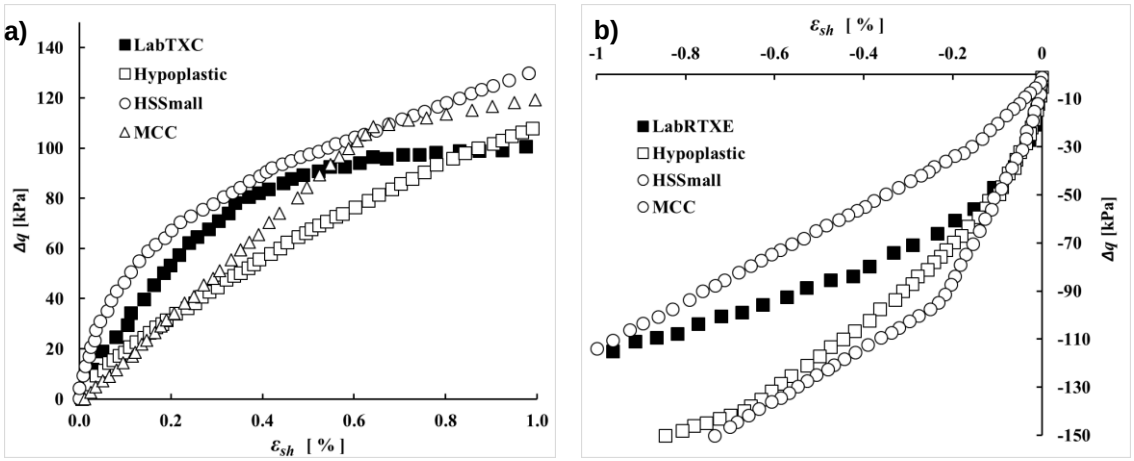

Figure 4-2: *Δq*- shear strain. Constitutive models comparison a) UTXC b) URTXE

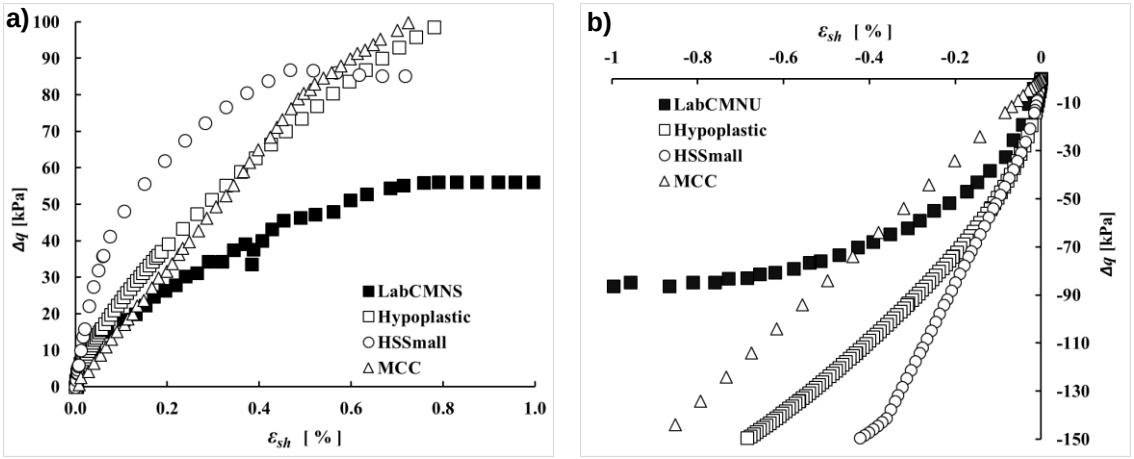

Figure 4-3: *Δq*- shear strain. Constitutive models comparison a) CMNS b) CMNU

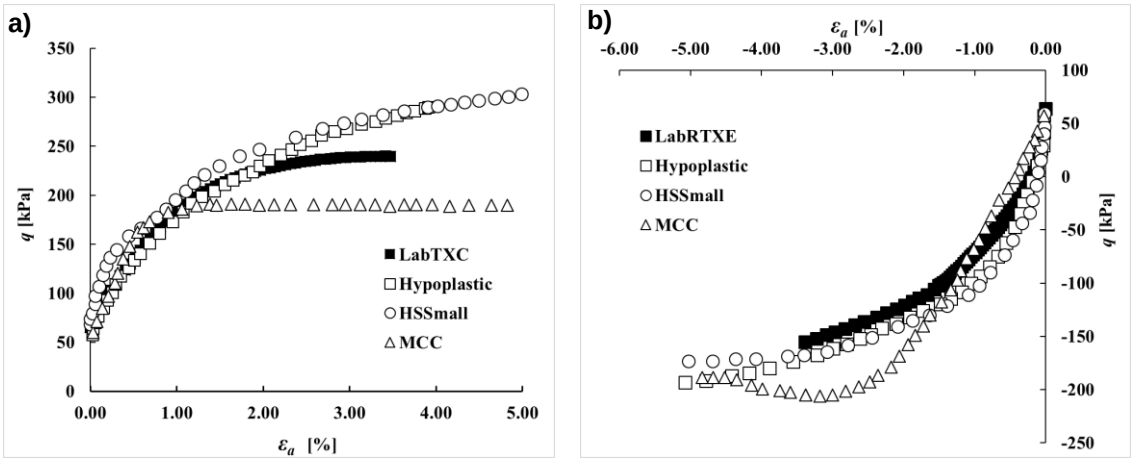

Figure 4-4: Axial strain-deviatoric stress (ε_a-q). Constitutive models comparison a) UTXC b) URTXE.

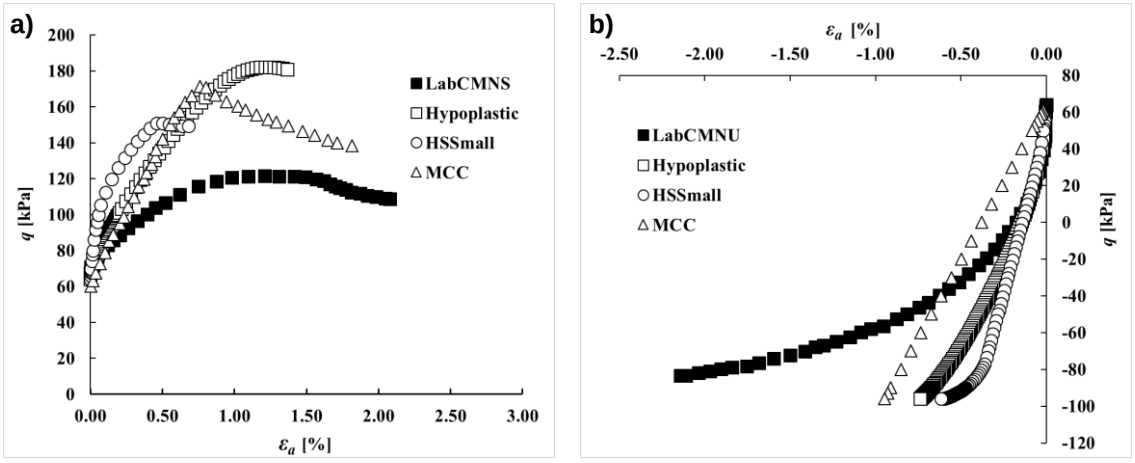

Figure 4-5: Axial strain-deviatoric stress (ε_a-q). Constitutive models comparison a) CMNS b) CMNU.

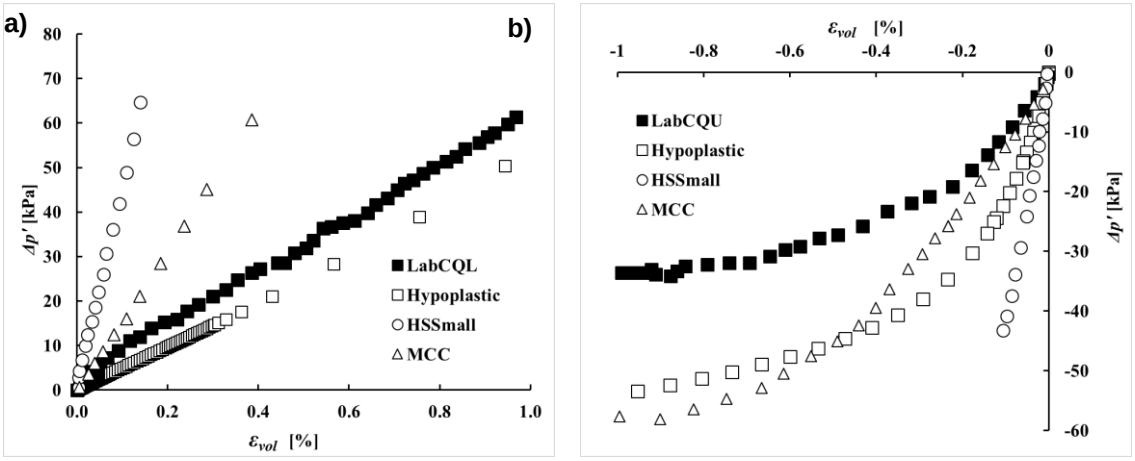

Figure 4-6: Volumetric strain-mean stress (ε_{vol}-$\Delta p'$). Constitutive models comparison a) CQL b) CQU

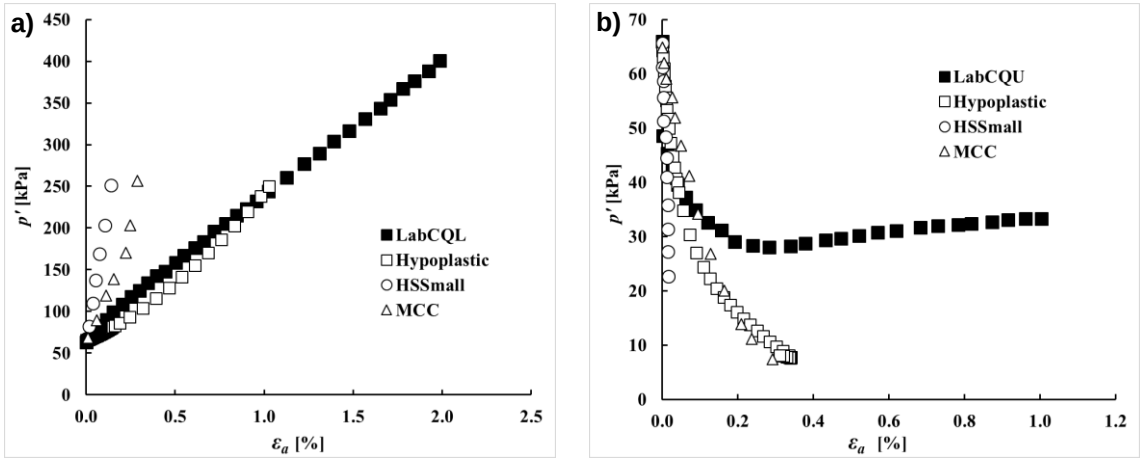

Figure 4-7: Axial strain-mean stress (ε_a-p'). Constitutive models comparison a) CQL b) CQU.

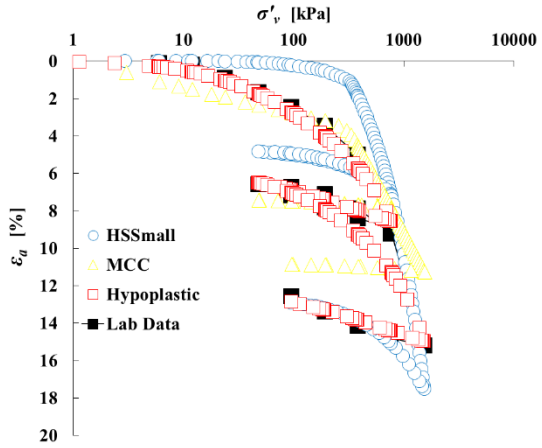

Figure 4-8: 1D compression curves**.** Axial strain-mean stress (ε_a- p') Constitutive models comparison

The experimental results presented by (Galeano 2020) suggest that the stress path rotation angle has more influence on the shear stiffness degradation than on the maximum shear modulus (see **Figure 2-22**). The experimental results agree with the stress path rotation angle concept. Numerical simulation results show that none of the evaluated constitutive models is capable to entirely capture the experimental-measured stress path rotation angle. The Modified Cam Clay model does not even capture the small strain stiffness of the evaluated residual soil; thus, the experimental curves are not even comparable. The HSsmall model does not account for different initial secant shear modulus according to the shearing path. The simulations results stick to the input parameter *G* defined by the user, so that all stress paths exhibit practically the same degradation curve.

The Hypoplastic Clay is the most accurate constitutive model in terms of predicting reasonably well the effects of the rotation angle. This model is capable to represent stiffer responses for larger rotation angles, accounting for the maximum secant shear modulus as for its degradation. However, the Hypoplastic clay model counts with a limitation, it does not permit that the predicted response can reproduce the Finno and Cho (2011) hypothesis of the stiffness measured at very small strain range (see **Figure 2-28**). The reason is that constitutive parameter m_{rat}, which basically represents the stiffness ratio under different stress paths, must necessarily be measured under conventional Triaxial test devices with local strain transducers and not under smaller strain tests such as Bender Element. Thus, the model's stiffness response under different stress paths will always exhibit different G_{max} without the possibility of reaching smaller strains related to the $G_{BE.}$

5. Summary, Conclusions and Recommendations

5.1 Summary

This research was aimed to improve the capability of predicting the laboratory-measured soil mechanical behavior of a Caldas residual fine-grained soil, by finite element models with only one set of constitutive parameters. The assessment of the mechanical behavior was empathized on the small strain behavior, particularly on the secant shear modulus. An advanced experimental laboratory program (Galeano, 2020) was selected to determine the constitutive parameters of the evaluated models, and also to carry on the inverse analyses and comparison with the numerical simulation results. Three constitutive models were employed and calibrated to numerically simulate the mechanical behavior of the residual soil, Modified Cam Clay, Hssmall, and Hypoplastic clay model. The compressibility constitutive parameters were determined under compressional Incremental Loading and Critical Rate of Strain laboratory tests. Critical state and strength parameters were determined from triaxial drained and undrained compression and extension tests. Bender Element tests results were used to determine constitutive parameters related with the very small strain behavior. Parameters related with the soil dilatancy (Hssmall model) were obtained in the basis of the drained triaxial tests.

The finite element software Plaxis 2D® was employed to simulate the laboratory tests conditions such as drainage, constrains, shearing, among others. Axisymmetric conditions were adopted for all the conducted numerical models. The preshearing paths considered for the triaxial tests simulations correspond to an initial stress-free state followed by the back pressure loading, and then followed by the K_0-reconsolidation path. Sampling, transportation and trimming effects were not considered.

Inverse analyses were conducted taking the undrained triaxial tests UTXC and URTXE as targets. Python version 3.10.4 was employed for these optimization techniques along with the Levenberg-Marquardt Method (Moré, 1978). Inverse analyses were employed to determine the constitutive parameters that could not be found on the basis of the experimental laboratory data. In order to determine which parameters should be subjected to optimization techniques, statistical variables such as scaled composite sensitivities and correlation coefficients were computed. Scaled composite sensitivities allowed to know what the importance of parameters with respect to each assessed soil response was. Correlation coefficients allowed to know the degree of correlation between parameters, so that parameters with 0.90 or higher correlation coefficients were not optimized together.

Other variables such as objective function, variance error, standard error and fit improvement were computed to quantify the agreement between the simulated and the experimental data, before and after the inverse analyses. The soil responses assessed by means of statistical variables were related with small and large strain behavior, secant shear modulus degradation and deviatoric stress versus axial strain, respectively, for both UTXC and URTXE. Overall responses composed by $\varepsilon_a vs\, q$ along with G_{sec} degradation were also computed.

5.2 Conclusions

The comparison of the numerical simulations presented in Section 3.2.4 and Chapter 4 demonstrated that the Hypoplastic model for clays (with only one set of parameters) captured soil behavior under one-dimensional compression loading, and different stress shearing compression and extension paths in triaxial conditions, and had an acceptable accuracy for capturing the small stress-strain behavior of the soil, reflected on the degradation of the secant shear modulus and even the effects of the stress path rotation angle. All this shows the capabilities of the mentioned constitutive model to reproduce the soil behavior in terms of compressibility, strength, and stiffness. Hssmall constitutive model exhibited shorter fit measurement variables than the Modified Cam Clay, which means a better agreement with the experimental data.

The Hypoplastic clay was the only model capable to reproduce soil stiffness degradation, accounting for the differences between different stress path rotation angles. This model was capable of represent stiffer responses for larger rotation angles. The Modified Cam Clay model is not capable of capturing the small strain stiffness of the evaluated residual soil, exhibiting low secant shear modulus. Although the HSsmall model can predict the initial shear stiffness of the soil, it does not account for the differences in terms of degradation according to each shearing path. The stiffness degradation curves obtained with the Hssmall model are almost the same regardless the stress path rotation angle.

An important limitation of the Hypoplastic clay model is that it cannot predict secant shear modulus at the very small strain range (Finno and Cho, 2011). The reason is that constitutive parameter m_{rat}, which basically represents the stiffness ratio under different stress paths, must necessarily be measured under conventional Triaxial test devices with local strain transducers and not under smaller strain tests such as Bender Element. Thus, the model's stiffness response under different stress paths will always exhibit different G_{max} without the possibility of reaching smaller strains related to the $G_{BE.}$

It was demonstrated and described in Section 3.2 that most of the parameter identification for the advanced constitutive Hypoplastic clay model can be carried on with common laboratory tests such as Bender Element, Oedometer (Incremental Loading and Constant Rate of Strain, in this work) and triaxial tests, on reconsolidated or undisturbed specimens. Since a few of the parameters which compose the advanced Hypoplastic model for clays need to be obtained by means of specific uncommon laboratory or field tests, parametric analyses and optimization techniques were successfully implemented to achieve a complete model calibration. Under specific conditions, these techniques can supply the additional information needed to determine certain constitutive parameters corresponding to any model.

Despite it was demonstrated that these represent powerful computational tools, optimization techniques must be understood as complement for typical constitutive model calibration procedures, mainly based on laboratory or field experimental data. Inverse analyses cannot replace field and laboratory soil investigations because they only represent mathematical models that can iteratively find parameters, improving the fit between the observed data and the computed soil response. Optimization techniques do not contribute

with real information about the soil mechanical response that can be measured and quantified. Without an accurate engineering judgment, deep knowledge of the adopted constitutive and mathematical algorithm limitations, and enough starting experimental soil data, the implementation of optimization techniques will not be very useful. Specifically, for the studied residual soil and the available experimental laboratory data it was demonstrated that the definitive set of parameters was obtained by optimizing each of them independently rather than optimizing two or more constitutive parameters together. This condition may vary with different objective experimental data such as field-measured displacements and also under a different constitutive model, so the user should always evaluate different ways to conduct the inverse analyses.

There are several factors that influence the results of the prediction of soil response and can cause a lack of accuracy between the experimental data and the modeling results. An example of this could be the selection of an inadequate constitutive model or the disturbance of the soil samples used for laboratory tests, which are the starting point of some constitutive parameters determination.

As remarked by Wichtman (2016), it is difficult to reproduce different kinds of test conditions by a single constitutive model with a single set of parameters, which is supported by the numerical results shown through this work. Some of the most representative shortcomings identified in this work regarding constitutive models capabilities are:

a) Constitutive parameters are often obtained from laboratory test data which do not match exactly when comparing responses. For instance, if there exist significant scatter in terms of void ratio, natural water content or overconsolidation ratios of the evaluated soil specimens, then the simulated response under one constitutive model and one set of parameters would hardly capture all the experimental data with the desired accuracy.

b) The parameter identification of some constitutive models (in a general context) needs some special laboratory and/or field testing programs, which might not be conducted under practical geotechnical applications. Thus, not always exist sufficient available experimental data for a “complete” evaluation. This shortcoming

is more relevant in cases where soil disturbance arising from sampling, transport and/or trimming are detected, so that experimental results are not reliable.

c) Another shortcoming is related to the cases in which inverse analyses are needed. The number of constitutive parameters that can be obtained from optimization techniques depends strongly on the available number of observation points, which are essentially laboratory and/or field tests results. Thus, limited experimental programs will limit the constitutive model's evaluations through optimization techniques.

d) When recourse is made to inverse analyses (optimization techniques) in order to match numerical results with a high number of experimental responses, limitations regarding technology and time could arise. A powerful computational tool that allows to run multiple models under multiple conditions in a row, under acceptable time periods, could be necessary. It would also be needed an advanced optimization tool capable of significantly reduce the measured error between experimental and simulated data. When at least these two requirements are not met, it is normal to observe a good agreement between some experimental results and the numerical simulations, and non-acceptable fit for others.

e) The constitutive models' capabilities are often evaluated under specific conditions, for example in this work, the evaluations were focused on an advanced experimental laboratory program. Other authors have simulated soil mechanical behavior for field conditions such as excavations (*e.g*., Arboleda-Monsalve, 2014; Kim, 2018; Kim and Finno, 2020). The interpretations and conclusions about the performance of any constitutive model should always be carefully taken when trying to extrapolate the results to other geotechnical scenarios (even with the same soil). It is possible that the defined sets of parameters are capable to perform accurately under certain specific conditions, while for other scenarios, another set of parameters or even other constitutive model would be required. An example of this could be found when trying to reproduce the soil mechanical behavior under cyclic loading conditions in laboratory tests with a constitutive set of parameters derived from field tests.

5.3 Recommendations

The estimated definitive set of constitutive parameters presented in this research, can be utilized as a reference for residual fine-grained soils in the south of the Aburrá Valley, specifically from Caldas. It is recommended that the parameters be used in numerical simulations of materials with similar physical and mechanical conditions, including the confinement levels, and the same degree of weathering. **Table 5-1** summarizes the range of the physical and mechanical properties for a soil that would be evaluated under the same constitutive parameters presented herein.

Table 5-1: Ranges of physical and mechanical properties for soil applicability

Properties	Lower limit	Upper limit
Lithological unit according to Dearman (1991)	Horizon VI	
Liquid limit [%]	77.9	77.9
Plastic index [%]	33.4	33.4
Specific gravity [-]	2.62	2.65
Apparent overconsolidation ratio [-]	3.1	4.9
Compression index [-]	0.327	0.0498
Recompression index [-]	0.044	0.059
Void ratio [-]	1.181	1.363

It must be highlighted that quality of the soil characterization and thus, the parameter identification and numerical simulation, is tightly correlated to quality of the soil samples. During field and laboratory procedures some disturbance might arise from soil sample transportation, storage, handling, trimming, among others. These disturbance effects can affect the soil structure so that the mechanical behavior such as stress-strain and strength observed during laboratory tests, may vary with respect to the actual one. In such case, the experimental campaigns and numerical simulations conducted on that soil, will not be representative of the in-situ conditions. Andresen and Kolstad (1979) and Lunne et al. (2006) suggest criteria to evaluate the quality of the soil specimens under the following levels: very good to excellent, good, fair, poor, and very poor. Terzaghi et al. (1996) asserts that laboratory testing conducted on soil samples of good quality (*e.g.*, block, fixed piston, Sherbrooke, or thin-walled samples) provide representative mechanical parameters of the

in-situ conditions. As shown in Section 2.3, the experimental field and laboratory procedures were taken from Galeano's (2020) work, which fulfilled the quality requirements.

For the calibration of the hypoplastic advanced constitutive model, it is recommended to utilize mainly conventional oedometer tests (or isotropic compression tests), undrained triaxial laboratory tests, and bender element tests during the consolidation stage in triaxial testing. An example of the considered laboratory tests results in this research is presented in Section 2.3, including the theory of some other parameter identification. Since parameters that compose the Hypoplastic clay model are advanced, it may be necessary to complement the conventional calibration procedures with parametric analysis and inverse modeling. The main parameters recommend to be obtained by means of parametric or inverse analyses are k^*, χ, β_r, m_{rat}, μ_{pp} and α_G (Mašín, 2015, 2017).

In order to determine which parameters should be estimated through inverse analysis, the user must consider their influence in the mechanical soil response. The computation of composite scaled sensitivities, correlation coefficients, and other statistical variables can be carried out for this purpose, as mentioned in Section 2.2. It's recommended not to run optimization techniques on two or more highly correlated constitutive parameters (see Chapters 2.2 and 3.2.4). Besides the observed visual fit between the simulated and experimental soil response, the evaluation the mentioned statistical variables and others such as fit improvement, standard error, and variance error, are also recommended to quantify the changes in terms of agreement, as it was developed in this work.

The Hypoplastic advanced modelling approaches (Mašín, 2018) for stable and meta-stable structure, rate effects, partial saturation and very small strain stiffness anisotropy, could represent a good opportunity to deepen the evaluation of constitutive models capable to predict residual soils mechanical behavior.

References

Área Metropolitana del Valle de Aburrá. (2007). Plan de Ordenación y Manejo de la Cuenca del río Aburrá, POMCA.

Alonso, E., Gens, A., and Josa, A. (1990). “A constitutive model for partially saturated soils.” *Géotechnique*, 40(3), 405–430.

Andresen, A., and P. Kolstad. (1979). “The NGI 54-mm sampler for undisturbed sampling of clays and representative sampling of coarser materials.” In Proc., of the Int. Conf. on Soil Sampling, 13-21. Oslo, Norway: Norwegian Geotechnical Institute.

Arboleda-Monsalve, L. (2014). “Performance, Instrumentation and Numerical Simulation of One Museum Park West Excavation.” Doctor of Philosophy Dissertation, Northwestern University, Evanston, Illinois.

Arboleda-Monsalve, L., Teng, F., Kim, T. and Finno, R. (2017). “Numerical Simulation of Triaxial Stress Probes and Recent Stress-History Effects of Compressible Chicago Glacial Clays.” *Journal of Geotechnical and Geoenvironmental Engineering*. 143(7) 04017029.

Atkinson, J. H., Richardson, D., and Stallebrass, S. E. (1990). “Effect of recent stress history on the stiffness of overconsolidated soil.” *Géotechnique*, 40(4), 531–540.

Baba, K., Bahi, L., Ouadif, L., and Akhssas, A. (2012). "Slope Stability Evaluations by Limit Equilibrium and Finite Element Methods Applied to a Railway in the Moroccan Rif" *Open Journal of Civil Engineering*, 2(1), 27-32.

Baudet, B. (2001). “Modeling effects of structure in soft natural clays.” PhD thesis, City University, London.

Baudet, B.A., Stallebrass, S.E. (2004). “A constitutive model for structured clays”. *Géotechnique,* 54(4), 269–278.

Becker, D. E., J. H. A. Crooks, K. Been, and M. G. Jefferies. (1987). “Work as a criterion for determining in situ and yield stresses in clays.” *Can. Geotech. J.*, 24 (4), 549–564.

Benz, T. (2006). Small-Strain Stiffness of Soils and its Numerical Consequences. PhD thesis, Universität Stuttgart.

Boulanger, R. W., and Ziotopoulou, K. (2018). “PM4Silt (Version 1): A silt plasticity model for earthquake engineering applications.” Report No. UCD/CGM-18/01, Center for Geotechnical Modeling, Department of Civil and Environmental Engineering, University of California, Davis, CA, 108 pp.

Brinkgreve, RBJ. (2005). “Selection of soil models and parameters for geotechnical engineering application”. *Geo-Frontiers Congress, Austin, Texas, Soil Constitutive Models: American Society of Civil Engineers (ASCE)*, Reston,Virginia, 69-98.

Brinkgreve, R.B.J., Engin, E. and Swolfs, W.M. (2017). Plaxis 2D manual. Rotterdam, Netherlands, Balkema.

Calvello, M. (2002). “Inverse Analysis of a Supported Excavation through Chicago Glacial Clays*.”* Doctor of Philosophy Dissertation, Northwestern University, Evanston, Illinois.

Callisto, L., and Rampello, S. (2002). “Shear strength and small-strain stiffness of a natural clay under general stress conditions.“ *Géotechnique*, 52(8), 547–560.

Chiu, C. F., and C. W. W. Ng. (2014). “Relationships between chemical weathering indices and physical and mechanical properties of decomposed granite.” *Eng. Geol*., 179, 76–89.

Cotecchia, F., Chandler, J. (2000). “A general framework for the mechanical behaviour of clays.” *Géotechnique,* 50(4), 431–447.

Coop, M. R., and Cotecchia, F. (1995). “The compression of sediments at the archeological site of Sibari.” *The interplay between geotechnical engineering and engineering geology: XI ECSMFE; proceedings of the eleventh European Conference on Soil Mechanics and Foundation Engineering: Vol. 8: Case histories demonstrating interplay,* Danish Geotechnical Society, Copenhagen, 19-26.

Dearman, R. (1991). *Engineering Geological Mapping*, Butterworth-Heinemann Ltda., Oxford.

Desai, C.S., and Zaman, M. (2014). *Advanced Geotechnical Engineering, Soil–Structure Interaction Using Computer and Material Models*., Taylor & Francis Group, Florida.

Ellison, K.C., Soga, K., and Simpson, B. (2012). “A strain space soil model with evolving stiffness anisotropy.” *Géotechnique*, 62(7), 627–641.

Finno, R. J., and Kim, T. (2012). “Effects of Stress Path Rotation Angle on Small Strain Responses.” *J. Geotech. Geoenvironmental Eng*., 138(4), 526–534.

Finno, R. J., and Cho, W. (2011). “Recent stress history effects on compressible Chicago glacial clays.” *J. Geotech. Geoenviron. Eng.*,137(3), 197–207.

Galeano, D.I. (2020). “Estimation of Dynamic Parameters in Residual Soils Derived from Crystalline Rocks Based on Geophysical Multichannel Analysis of Surface Waves tests.” Doctor of Philosophy Dissertation, Universidad Nacional de Colombia, Medellin, Colombia.

Graham, J., and Houlsby, G. T. (1983). “Anisotropic elasticity of a natural clay.” *Géotechnique*, *33*(2), 354-354.

Gudehus, G. (1996). “A comprehensive constitutive Equation for granular materials.” *Soils and Foundations*, 36(1), 1–12.

Gudehus, G., Amorosi., A., Gens, A., Herle, I., Kolymbas, D., Mašín, D., Muir Wood, D., Nova, R., Niemunis, A., Pastor, M., Tamagnini, C., and Viggiani, G. (2008). “The soilmodels.infoproject.” *International Journal for Numerical and Analytical Methods in Geomechanics*, *32*(12), 1571-1572.

Hardin, B.O., Drnevich, V.P. (1972). “Shear modulus and damping in soils: Design equations and curves.” *Journal of the Soil Mechanics and Foundations Division*, 98(SM7), 667–692.

Hájek, V., Mašín, D., Boháč, J. (2009). “Capability of constitutive models to simulate soils with different OCR using a single set of parameters.” *Computers and Geotechnics*, 36(4), 655-664.

Herle, I., and Kolymbas, D. (2004). “Hypoplasticity for soils with low friction angles.” *Computers and Geotechnics*, 31(5), 365–373.

Hill, M. C. (2000). “Methods and Guidelines for Effective Model Calibration.” *Joint Conference on Water Resource Engineering and Water Resources Planning and Management*, (Ed: Hotchkiss, R.H., and Glade, M.), Pullman, Washington, 124-134.

Hsiung, B.C.D. and Dao, S.D. (2014). “Evaluation of Constitutive Soil Models for Predicting Movements Caused by a Deep Excavation in Sands”. *Electronic Journal of Geotechnical Engineering,* 19: 17325-17344.

Jaky, J. (1944). “A nyugalmi nyomas tenyezoje” [The coefficient of earth pressure at rest]. [In Hungarian]. *Journal of the Society of Hungarian Engineers and Architects*, 78(22), 355–358.

Jardine, R. J. (1992). “Some observations on the kinematic nature of soil stiffness.” *Soils Found.*, 32(2), 111–124.

Kim, S. (2018). “Observed Performance and Inverse Analysis of a Sheet Pile-Supported Excavation in Chicago Clays” Doctor of Philosophy Dissertation, Northwestern University, Illinois, U.S.

Kim, S., and Finno, R. J (2020). “Inverse analysis of Hypoplastic Clay model for computing deformations caused by excavations” *Computers and Geotechnics*, 122, 103499.

Knabe, T., Schweiger, H. F. and Schanz, T. (2012). “Calibration of constitutive parameters by inverse analysis for a geotechnical boundary problem”. *Can. Geotech. J*., 49(2), 170–183.

Kolymbas, D. (1978). “Eine konstitutive Theorie für Böden und andere körnige Stoffe”. Ph.D. Thesis, University of Karlsruhe.

Krahn, J. (2003). “The 2001 R.M. Hardy Lecture: The limits of limit equilibrium analyses”. *Can. Geotech. J*., 40(3), 643-660.

Ladd, C. C., and D. J. DeGroot. (2003). “Recommended practice for soft ground site characterization.” In Proc., of the 12th Panamerican Conference on Soil Mechanics and Geotechnical Engineering, 3–57. MIT, Cambridge: Massachusetts Institute of Technology.

Lade, P.V. (2005). “Overview of Constitutive Models for Soils”. *ASCE Geotechnical Special Publication No.128, Soil Constitutive Models: Evaluation, Selection and Calibration,* Geo-Frontiers Congress 2005, Austin, Texas, 1-34.

Lanier, J., Caillerie, D., Chambon, R., Viggiani, G., Bésuelle, P., and Desrues, J. (2004). “A general formulation of hypoplasticity.” *International Journal for Numerical and Analytical Methods in Geomechanics*, 28(15), 1461-1478.

Lim, J. X., Chong, S. Y., Tanaka, Y., and Lee, M. L. (2019). “CI and CK0 Triaxial Tests for Tropical Residual Soil in Malaysia.” *1st Malaysian Geotechnical Society (MGS) and Geotechnical Society of Singapore (GeoSS) Conference: Geotechnics in Urban Infrastructure*, Petaling Jaya, Malaysia.

Liu Xinyu, Xianwei Zhang, Lingwei Kong, Xinming Li, Gang Wang. (2021). “Effect of cementation on the small-strain stiffness of granite residual soil”. *Soils and Foundations*, 61(2), 520-532.

Lunne, T., T. Berre, K. H. Andersen, S. Strandvik, and M. Sjursen. (2006). “Effects of sample disturbance and consolidation procedures on measured shear strength of soft marine Norwegian clays.” *Can. Geotech. J.*, 43 (7), 726-750.

Mašín, D. (2005). “A Hypoplastic constitutive model for clays.” *International Journal for Numerical and Analytical Methods in Geomechanics*, *29*(4), 311–336.

Mašín, D., and Herle. I., (2005). “State boundary surface of a Hypoplastic model for clays.” *Computers and Geotechnics*, 32(6), 400–410.

Mašín, D. (2007). “A Hypoplastic constitutive model for clays with meta-stable structure”. *Can. Geotech. J.*, 44(3), 363–375.

Mašín, D. (2013). “Clay hypoplasticity with explicitly defined asymptotic states.” *Acta Geotechnica*, *8*(5), 481–496.

Mašín, D. (2015). *Hypoplasticity for practical applications.* PhD Course on hypoplasticity. Zhejiang University.

Mašín, D. (2017). “PLAXIS implementation of Hypoplasticity.” 35.

Moré, J.J. (1978). “The Levenberg-Marquardt algorithm: Implementation and theory.” *Numerical Analysis*, Springer, Berlin, Heidelberg (Ed: Watson, G. A.), Dundee, Scotland, 105-116.

Muir Wood, D. (1990). Soil Behaviour and Critical State Soil Mechanics. Cambridge University Press.

Ng., C. W. W., Fung, W. T, Cheuk, C. Y., and Zhang. L. (2004). “Influence of Stress Ratio and Stress Path on Behavior of Loose Decomposed Granite.” *Journal of Geotechnical and Geoenvironmental Engineering*, 130(1), 36–44.

Ng, C. W. W., D. B. Akinniyi, and C. F. Chiu. (2019). “Comparisons of weathered lateritic, granitic and volcanic soils: Compressibility and shear strength.” *Eng. Geol.*, 249, 235-240.

Niemunis, A., and Herle, I. (1997). “Hypoplastic model for cohesionless soils with elastic strain range.” *Mechanics of Cohesive-Frictional Materials*, 4(2), 279–299.

Niemunis, A. (2002). "Extended Hypoplastic models for soils." Habilitation Thesis, Ruhr-University, Bochum.

Niemunis, A. (2003). “Anisotropic effects in hypoplasticity.” *3rd International Symposium on Deformation Characteristics of Geomaterials*, (Ed: Di Benedetto et al.), Lyon, France, 1211-1217.

Poeter, E.P. and Hill, M.C. (1998). Documentation of UCODE, a computer code for universal inverse modeling, U.S. Geological Survey Water-Resources, Denver, Colorado.

Rahardjo, H., B. H. Ong, and E. C. Leong. (2004). “Shear strength of a compacted residual soil from consolidated drained and constant water content triaxial tests.” *Can. Geotech J.*, 41 (3), 421–436.

Rocchi, I., and Coop., M. R. (2015). “The effects of weathering on the physical and mechanical properties of a granitic saprolite.” *Géotechnique*, 65(6), 482–493.

Roscoe, K.H., Burland, J.B. (1968). “On the generalized stress-strain behavior of “wet” clay”. In: Heyman & Leckie, Engineering Plasticity, Cambridge University Press. 535–609.

Roscoe, K.H., Schofield, A.N., Thurairajah, A. (1963). “Yielding of clays in states wetter than critical”. *Géotechnique.* 13(3), 211–240.

Sarabia, F. (2012). "Hypoplastic Constitutive Law Adapted to Simulate Excavations in Chicago Glacial Clays." Doctor of Philosophy Dissertation, Northwestern University, Evanston, Illinois.

Schanz, T., Vermeer, A., and Bonnier, P. (1999). “The hardening soil model: formulation and verification.” *Beyond 2000 in Computational Geotechnics: 10 Years of Plaxis International, Proceedings of the International Symposium Beyond 2000 in Computational Geotechnics*, Balkema, Rotterdam, Netherlands, 281-296.

Schofield, A.N., and Wroth, C.P. (1968). *Critical state soil mechanics*, McGraw-Hill, London.

Schweiger, H.F. (2008), The Role of Advanced Constitutive Models in Geotechnical Engineering. *Geomechanics and Tunnelling*, 1(5), 336-344.

Shu, R., Kong, L., Liu, B., Wang, J. (2021). “Stress–Strain Strength Characteristics of Undisturbed Granite Residual Soil Considering Different Patterns of Variation of Mean Effective Stress”. *Appl. Sci*., 11, 1874.

Smith, P. R., Jardine, R. J., and Hight, D. W. (1992). “The yielding of bothkennar clay.” *Géotechnique*, 42(2), 257–274.

Teachavorasinskun, S., and Amornwithayalax, T. (2002). “Elastic shear modulus of Bangkok clay during undrained triaxial compression.” *Géotechnique*, 52(7), 537–540.

The MathWorks, I. (2020). Symbolic Math Toolbox, Natick, Massachusetts, United State. Available at: https://www.mathworks.com/help/symbolic/.

Timoshenko, S., and Goodier J. N. (1951). *Theory of elasticity, 2nd Ed*., McGraw-Hill, New York.

Ti, K. S., Huat, B. B., Noorzaei, J., Jaafar, M. S., & Sew, G. S. (2009). “A review of basic soil constitutive models for geotechnical application”. *Electronic Journal of Geotechnical Engineering*, 14, 1-18.

Torres, C., and Colmenares, J. E. (2018). "Influence of ConfiningStress on the Small Strain Stiffness of a Residual Soilunder K_0 Conditions," *PanAm Unsaturated Soils 2017.* Dallas, Texas.

United Nations Department of Economic and Social Affairs. (2019). *Revision of world population prospects*. New York: UN DESA

Vaughan, P. R., and Kwan, C. W. (1984). "Weathering, structure and in situ stress in residual soils." *Géotechnique*, 34(1), 43–59.

Viana da Fonseca, A., Fernandes, M. M., and Cardoso, S. A. (1997). "Interpretation of a footing load test on a saprolitic soil from granite." *Géotechnique*, 47(3), 633–651.

Viggiani, G., and Atkinson, J. H. (1995). "Stiffness of fine–grained soil at very small strains." *Géotechnique*, 45(2), 245–265.

von Wolffersdorff., P. A. (1996). "A hypoplastic relation for granular materials with a predefined limit state surface." *Mechanics of Cohesive-Frictional Materials*, 1(3), 251–271.

Wang, Y., and Ng. (2005). "Effects of stress paths on the small strain stiffness of completely decomposed granite." *Canadian Geotechnical Journal*, 42 (4), 1200–1211.

Wesley, L.D. (1990). "Influence of structure and composition on residual soils." *Journal of Geotechnical Engineering*, 116(4), 589–603.

Wesley, L. D. (2009). *Fundamentals of soil mechanics for sedimentary and residual soils.*, John Wiley & Sons, Inc., New Jersey.

Wesley, L. D. (2010). *Geotechnical engineering in residual soils.*, John Wiley & Sons, Inc., New Jersey.

Wichtmann, T. (2016). “Soil Behaviour under Cyclic Loading – Experimental Observations”, Constitutive Description and Applications. Veröffentlichungen des Instituts für Bodenmechanik und Felsmechanik am KIT. Habilitation. Helft 181.

Appendix A: Parameter optimization code.

“Opytimization” V.0.0.1. By Alan Jaret Aparicio Ortube (2022)

INPUTS:

```
# Activate scripting server:
## Make sure Plaxis 2D Input is open and the server is active
## (localhostports and password must coincide with the data below)
localhostport_input = 10000
localhostport_output = 10001
password_plaxis = 'PASSWORD'
from plxscripting.easy import *
s_i, g_i = new_server('localhost', localhostport_input, password = passwo
rd_plaxis)
s_o, g_o = new_server('localhost', localhostport_output, password = passw
ord_plaxis)

# Python packages:
import numpy as np
import scipy.optimize as optimize
from scipy.interpolate import interp1d
import matplotlib.pyplot as plt
import pandas as pd
import time

# Time:
time_start = time.ctime()

# Parameters to be optimized:
## Reference values:
## phi (from 22.7 to 35.6)
## lambda* (from 0.0033 to 0.296)
## kappa* (from 0.003 to 0.020)
## N (from 0.507 to 2.760)
## nu (from 0.01 to 0.37)
## R (from 5e-5 to 1e-4)
## beta_r (from 0.08 to 0.20)
## chi (from 0.8 to 0.9)
## Ag (from 270 to 5300)
## ng (from 0.5 to 1.0)
## m_rat (0.5)
```

```
## alpha_g (from 1.10 to 2.00)
## alpha_e (1.13)
## alpha_nu (1.10)

chi = 0.1
print("chi=" + str(chi))
#nu_scaled = (nu - 0.01) / (0.37 - 0.01) # linear scaling function
chi_scaled = chi
print("chi scaled=" + str(chi_scaled))
x0 = np.array([chi_scaled]) # initial value

# TXC_Laboratory data (Deviatoric Stress vs Axial Strain):
txc_lab_data = pd.read_excel(r'Route')
print(txc_lab_data)
lab_axial_strain_txc = txc_lab_data.iloc[ : , 0]
lab_deviator_stress_txc = txc_lab_data.iloc[ : , 1]


# TXC_Laboratory data (Secant shear modulus vs shear Strain):
txc_lab_modulus_data = pd.read_excel(r'Route')
print(txc_lab_modulus_data)
lab_shear_strain_txc = txc_lab_modulus_data.iloc[ : , 0]
lab_modulus_txc = txc_lab_modulus_data.iloc[ : , 1]


## TXC Laboratory data plot (Deviatoric Stress vs Axial Strain):
plt.scatter(lab_axial_strain_txc, lab_deviator_stress_txc,
            label = 'Observed', marker = 'o',
            s = 10, color = 'black')
plt.title('TXC - Laboratory data')
plt.xlabel('Axial strain [%]')
plt.ylabel('Deviatoric stress [kPa]')
plt.legend(loc = 'lower right')
plt.show()


## TXC Laboratory data plot (Secant shear modulus vs shear Strain)::
plt.scatter(lab_shear_strain_txc, lab_modulus_txc,
            label = 'Observed', marker = 'o',
            s = 10, color = 'black')
plt.title('TXC - Laboratory data')
plt.xlabel('Shear strain [%]')
plt.ylabel('Secant Shear Modulus [MPa]')
plt.legend(loc = 'lower right')
plt.xscale('log')
plt.show()

# Optimization parameters:
## The phase where shearing stage begins:
phase_start_txc = 4 # phase after RTXE Shearing
phase_end_txc = 13 # phase after TXC Shearing

## Optimization function:
```

```
ftol = 1e-8 # default=1e-8
xtol = 1e-8 # default=1e-8
gtol = 1e-8 # default=1e-8
diff_step = 1e-1
max_nfev = 60 # tip: control script perfomance with this parameter
#bounds = (0.19, 0.22) #Optimization limits
```

Traced values during iterations

```
counter = 0
counter_l = []
iteration = 0
iteration_l = []
opt_parameters = []
residual = []
```

Optimization function

```
def opt_fun(x):
    #nu_normal = x[0] * (0.37 - 0.01) + 0.01
    chi_normal = x[0]
    x_normal = np.array([chi_normal])

    global counter, iteration
    counter = counter + 1
    if counter == iteration * len(x0) + iteration + 1:
        iteration = iteration + 1

    iteration_l.append(iteration - 1)
    counter_l.append(counter)
    opt_parameters.append(x_normal)

    # Plaxis:
    ## Go to Staged Constructions:
    g_i.gotostages()

    ## Turn phases off from staged constructions:
    for phase in g_i.Phases[:]:
        phase.ShouldCalculate = True

    ## Update constitutive soil parameter:
    g_i.CaldasSite1.setproperties("User15", x_normal[0])

    ## Calculate all phases:
    g_i.calculate()

    ## Open Plaxis 2D Output:
    output_port = g_i.view(g_i.Phases[-1])
    s_o, g_o = new_server('localhost', output_port, password = password_p
laxis)
```

```
    ## EXTRACT SIMULATED DATA - RTXE:
    ###In-Situ state RTXE
        TXC_EAS = []
        TXC_ERS = []
        TXC_AS = [0]
        TXC_RS = [0]

        TXC_EAS.append(g_o.getcurveresults(g_o.Stresspoints[-1],
                               g_o.Phases[phase_start_txc - 2],
                               g_o.ResultTypes.Soil.SigyyE))

        TXC_ERS.append(g_o.getcurveresults(g_o.Stresspoints[-1],
                               g_o.Phases[phase_start_txc - 2],
                               g_o.ResultTypes.Soil.SigxxE))

        ###Effective stresses and strains - TXC
        for i in range(phase_start_txc - 1, phase_end_txc):
         values_TXC_EAS = g_o.getcurveresultspath(g_o.Stresspoints[-1],
                         g_o.Phases[i],
                         g_o.Phases[i],
                         g_o.ResultTypes.Soil.SigyyE)
        values_TXC_EAS = values_TXC_EAS.echo()
        values_TXC_EAS = values_TXC_EAS[1:len(values_TXC_EAS) - 1]
        values_TXC_EAS = [float(idx) for idx in values_TXC_EAS.split(', ')

        TXC_EAS = TXC_EAS + values_TXC_EAS

        values_TXC_ERS = g_o.getcurveresultspath(g_o.Stresspoints[-1],
                       g_o.Phases[i],
                       g_o.Phases[i],
                       g_o.ResultTypes.Soil.SigxxE)
        values_TXC_ERS = values_TXC_ERS.echo()
        values_TXC_ERS = values_TXC_ERS[1:len(values_TXC_ERS) - 1]
        values_TXC_ERS = [float(idx) for idx in values_TXC_ERS.split(', ')

        TXC_ERS = TXC_ERS + values_TXC_ERS

        values_TXC_AS = g_o.getcurveresultspath(g_o.Stresspoints[-1],
                       g_o.Phases[i],
                       g_o.Phases[i],
                       g_o.ResultTypes.Soil.Epsyy)
        values_TXC_AS = values_TXC_AS.echo()
        values_TXC_AS = values_TXC_AS[1:len(values_TXC_AS) - 1]
        values_TXC_AS = [float(idx) for idx in values_TXC_AS.split(', ')]
        TXC_AS = TXC_AS + values_TXC_AS

        values_TXC_RS = g_o.getcurveresultspath(g_o.Stresspoints[-1],
                       g_o.Phases[i],
                       g_o.Phases[i],
                       g_o.ResultTypes.Soil.Epsxx)
        values_TXC_RS = values_TXC_RS.echo()
        values_TXC_RS = values_TXC_RS[1:len(values_TXC_RS) - 1]
        values_TXC_RS = [float(idx) for idx in values_TXC_RS.split(', ')]
```

```
        TXC_RS = TXC_RS + values_TXC_RS

        ### Dataframe:
        data_txc = {'TXC_EAS':TXC_EAS,
                    'TXC_ERS':TXC_ERS,
                    'TXC_AS':TXC_AS,
                    'TXC_RS':TXC_RS}
    Sim_TXC = pd.DataFrame(data_txc)
    Sim_TXC['TXC_EAS'] = Sim_TXC['TXC_EAS'] * (-1) # effective vertical s
tress sign is transformed to the geotechnical convention
    Sim_TXC['TXC_ERS'] = Sim_TXC['TXC_ERS'] * (-1) # effective radial str
ess sign is transformed to the geotechnical convention
    Sim_TXC['TXC_q'] = Sim_TXC['TXC_EAS'] - Sim_TXC['TXC_ERS']
    Sim_TXC['TXC_AS'] = Sim_TXC['TXC_AS'] * 100 * (-1) # axial strain sig
n is transformed to the geotechnical convention
    Sim_TXC['TXC_RS'] = Sim_TXC['TXC_RS'] * 100 * (-1) # radial strain si
gn is transformed to the geotechnical convention
    Sim_TXC['TXC_SS'] = (Sim_TXC['TXC_AS'] - Sim_TXC['TXC_RS']) * 2 / 3
    Sim_TXC['TXC_delta_q'] = Sim_TXC['TXC_q'] - Sim_TXC['TXC_q'][0]
    Sim_TXC['TXC_SM'] = Sim_TXC['TXC_delta_q'] / 3 / (Sim_TXC['TXC_SS'] /
100) / 1000

    ## Close Plaxis 2D Output:
    g_o.close()


    ### Interpolation_TXC:
    f_interp_txc = interp1d(Sim_TXC.iloc[1: , 5], Sim_TXC.iloc[1: , 7],
                            kind = 'cubic', fill_value = 'extrapolate')
    interp_SM_txc = f_interp_txc(lab_shear_strain_txc)

    # Objective function:
    error_txc = lab_modulus_txc - interp_SM_txc
    residual.append(sum(error_txc ** 2) * 0.5)
    return error_txc


Results

# Optimization:
opt_result = optimize.least_squares(fun = opt_fun,
                                    x0 = x0,
                                    method = 'lm',
                                    ftol = ftol,
                                    xtol = xtol,
                                    gtol = gtol,
                                    diff_step = diff_step,
                                    max_nfev = max_nfev)
                                    #bounds = bounds)
print("Optimization message:")
print(opt_result.message)
```

```
# Optimized parameter:
#nu_normal = opt_result.x[0] * (0.37 - 0.01) + 0.01
chi_normal = opt_result.x[0]
x_normal = np.array([chi_normal])
print("Optmized parameter:")
print("chi=" + str(x_normal))


# Optimized response:
## Go to Staged Constructions:
g_i.gotostages()

## Turn phases off from staged constructions:
for phase in g_i.Phases[:]:
    phase.ShouldCalculate = True

## Update constitutive soil parameter:
g_i.CaldasSite1.setproperties("User15", x_normal[0])

## Calculate all phases:
g_i.calculate()

## Open Plaxis 2D Output:
output_port = g_i.view(g_i.Phases[-1])
s_o, g_o = new_server('localhost', output_port, password = password_plaxi
s)


## EXTRACT SIMULATED DATA - RTXE:
###In-Situ state RTXE
TXC_EAS = []
TXC_ERS = []
TXC_AS = [0]
TXC_RS = [0]

TXC_EAS.append(g_o.getcurveresults(g_o.Stresspoints[-1],
                                   g_o.Phases[phase_start_txc - 2],
                                   g_o.ResultTypes.Soil.SigyyE))

TXC_ERS.append(g_o.getcurveresults(g_o.Stresspoints[-1],
                                   g_o.Phases[phase_start_txc - 2],
                                   g_o.ResultTypes.Soil.SigxxE))

###Effective stresses and strains - TXC
for i in range(phase_start_txc - 1, phase_end_txc):
    values_TXC_EAS = g_o.getcurveresultspath(g_o.Stresspoints[-1],
                     g_o.Phases[i],
                     g_o.Phases[i],
                     g_o.ResultTypes.Soil.SigyyE)
    values_TXC_EAS = values_TXC_EAS.echo()
    values_TXC_EAS = values_TXC_EAS[1:len(values_TXC_EAS) - 1]
    values_TXC_EAS = [float(idx) for idx in values_TXC_EAS.split(', ')]
```

```
    TXC_EAS = TXC_EAS + values_TXC_EAS

    values_TXC_ERS = g_o.getcurveresultspath(g_o.Stresspoints[-1],
              g_o.Phases[i],
              g_o.Phases[i],
              g_o.ResultTypes.Soil.SigxxE)
     values_TXC_ERS = values_TXC_ERS.echo()
     values_TXC_ERS = values_TXC_ERS[1:len(values_TXC_ERS) - 1]
     values_TXC_ERS = [float(idx) for idx in values_TXC_ERS.split(', ')]
     TXC_ERS = TXC_ERS + values_TXC_ERS

     values_TXC_AS = g_o.getcurveresultspath(g_o.Stresspoints[-1],
                         g_o.Phases[i],
                         g_o.Phases[i],
                         g_o.ResultTypes.Soil.Epsyy)
     values_TXC_AS = values_TXC_AS.echo()
     values_TXC_AS = values_TXC_AS[1:len(values_TXC_AS) - 1]
     values_TXC_AS = [float(idx) for idx in values_TXC_AS.split(', ')]
     TXC_AS = TXC_AS + values_TXC_AS

     values_TXC_RS = g_o.getcurveresultspath(g_o.Stresspoints[-1],
                     g_o.Phases[i],
                     g_o.Phases[i],
                     g_o.ResultTypes.Soil.Epsxx)
     values_TXC_RS = values_TXC_RS.echo()
     values_TXC_RS = values_TXC_RS[1:len(values_TXC_RS) - 1]
     values_TXC_RS = [float(idx) for idx in values_TXC_RS.split(', ')]
     TXC_RS = TXC_RS + values_TXC_RS

### Dataframe:
data_txc = {'TXC_EAS':TXC_EAS,
            'TXC_ERS':TXC_ERS,
            'TXC_AS':TXC_AS,
            'TXC_RS':TXC_RS}
Sim_TXC = pd.DataFrame(data_txc)
Sim_TXC['TXC_EAS'] = Sim_TXC['TXC_EAS'] * (-1) # effective vertical stres
s sign is transformed to the geotechnical convention
Sim_TXC['TXC_ERS'] = Sim_TXC['TXC_ERS'] * (-1) # effective radial stress
sign is transformed to the geotechnical convention
Sim_TXC['TXC_q'] = Sim_TXC['TXC_EAS'] - Sim_TXC['TXC_ERS']
Sim_TXC['TXC_AS'] = Sim_TXC['TXC_AS'] * 100 * (-1) # axial strain sign is
transformed to the geotechnical convention
Sim_TXC['TXC_RS'] = Sim_TXC['TXC_RS'] * 100 * (-1) # radial strain sign i
s transformed to the geotechnical convention
Sim_TXC['TXC_SS'] = (Sim_TXC['TXC_AS'] - Sim_TXC['TXC_RS']) * 2 / 3
Sim_TXC['TXC_delta_q'] = Sim_TXC['TXC_q'] - Sim_TXC['TXC_q'][0]
Sim_TXC['TXC_SM'] = Sim_TXC['TXC_delta_q'] / 3 / (Sim_TXC['TXC_SS'] / 100
) / 1000

## Close Plaxis 2D Output:
g_o.close()


### Interpolation_TXC:
```

```
f_interp_txc = interp1d(Sim_TXC.iloc[1: , 5], Sim_TXC.iloc[1: , 7],
                        kind = 'cubic', fill_value = 'extrapolate')
interp_SM_txc = f_interp_txc(lab_shear_strain_txc)

      ## TXC - Secant Shear Modulus - Shear strain:
plt.scatter(lab_shear_strain_txc, lab_modulus_txc,
            label = 'Observed', marker = 'o',
            s = 10, color = 'black')
plt.plot(lab_shear_strain_txc, interp_SM_txc,
         label = 'Interpoled', linestyle = 'dashed', color = 'red')
plt.plot(Sim_TXC.iloc[1: , 5], Sim_TXC.iloc[1: , 7],
         label = 'Simulated', linestyle = 'dashdot',
         linewidth = 2, color = 'steelblue')
plt.title('TXC')
plt.xlabel('Shear strain [%]')
plt.ylabel('Secant Shear Modulus [MPa]')
plt.legend(loc = 'upper right')
plt.xscale('log')
plt.xlim(0.003, 2)
plt.ylim(0, 40)
plt.show()

## TXC - Deviatoric Stress - Axial strain:
plt.scatter(lab_axial_strain_txc, lab_deviator_stress_txc,
            label = 'Observed', marker = 'o',
            s = 10, color = 'black')
plt.plot(Sim_TXC.iloc[0: , 2], Sim_TXC.iloc[: , 4],
         label = 'Simulated', linestyle = 'dashdot',
         linewidth = 2, color = 'steelblue')
plt.title('TXC')
plt.xlabel('Axial strain [%]')
plt.ylabel('Deviatoric Stress [kPa]')
plt.legend(loc = 'upper right')
plt.xlim(-0.1, 2)
plt.show()


## Residual - Constitutive soil parameter (convergence):
error_last = lab_modulus_txc - interp_SM_txc
residual.append(sum(error_last ** 2) * 0.5)
print("Residual:")
print(residual)

opt_parameters.append(x_normal)
print("Optimized parameters:")
print(opt_parameters)

counter_l.append(counter + 1)
print("Counter:")
print(counter)
print(counter_l)

iteration_l.append(iteration)
```

```
print("Iteration:")
print(iteration)
print(iteration_l)

### Plots:
#### chi:
opt_parameters_values_chi = []
for i in range(len(opt_parameters)):
    opt_parameters_values_chi.append(opt_parameters[i])

plt.plot(opt_parameters_values_chi, residual,
         label = 'chi', marker = 'o', color = 'black')
plt.xlabel('chi')
plt.ylabel('Residual')
plt.legend(loc = 'best')
plt.show()

plt.plot(counter_l, opt_parameters_values_chi,
         label = 'chi', marker = 'o', color = 'black')
plt.xlabel('Counter')
plt.ylabel('chi')
plt.legend(loc = 'best')
plt.show()


print("Optimization details:")
print(opt_result)

###Export results
# Simulated soil response RTXE :
#sim_data_3_rtxe.to_excel(r'sim_data_RTXE.xlsx', index = False, header =
True)

# Interpoled soil response - RTXE:
#sim_data_interp_rtxe.to_excel(r'Interp_data_RTXE.xlsx', index = False, h
eader = True)

# Simulated soil response TXC :
#sim_data_txc.to_excel(r'sim_data_TXC.xlsx', index = False, header = True
)

# Interpoled soil response - TXC:
#sim_data_interp_txc.to_excel(r'Interp_data_TXC.xlsx', index = False, hea
der = True)

# Optimized parameters:
#data_parameters = {'Counter':counter_l,
                   #'Iteration':iteration_l,
                   #'Residual':residual,
                   #'nu':opt_parameters}
#optimized_parameters = pd.DataFrame(data_parameters)
#optimized_parameters.to_excel(r'Optimized_Parameters_1p.xlsx', index = F
alse, header = True)
```

```
time_end = time.ctime()
text_0 = f'Initial time:\n{time_start}\n\nFinal time:\n{time_end}'
print("Time:")
print(text_0)
```